ABSTRACT

Title of dissertation: ANALYSIS AND CONTROL OF MICROSTRUCTURE IN BINARY ALLOYS

Kyuyong Lee, Doctor of Philosophy, 2004

Dissertation directed by: Professor Wofgang Losert
Department of Physics

When metallic alloys solidify, various microstructures form inside the alloys. Most solidified alloys have a polycrystalline structure, which is an assembly of crystalline grains with boundaries between any two grains. Each grain is a single crystal with a unique crystalline orientation. Many physical properties of polycrystalline alloys are determined by the arrangement of these grains and grain boundaries. During solidification of a single crystal, microstructures with even smaller microscopic lengthscales form, such as dendritic and eutectic structures. The physical properties of single crystal alloys are largely influenced by the lengthscales of these structures. Therefore, the understanding and control of microstructure formation in solidification is important in order to achieve desired properties.

Microstructures form while the system is not in equilibrium. What microstructures form is not based on minimization of free energy of the system, but depends on the dynamics of the solidification process, which is the focus of our study. We used an alloy model system, succinonitrile-coumarin152 (SCN-C152), to experimentally investigate dynamic selection and control of grain boundary structures and

dendritic structures in binary alloys. We found that in a temperature gradient the grain boundaries drift toward the high temperature region in addition to the migration due to grain coarsening. We show how we can control grain boundary orientations by generating local temperature gradient through UV or laser heatings. We show that perturbations also permit accurate control of the microstructure within a single crystal during the directional solidification process. Dendritic patterns can be controlled either by guiding the initial formation of the pattern or by triggering subcritical transitions between stable microstructures. We also investigated the role of surface tension anisotropy on the stability of cellular/dendritic arrays using three crystals of different growth orientations with respect to the surface tension anisotropy. We found that the surface tension anisotropy affects the spacing between dendrites and stability via the surface tension perpendicular to the growth direction.

ANALYSIS AND CONTROL OF MICROSTRUCTURE IN BINARY ALLOYS

by

Kyuyong Lee

Dissertation submitted to the Faculty of the Graduate School of the
University of Maryland, College Park in partial fulfillment
of the requirements for the degree of
Doctor of Philosophy
2004

Advisory Committee:

Professor Wolfgang Losert, Chair/Advisor
Professor Robert M. Briber
Dr. James A. Warren
Professor Christopher J. Lobb
Professor Daniel P. Lathrop

DEDICATION

This dissertation is dedicated to my grandfather,

Jongsung Lee (1905-1998).

ACKNOWLEDGMENTS

First, I would like to thank my adviser, Professor Wolfgang Losert, for his support and guidance throughout my research and writing the dissertation. Because of him I could develop scientific insights in experimental physics.

Next, I would like to thank Don Martin for his technical help and valuable suggestions on experimental apparatus. Edward Condon kindly helped me whenever I had problems with computers. I would also like to thank Silvere Akamatsu, James A. Warren, and Sascha Hilgenfeldt for valuable discussions on my research projects. I thank Dorothea Brosius for providing the LaTex templates for writing this dissertation.

My gratitude also goes to Maria Aronova, Dominic Britti, Peter Bradford, Matt Ferguson, Julio Friedmann, Jennifer Galanis, Sejin Han, Nicole Harrison, David Jones, Jongwon Kim, Minyoung Kim, Youngchan Kim, Younggu Kim, Matt Kelley, Gene Kwon, Mike Newey, Ricardo Pizarro, Andrew Pomerance, Andrew Porter, Cory Poole, Jay Pyle, Mumtaz Qazilbash, Erin Rericha, Ron Skupsky, Ryan Smith, Justin Stambough, Nicolas Taberlet, Masahiro Toiya, and Cynthia Wu for sharing their inspiring ideas and having pleasant conversations with me.

I cannot thank enough my parents for their endless support and careful consideration.

Last and most, I thank my wife, Eunah Song, for her continuous support and

patience. Without her love, this moment would not even exist.

TABLE OF CONTENTS

List of Figures vii

1 Introduction 1

2 Background 14

3 Instruments for Microstructure Imaging and Control 24

3.1 The Alloy Model System 24

3.2 Directional Solidification Setup 25

3.3 Laser Scanning Confocal Microscope 27

3.4 Two-photon Laser Scanning Microscope 32

3.5 Holographic Optical Tweezer Array 35

4 Controlled Dynamics of Grain Boundaries in Binary Alloys 38

4.1 Overview 38

4.2 Experimental Detail 38

4.3 Results and Discussion 39

4.4 Conclusion 62

5 Local Control of the Dendritic Microstructure Through Perturbation 67

5.1 Overview 67

5.2 Experimental Detail 68

5.3 Results and Discussion 71

5.4 Conclusion 80

6 Studies on Cellular/Dendritic Arrays with Different Crystal Orientations 83

6.1 Overview 83

6.2 Experimental Detail 84

6.3 Results and Discussion 85

6.4 Conclusion 101

A Preliminary Studies on Eutectic Microstructure 103

A.1 Overview 103

A.2 Microstructure Control Through Adaptive Holograms 109

A.3 Analyzing Interface Anisotropy Through Confocal Microscopy 116

A.4 Conclusion 118

B Sample Preparation 120

B.1 Capillary Cleaning 120

B.2 Distillation of SCN 120

B.3 Filling the Sample Capillaries 125

C Image Analysis 127

C.1 Programs for Dendrite Tip Extraction 127

C.2 Programs for Grain Boundary Extraction 132

C.3 Programs for Obtaining Speed of Grain Boundaries 133

Bibliography 137

LIST OF FIGURES

1.1 Iron dendrites obtained in a steel ingot. (from [1]) 3

1.2 Al-Cu Al_2 lamellar eutectic normal to the growth direction. (from [2]) 4

1.3 Polycrystalline grains in zinc-5.2% aluminum alloy. (from [1]) 5

1.4 When metallic alloys solidify, many nuclei form initially. The nuclei then grow into spherical crystals which become unstable and dendritic in form. These dendrites grow in the melt and impinge on one another. These points of impingement become grain boundaries. Each grain originates from a nucleus and has different crystal orientation. (from [3]) 6

1.5 A intergranular fracture caused by brittle grain boundaries. (from [7]) 7

1.6 Examples of intergranular creep fracture. (from [8]) 7

1.7 A directionally solidified single crystal (tin-1% lead alloy). The black lines indicate the segregation of composition resulted from dendritic growth. (from [1]) 9

1.8 An illustrated branched structure of a dendrite growing upward. A primary trunk, secondary and tertiary branches are shown. λ_1 and λ_2 denote the primary and secondary arm spacings respectively. (from [3]) 10

2.1 A typical phase diagram of dilute binary alloys. C is the concentration of the second alloy component, T is the equilibrium temperature, and k is the segregation coefficient. 16

2.2 Schematic phase diagram of the solid-liquid interface pattern as a function of growth speed V and interdendritic spacing λ. 22

3.1 A schematic of a temperature gradient setup. 26

3.2 (a) A confocal microscope image of growing dendrites. (b) A plot of concentration field along the green line in (a). An exponential fit yields a diffusion length of approximately $78\mu m$ in the liquid ahead of the dendrite tip. 29

3.3 Schematic diagram showing the principle of a laser scanning confocal microscope. 30

3.4 (a) Schematic diagram showing the principle of two-photon absorption process. (b) Two-photon absorption process occurs only at near the focal point thus heating the interior of a sample. (from [76]) . . . 34

3.5 A schematic of a typical holographic optical tweezer array. a) The phase pattern generated by the programmable phase modulator(DOE). b) Melting around individual grains near the solid-liquid interface using multiple laser spots. (from [88]) 36

4.1 Ideal grain growth at a uniform temperature (T=55 °C). The grains with number of sides larger than six grow and smaller than six shrink. 41

4.2 A plot of the average grain area vs. time. The fluctuations are due to measurement errors in extracting grain areas. The average grain area increases linearly in time. The black line is a linear fit. 42

4.3 A plot of the grain area vs. time for ten grains. The grain with number of sides larger than six grows and smaller than six shrinks. The black lines are fits of the linear portions of the curves (during which the grain maintains the same number of sides). 43

4.4 A plot of the rate of grain area change (the slope of the fit in Fig. 4.3) vs. $N-6$, where N is the number of sides. The blue line is a linear fit. 44

4.5 As a rectangular grain shrinks, two pairs of trijunctions merge. The resulting trijunctions move apart. (The picture has low quality because it has been magnified.) 46

4.6 A plot of the distance between a trijunction and the merging point versus time for Fig. 4.5. After two pairs of trijunctions (blue lines) merge, two newly created trijunctions (red lines) immediately move away from the merging point. 47

4.7 As a four-sided grain shrinks into a point, four trijunctions become one quadrijunction. (The picture has low quality because it has been magnified.) 48

4.8 A plot of the distance between a trijunction and the merging point versus time for Fig. 4.7. The quadrijunction formed from merging of four trijunctions stays at the merging point for a while (blue lines) before it dissociates into two trijunctions (red lines). 49

4.9 In a temperature gradient (G=2.5K/cm) the grain boundaries drift toward the high temperature region. As grains approach the hot side, they become larger and elongate in the direction of motion. 51

4.10 Speed of grain boundary motion divided by temperature gradient vs. local temperature for six different data sets. All data sets fall on the same curve fit to $V = DG/\{(1-k)(T_0 - T)\}$. 52

4.11 A schematic showing a grain boundary considered as a liquid channel. The concentration gradient across the wet grain boundary induces diffusion of the solute. 53

4.12 A four-sided grain shrinks while drifting in a temperature gradient. (The picture has low quality because it has been magnified.) 55

4.13 A plot of the distance between a trijunction and the merging point versus time after subtracting the effect of motion in a temperature gradient for Fig. 4.12. After two pairs of trijunctions (blue lines) merge, two newly created trijunctions (red lines) immediately move away from the merging point. 56

4.14 Log-log plots of the trajectories for (a) the case of a uniform temperature and (b) the case of a temperature gradient. 57

4.15 The UV spot heating causes the boundaries to align along the radial line. At each point on a grain boundary, we define ϕ as an angle between the tangential line to the boundary and the radial line from the UV spot. R is the distance between the center of the spot and the point. 59

4.16 With the UV spot heating the mean absolute angle $\langle|\phi|\rangle$ decreases in time, while it stays around $\pi/4$ (indicated by a black line) in the absence of UV spot heating. 60

4.17 A plot of $\langle|\phi|\rangle$ vs. R at four different time intervals shows that the distance over which grain boundaries become radially aligned (lower $\langle|\phi|\rangle$) due to local heating increases with time. 61

4.18 The UV line heating causes the boundaries to align along the UV line. At each point on a grain boundary, we define θ as an angle between the tangential line to the boundary and the heating line. 63

4.19 The histogram of the mean absolute angle $\langle|\theta|\rangle$ shows the development of preferred orientation due to the line heating. The black line indicates a uniform distribution. 64

4.20 Two-photon laser scanning microscope image of 3-D grain structure around a heating spot generated by focusing the laser beam. The front view and the corresponding side view are shown. 65

5.1 Uniform dendritic arrays with controlled interdendritic spacing λ are obtained through spatially periodic UV perturbations (bright spots). UV spots: (a) spacing 235 μm, Gaussian width 70 μm, duration 247 s; (b) spacing 190 μm, Gaussian width 65 μm, duration 434 s. 69

5.2 (a) The standard deviation of interdendritic spacings $\delta\lambda$ decreases to zero more rapidly under perturbations than in a reference experiment without perturbation. (same run as in Fig. 5.1; small and large λ correspond to (a) and (b) respectively) (b) The number of dendrites reaches a steady state at an early stage while $\delta\lambda$ shows continuous adjustment toward uniform λ before and after that. ($G = 7.5$ K/cm, $V = 8.8$ μm/s) 70

5.3 Guiding the crystal growth pattern through perturbations: A stable cellular interface pattern (a) is perturbed through localized perturbation of every other tip (UV spots: spacing 386 μm, Gaussian width 96 μm, duration 40 s). This triggers a transition (b) to another stable microstructure, a dendritic array (c). 73

5.4 Modulation amplitude ξ vs time after perturbations with different strength. The band indicates the critical amplitude with uncertainty. The bottom two lines show weak perturbation, which lead to a decaying ξ. The top three lines show the growth of ξ (which leads to period doubling) after strong perturbations. ($G = 4.4$ K/cm, $V = 5.9$ μm/s) 74

5.5 A period halving transition from a dendritic to a cellular array is triggered through very strong UV perturbation on every tip. UV spots: spacing 386 μm, Gaussian width 96 μm, duration 76 s. 76

5.6 Arrays with λ larger than the stable range can be generated transiently through perturbations (second image from below) but the unstable array returns to smaller λ by growing sidebranches (a) or tip splitting (b). 77

5.7 (a) A magnified image of a transient dendrite in Fig. 5.6a. (b) A dendrite in a stable limit cycle state (simulation by A. Karma). (c) A plot of the tip position x and the tip radius vs. time for the dendrite in (a). 79

5.8 Control of non-periodic structures: The local λ is continuously increased by independently movable laser spots (40 μm in diameter) until the system adjusts λ through instabilities - (a) sidebranch growing and (b) tip splitting. The arrows indicate the controlled motion of laser spots. 81

6.1 $\{hkl\}\langle uvw\rangle$-oriented crystal. 86

6.2 (a) $\{001\}\langle 100\rangle$dendrites have sidebranches growing toward each other and growing directly into the wall with 90 ° angle. (b) $\{011\}\langle 100\rangle$-oriented dendrites have sidebranches growing into the wall with 45 ° angle. (c) $\{\bar{1}01\}\langle 101\rangle$-oriented dendrites have sidebranches growing toward other sidebranches but have no sidebranches growing into the wall. 87

6.3 $\{001\}\langle 100\rangle$-oriented crystal have the strong tip and strong transverse surface tensions. 88

6.4 $\{011\}\langle 100\rangle$-oriented crystal have the strong tip and weak transverse surface tensions. 89

6.5 $\{011\}\langle 100\rangle$-oriented crystal have the weak tip and strong transverse surface tensions. 90

6.6 A plot of $\langle\lambda\rangle$ vs. V for $\{001\}\langle 100\rangle$- and $\{011\}\langle 100\rangle$-oriented arrays at two temperature gradients. $C = 0.51$ wt%. 92

6.7 A plot of $\langle\lambda\rangle$, $\langle\lambda_{max}\rangle$, and $\langle\lambda_{min}\rangle$ vs.f V for $\{001\}\langle 100\rangle$- and $\{011\}\langle 100\rangle$-oriented arrays. $C = 0.51$ wt%, $G = 12.7$ K/cm. 94

6.8 A plot of $\langle\lambda\rangle$ vs. V for $\{001\}\langle 100\rangle$- and $\{011\}\langle 100\rangle$-oriented arrays for two different concentrations. $G = 12.7$ K/cm. 95

6.9 A plot of $\langle R\rangle$ vs. V for the samples of Fig. 6.8. $G = 12.7$ K/cm. . . . 97

6.10 A plot of $\langle\lambda\rangle \cdot\langle R\rangle$ vs. V for the samples of Fig. 6.8. $G = 12.7$ K/cm. 98

6.11 A plot of $\langle\lambda\rangle$ vs. V for arrays of $\{001\}\langle 100\rangle$- and $\{\bar{1}01\}\langle 101\rangle$-oriented dendrites. $C = 0.31$ wt%, $G = 4.4$ K/cm. 99

6.12 (a) A magnified image of a $\{\bar{1}01\}\langle 101\rangle$-oriented dendrite. (b) A plot of the tip position y and the tip radius vs. time for the dendrite in (a).100

A.1 Lamellar eutectic pattern observed in TDS of CBr_4-C_2Cl_6 ($C_0 \approx$ 11.6 mol%; $V = 0.5\ \mu\text{ms}^{-1}$). The growth direction is upward (axis z). The solid-solid interfaces, which trace the trajectories of the three-phase coexistence lines (trijunctions), provide a natural spatiotemporal diagram of the growth front. Here, these interfaces are aligned along the growth axis: the pattern is stationary. Inset: coexistence of a stationary pattern and a drifting pattern (tilt domain). 105

A.2 (a) Large-magnification micrograph of a lamellar pattern. The average temperature of the front T_{av} is close to the eutectic temperature T_E, due to the coexistence of the two solids and the liquid. The departure from equilibrium is measured by the undercooling $\Delta T = T_E - T_{av} > 0$, and is determined by the mean curvature of the interface imposed by the equilibrium of the surface tensions on trijunctions and by the modulated concentration field in the liquid. ΔT is a function of λ and V, and presents a minimum, at given V, for a spacing value λ_m (minimum-undercooling spacing), which varies as $V^{-1/2}$ [102, 103]. (b) Numerical simulation of a stationary pattern; courtesy of M. Plapp [see M. Plapp and A. Karma, Phys. Rev. E **66**, 061608 (2002)]. The gray levels represent the diffusion field in the liquid. 106

A.3 Nonstationary, intermittent-like pattern in a CBr_4-C_2Cl_6 sample of concentration close to the eutectic one, observed after a velocity jump far above the threshold of the so-called period-doubling oscillatory instability ($C_0 \approx 11.6$ mol%; $G = 80$ Kcm^{-1}; $V = 0.5$ μms^{-1}). Horizontal dimension: 830 μm. 110

A.4 Perturbation of a lamellar eutectic front by a single, small-power laser spot. (a) Initial, unperturbed stationary pattern; (b) Perturbation; (c) Recovery of the perturbation after 200 s ($V = 0.5$ μms^{-1}). 112

A.5 Perturbation of a lamellar eutectic front by a single, small-power laser spot moving along the solidification axis toward the front (a) for 5 seconds ($V = 1.3$ μms^{-1}); (b) for 40 seconds ($V = 1.0$ μms^{-1}); note the spontaneous appearance of tilt domains. 114

A.6 Control of lamellar structure through localized laser perturbations. (a) Triggering local tilt instability ($V = 1.3$ μms^{-1}). (b) Stopping local tilt instability ($V = 0.7$ μms^{-1}). 115

A.7 (a) Giant-oscillation pattern in a thin sample of a nearly eutectic CBr_4-C_2Cl_6alloy observed in reflected-light confocal microscopy ($V =$ 1.1 μms^{-1}). (b) A magnified detail of the front (square portion in (a)).117

B.1 Schematic of the capillary cleaning. 121

B.2 Schematic of the distillation of SCN. 123

B.3 Schematic of the sample capillary filling. 124

C.1 (a) An original image. (b) Extracted dendrite shape. (c) Obtaining tip positions. (d) Obtaining tip radius. 129

C.2 (a) An original image. (b) Extracted grain boundaries with noises. (c) Extracted grain boundaries after noises are removed. 131

C.3 Extracting grain boundary speed and slope. The colors represent time. 135

Chapter 1

Introduction

An alloy is a material consisting of two or more metals (e.g. brass is an alloy of copper and zinc) or a metal and a nonmetal (e.g. steel is an alloy of iron and carbon). A binary alloy in the form of a solid solution, which we focus on this study, is a mixture of two components with one component replacing some of the other component in its normal crystal lattice. As most metallic products made with alloys are in a solid state, they solidify from the melt at some stage of manufacturing. During this solidification various microstructures form in alloys. While alloy properties are largely determined by the components used and the composition of the components, microstructure formed during solidification of alloy is also important in improving the properties.

The form of solidification microstructure generally depends on the alloy composition. At a low concentration of the second alloy component (dilute binary alloy), the microstructure is single-phase dendritic (Fig. 1.1 (from [1])). At a concentration near the eutectic point, two-phase eutectic structure forms (Fig. 1.2 (from [2])) . In between the two, dendrites with interdendritic eutectic form. These crystal morphologies are not often visible in alloy microstructures because of their small length scale. Instead, we observe crystalline grains (Fig. 1.3 (from [1])), which are made of dendrites or eutectic. Fig. 1.4 (from [3]) illustrates the various stages of

solidification -from nucleus to grain- for the dendritic growth morphology.

The creation of alloy microstructures causes a local change in the composition and this is the reason why alloy properties are influenced by the microstructures. In ordinary alloys, solute is more soluble in liquid than in solid at a given temperature. Therefore, as an alloy solidifies, solute is rejected from solid and piles up in front of the solidification front. This gives rise to microstructure on lengthscales of submicron and up. In this thesis, we consider two microstructures, grain boundary structures and dendritic (treelike) microstructures within grains. In polycrystalline materials the main segregation of composition happens on grain boundaries.

Most metal products are made with polycrystalline materials (Fig. 1.3 (from [1]) shows a polished cross section through a metal, each region is a single crystal, each has different crystalline orientation and reflects differently). The size, shape, and arrangement of crystalline grains determine the mechanical, electrical and other properties of the material. For example ductility and impact resistance of a material get lower as grain size increases. It is also found that a reduction of the grain size in thin films results in electrical resistivity increase since grain boundaries scatter electrons [4]. The electrical resistivity in a certain direction can be influenced by grain boundary orientation.

The grain boundary orientation is also important in brittle fracture [5] and creep failure mechanism [6]. Brittle fracture is static failure caused by crack propagation. If the segregation on grain boundaries is large, cracks propagate along the grain boundaries causing an intergranular fracture as shown in Fig. 1.5 (from [7]). Therefore, the crack growth direction strongly depends on the grain boundary orien-

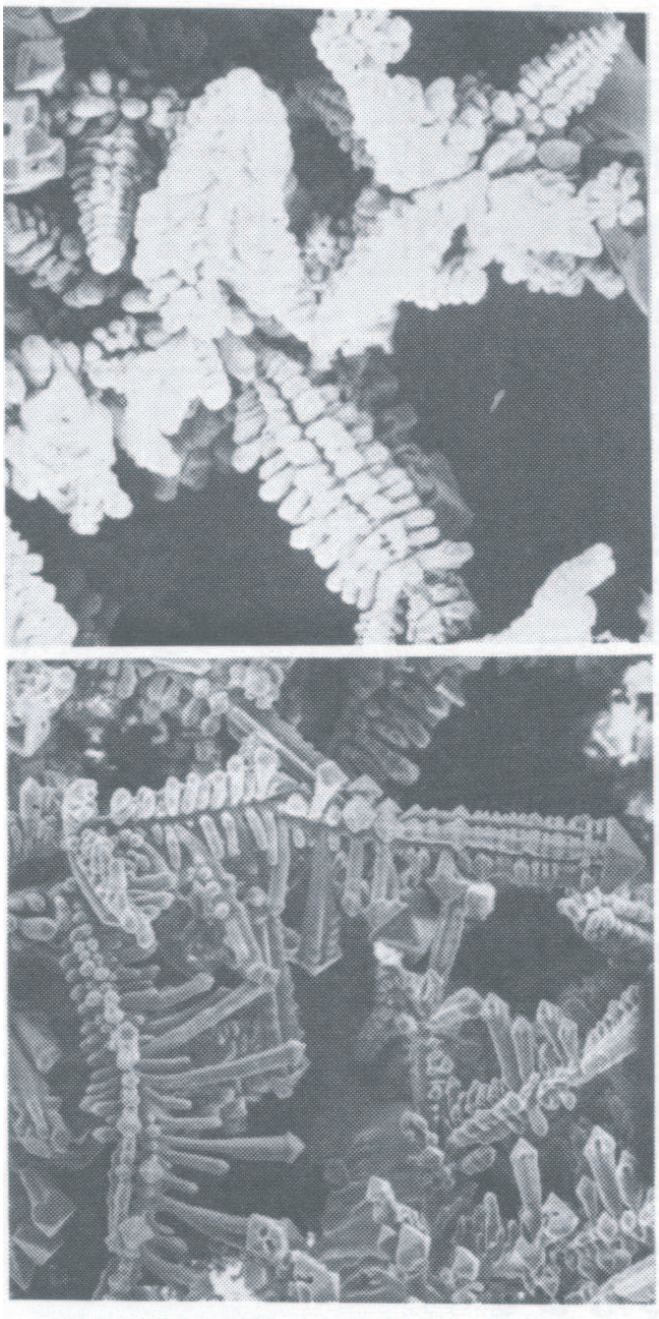

Figure 1.1: Iron dendrites obtained in a steel ingot. (from [1])

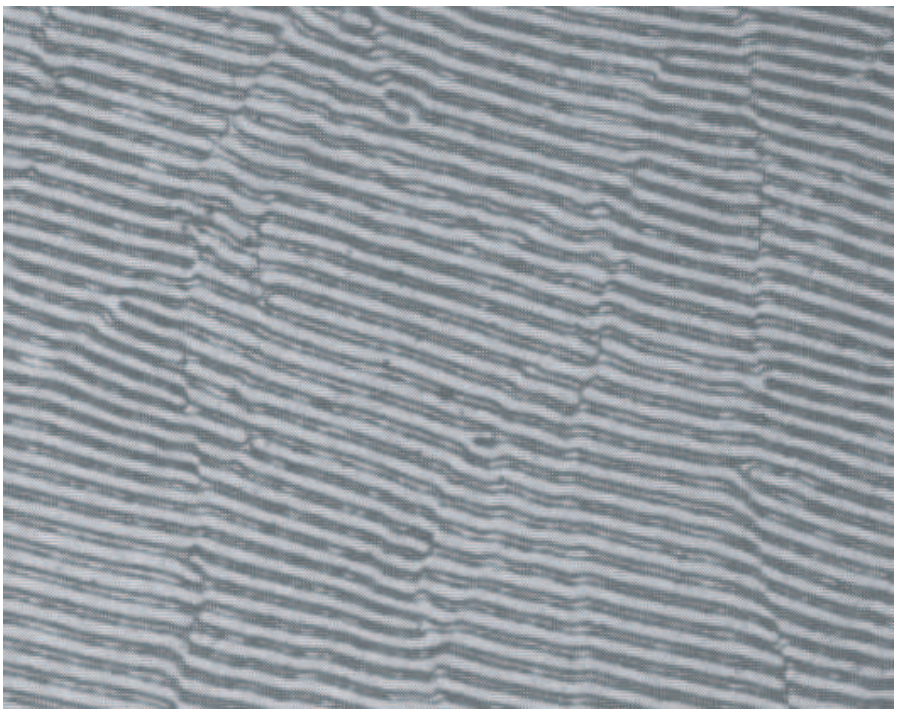

Figure 1.2: Al-Cu Al_2 lamellar eutectic normal to the growth direction. (from [2])

tation. Depending on the grain boundary orientation with respect to applied stress, creep failure (continuous deformation under steady load) can be either intergranular or transgranular. Because voids form more easily along the grain boundaries, creep failure is usually intergranular as shown in Fig. 1.6 (from [8]). If the grain boundary orientation is parallel to the applied stress, creep failure can be greatly reduced due to the lack of intergranular failure. Therefore, it is desirable to control the microstructure of polycrystalline materials in order to improve the material properties. In this thesis, we show how we can control grain boundary orientation through a local temperature gradient.

In some applications, we want to completely remove the grain boundaries. For example, some high performance turbine blades, which operate under a strong tensile

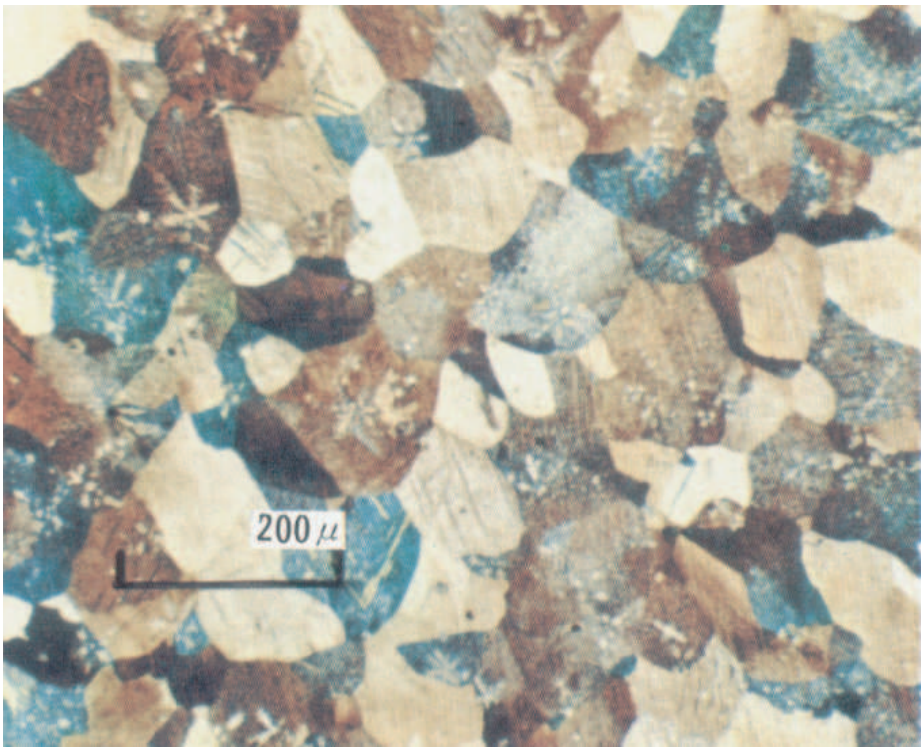

Figure 1.3: Polycrystalline grains in zinc-5.2% aluminum alloy. (from [1])

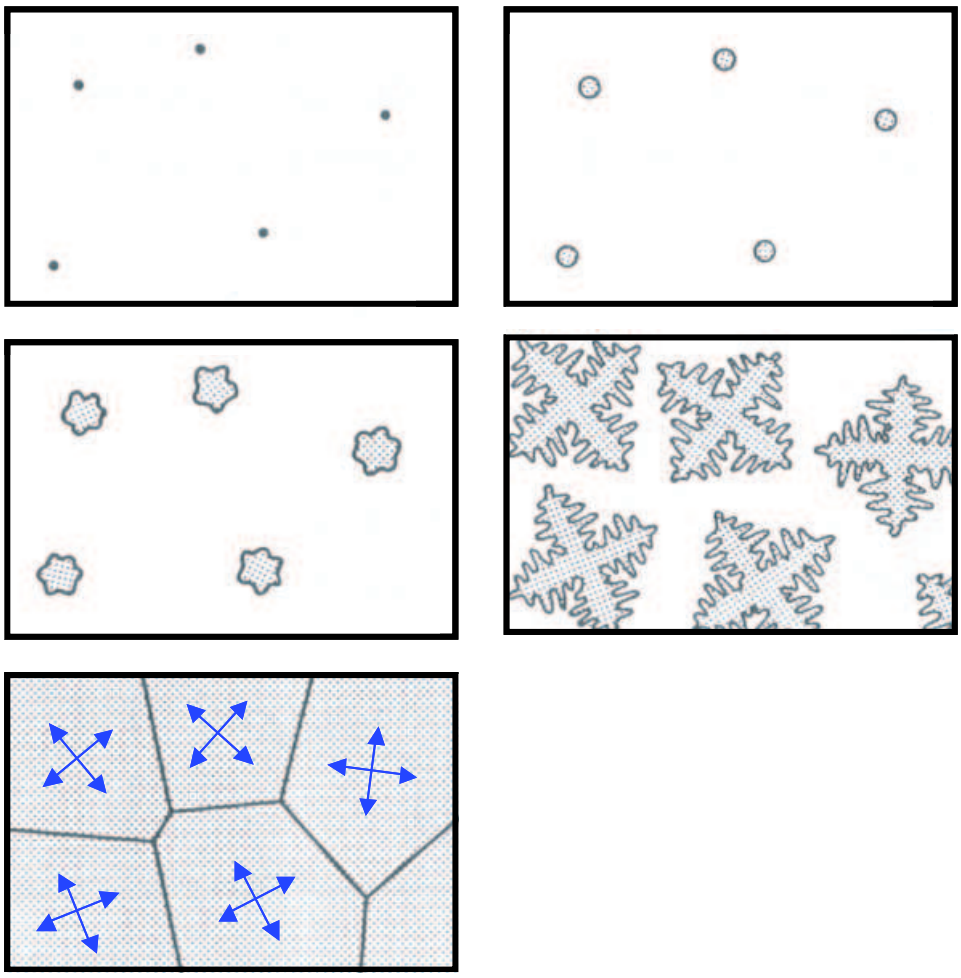

Figure 1.4: When metallic alloys solidify, many nuclei form initially. The nuclei then grow into spherical crystals which become unstable and dendritic in form. These dendrites grow in the melt and impinge on one another. These points of impingement become grain boundaries. Each grain originates from a nucleus and has different crystal orientation. (from [3])

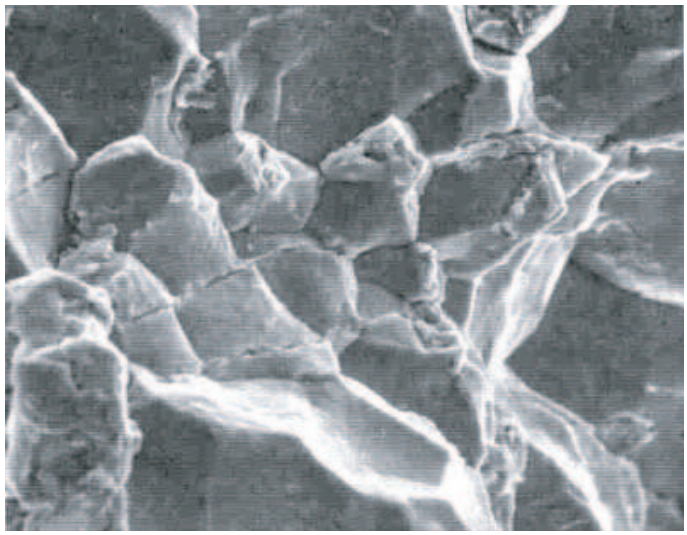

Figure 1.5: A intergranular fracture caused by brittle grain boundaries. (from [7])

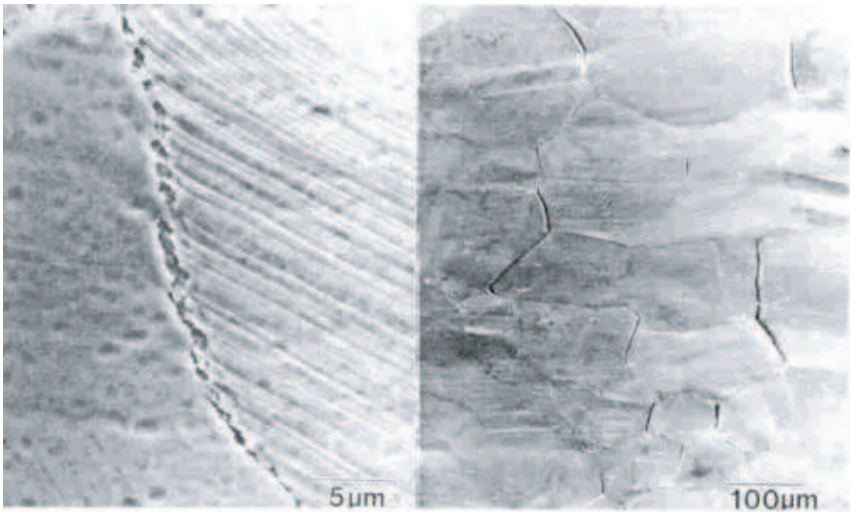

Figure 1.6: Examples of intergranular creep fracture. (from [8])

stress, are made with a directionally solidified single crystal [9] to avoid intergranular failure (Fig. 1.7 (from [1])) and to avoid gradual lengthening of the turbine blade due to intergranular creep. A single crystal is usually obtained by solidifying an alloy through a corkscrew-shaped channel called a grain selector. Only one grain with a particular crystalline orientation emerges from the selector. This grain is then grown further in a directional solidification setup, where the alloy is pulled through a temperature gradient at a constant speed. This process ensures that a whole cast is made of a single crystal with controlled orientation. In a single crystal, the distribution of the second alloy component is also inhomogeneous and leads to intragrain microstructures.

One of the most frequently encountered microstructures in a single crystal is a dendritic (tree-like) structure. Like a tree the dendrite is a branched structure with primary, secondary, tertiary, and even higher order branches as shown in Fig. 1.8 (from [3]). The microscopic length scales of dendrites of the order of a few μm to mm, such as primary and secondary arm spacings, control the segregation pattern that again influences many macroscopic properties of the material. For example, the cracking rate is higher in coarser microstructures and the cracking probability is a function of the primary spacings [10, 11]. It was also found that the primary branches of dendrites contribute to ductility and strength if they are in the direction of tensile stress [12].

Microstructures form while the system is not in equilibrium. Patterns are not selected based on equilibrium minimization of free energy, but depend on the dynamics of the microstructure formation process. Dynamic control of interface pat-

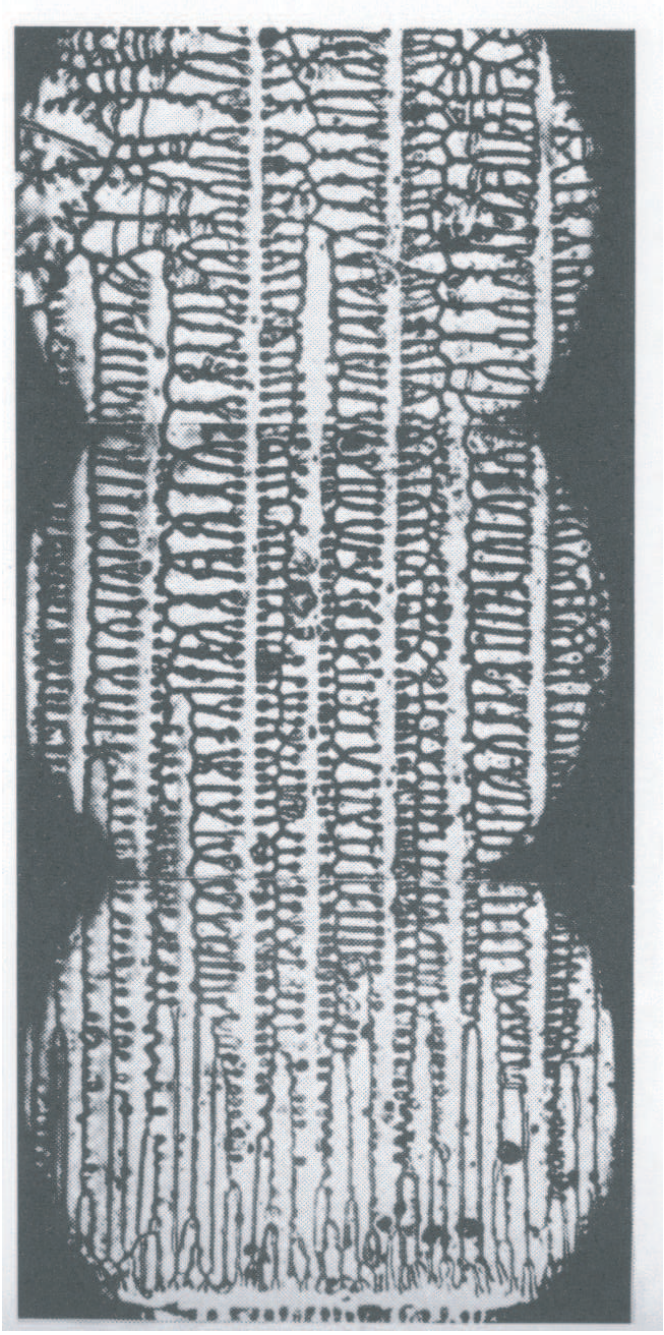

Figure 1.7: A directionally solidified single crystal (tin-1% lead alloy). The black lines indicate the segregation of composition resulted from dendritic growth. (from [1])

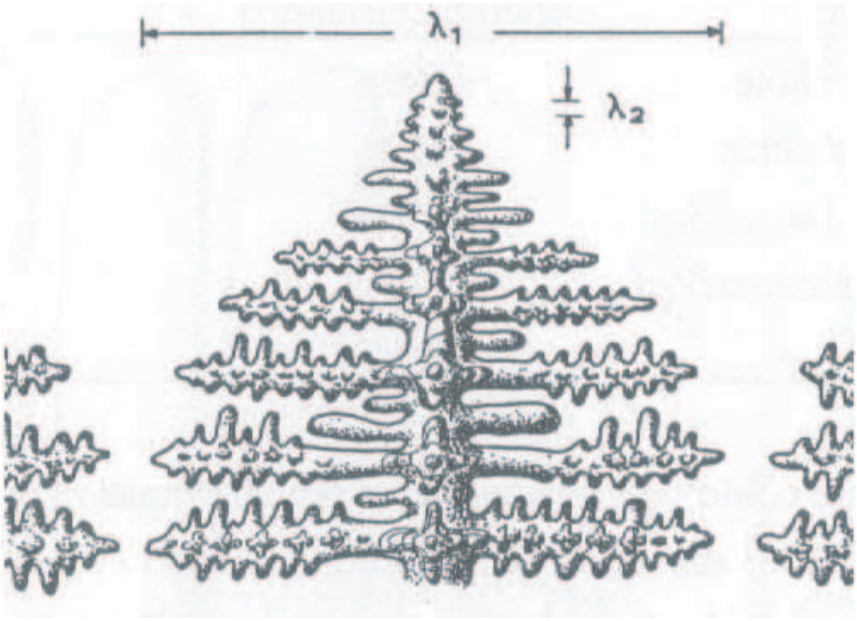

Figure 1.8: An illustrated branched structure of a dendrite growing upward. A primary trunk, secondary and tertiary branches are shown. λ_1 and λ_2 denote the primary and secondary arm spacings respectively. (from [3])

terns during solidification was investigated by Cummins and Losert [68]. In their study doublet cellular patterns are dynamically selected by applying spatially periodic perturbations to the planar interface during the planar-cellular transient. Also, dynamic control of the system in a non-equilibrium state has been used in other systems such as optical selection and control of microscale fluid flow patterns [13]. Here, we use this method to control grain boundary structure and intragrain dendritic structure, and to select grains of arbitrary orientations for detailed studies.

Since Jackson and Hunt introduced transparent organic materials that effectively solidify like a metal [14, 15], remarkable progress has been made in experimental study of microstructure formation because the dynamics of microstructure formation can be visualized directly under the microscope in these systems. Various types of organic materials such as pivalic acid [16, 17, 18], carbon tetrabromide [19, 20], and succinonitrile [16, 17, 18, 21, 22, 23] with an added impurity have been used as alloy model systems. With these model systems the evolution of interfacial instabilities has been studied in situ in thin samples under an ordinary optical microscope. Also, grain structures in polycrystalline materials has been studied with pure succinonitrile [24, 25, 26, 27]. The experimental results obtained from the study with these model systems were found to be applicable to metallic alloys [28, 29]. In most of the experiments discussed in this thesis we use succinonitrile (SCN) with coumarin 152 (C152) added in small concentration as a solute. The fluorescent dye C152 enables us to visualize the microstructure using fluorescence microscopy, to perturb the interface pattern, and to control the microstructure. For the study of eutectic growth we used CBr_4-C_2Cl_6.

The outline of this thesis is as follows. In Chapter 2 a brief background of alloy microstructure study is presented. Chapter 3 is a description of the instruments for microstructure imaging and control. First, we describe the alloy model systems used in this study. Second, the experimental setup for directional solidification study is described. It includes a motor-driven temperature gradient stage and apparatus of thermal perturbation used in control of microstructures. Then, basic principle and advantages of the imaging instruments, that are laser scanning confocal microscope and two-photon laser scanning microscope, are given. Last, the basic concept of holographic optical tweezer array and advantages of using it in microstructure study are discussed. In Chapter 4 we discuss the effect of temperature gradient on grain boundary motion of dilute binary alloys. We show that grain boundary orientation can be controlled through local heating. In Chapter 5 we present the results on control of cellular/dendritic primary spacings through local perturbations. It is shown that spatially periodic thermal perturbations during the initial instability create cellular/dendritic arrays with a desired primary spacing in the stable range. Moreover, perturbations can trigger a subcritical transition from one stable state to another stable state. We show that control of microstructure through perturbation allows us to investigate the modes of instability that limits the array stability of crystal growth patterns. In Chapter 6 we present experimental results on the role of anisotropy and sidebranches in stability of cellular/dendritic arrays. Comparison of cellular/dendritic arrays with different crystal orientations indicate that the anisotropy at the tip is an important factor of spacing selection. In Appendix A we present some preliminary results on imaging and control of eutectic structure.

In Appendix B we describe the sample preparation procedure. In Appendix C our method of image analysis is presented.

Chapter 2

Background

Grain growth associated with grain boundary migration is the most important process in the aging of the microstructure. The fundamental mechanism for grain growth is curvature driven grain growth [30], in which the surface tension difference between two grains caused by a curved boundary creates a difference in free energy that drives the atoms across the boundary. The overall result of boundary migration is to reduce the number of grains, thus increasing the mean grain size and reducing the total grain boundary energy.

Under the assumption of ideal grain growth, in which all grain boundaries have the same surface energy independent of boundary orientation relative to the crystal orientation, grain growth in a two-dimensional structure obeys the Mullins-von Neumann rule [31, 32]. The rule obtained through an integral of the curvature over the surface of a grain states that the growth rate of an individual grain depends only on the number of neighbors. Grains with more than six sides grow in area, and grains with fewer sides shrink. Grain growth also follows a parabolic growth law proposed by Burke and Turnbull [33], i.e. the mean grain size increases linearly in the square root of time. Recent study [34] has found that the neighbor-switching and the disappearance of two-sided grain are the only mechanisms of topological rearrangement of grain boundaries in a two-dimensional system. However, the grain

growth in a temperature gradient has not been studied experimentally.

The grain growth mechanism in 3-D is not fully understood. For example, no simple three-dimensional analog of the Mullins-von Neumann rule has been developed for grain growth. At present a widely accepted rule is that the growth rate of an individual 3-D grain depends on the number of faces. Grains with the number of faces larger than f_0 grow in volume, and grains with fewer faces shrink, where f_0 ranges from 15.7 to 16.1 according to numerical calculations [35, 36] and simulations [37]. Recent analytical results by Hilgenfeldt et al. [41] give 13.7 for f_0. Only a few experimental studies have investigated 3-D grain growth, mainly the distribution of grain sizes [38, 39]. The experimental system closest to grain growth is soap froths (foams). The dynamics of 3-D foam coarsening was experimentally investigated by Monnereau and Vignes-Adler [40], giving 13.5 for f_0. However, there has been no experimental observation of the dynamics of 3-D grain coarsening.

In Chapter 4 we present results on curvature driven grain growth and the effect of temperature gradient on grain boundary motion in 2-D and 3-D. As far as we know, this is the first time the dynamics of 3-D grain coarsening has been observed.

In Chapters 5 and 6 we investigate the dendritic microstructure within a single crystal. Although there have been extensive studies on the solidification pattern, there are still many questions to be solved. For example, we still do not have complete understanding of spacing selection mechanism in dendritic arrays. There have been no experimental results or theoretical predictions on the role of surface tension anisotropy in spacing selection.

In directional solidification, which we focus on in this study, a crystal grows in

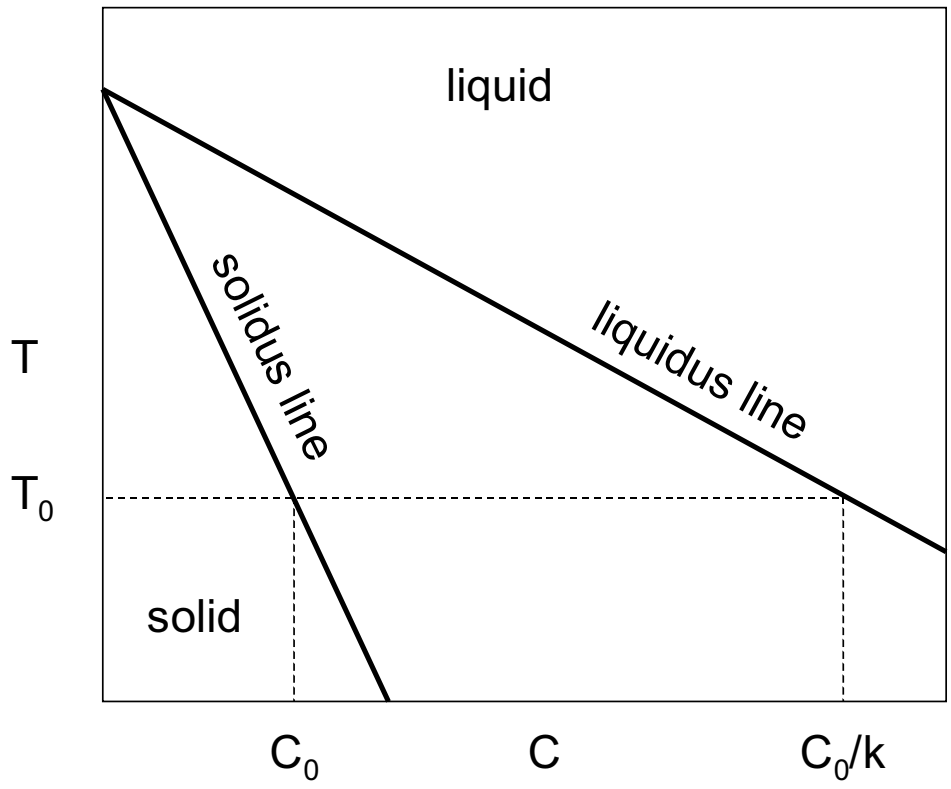

Figure 2.1: A typical phase diagram of dilute binary alloys. C is the concentration of the second alloy component, T is the equilibrium temperature, and k is the segregation coefficient.

a well defined direction. As a single crystal grows, heat is produced at the interface and solute is rejected from the interface. The growth of dendrites is primarily controlled by the transport of solute from the moving solid-liquid interface. The latent heat of fusion can be neglected since thermal diffusion is much faster than chemical diffusion.

Fig. 2.1 shows a typical phase diagram of dilute binary alloys. C is the concentration of the second alloy component and T is the equilibrium temperature. In the region between the liquid phase and the solid phase, phase separation occurs.

The line between the liquid phase and the phase-separation region is the liquidus line and the line between the solid phase and the phase-separation region is the solidus line. In dilute alloys the liquidus line and the solidus line are assumed to be straight lines. At the solidification front the alloy is phase-separated into solid with $C = C_0$ and liquid with $C = C_0/k$, where k is the segregation coefficient. Under the assumption of local thermodynamic equilibrium, the interface temperature T_i is given by [3]

$$T_i = T_m - mC - d_0 K T_m, \tag{2.1}$$

where T_m is the melting temperature of pure material, m is the slope of the liquidus line, C is the concentration on the liquid side of the interface, d_0 is the capillary length (characteristic length due to capillarity effect, $d_0 = \sigma/L$ where σ is the surface free energy density and L is the latent heat), and K is the local interface curvature. The second and third terms on the right hand side of Eq. (2.1) are the melting temperature depression due to the solute and the interface curvature respectively.

Most metallic alloys including our model system have microscopically rough interfaces due to the weak anisotropy in the interface energy, thus generating non-faceted growth patterns. However, the presence of even weak anisotropy leads to the growth of dendrite arms in specific directions. The origin of anisotropy is the capillary length, which is proportional to the surface stiffness τ as [42, 43]

$$\tau(\alpha) = \gamma(\mathbf{n}) + \frac{\partial^2 \gamma(\mathbf{n})}{\partial \alpha^2}, \tag{2.2}$$

where γ is the surface tension and α is the angle between the normal to the interface $\mathbf{n}$ and the pulling direction in the plane of 2-D sample. The surface tension for a

cubic crystal (up to the fourth-order cubic spherical harmonics) is represented in 3-D as [42]

$$\gamma(\mathbf{n}) = \gamma_0 \left[1 + \epsilon_0(n_1^4 + n_2^4 + n_3^4)\right], \tag{2.3}$$

where γ_0 is the isotropic part of the surface tension and ϵ_0 is the degree of anisotropy. The anisotropy has been measured for SCN as $\epsilon_0 = 0.0055$ [44]. n_1, n_2, and n_3 are the components of a unit vector $\mathbf{n}$. In general, dendrite trunks and arms tend to grow toward maximum surface tension. In thin sample directional solidification the crystal is constrained to grow in a plane. Therefore, the in-plane anisotropy is equivalent to a slice through the 3-D projection of $\gamma(\mathbf{n})$ (see Fig. 6.3).

Why is the solid-liquid interface not planar? The solute rejected from the solid during solidification piles up ahead of the solidification front and lowers the local equilibrium melting point. If the imposed temperature gradient at the interface is lower than the gradient of the melting temperature, the liquid in front of the solidification front exists below its equilibrium freezing temperature. This undercooling arising from constitutional effect, therefore known as constitutional undercooling, is a driving force for the development of the interfacial perturbations.

What determines the solidification pattern? Solidification morphologies are determined by the interplay of two effects acting at the solid-liquid interface. These are the diffusion of solute or heat, which tends to minimize the scale of the pattern, and capillarity effects, which tend to maximize the scale. The crystal morphologies observed are thus a compromise between these two tendencies. Another important factor in the crystal morphologies is the crystalline anisotropy of the surface tension.

The characteristic length scale of the microstructure is governed by the competition of a long diffusive length scale of the second alloy component and a short length scale introduced by surface tension. However, since the length scales differ by many orders of magnitude, both analytical calculations and simulations are difficult.

Over the last two decades, significant advances have been made in understanding fundamental aspects of dendritic microstructures. The onset of morphological instability in directional solidification, which was originally modeled by the classic Mullins-Sekerka instability [45], was studied in Warren-Langer time dependent linear stability analysis [46]. By analyzing the morphological stability of the planar interface during the transient build-up of the solute boundary layer, and by taking into account that the instability takes time to grow from natural modulations to until it becomes observable, it predicted the onset instability wavelength, in good quantitative agreement with experiments [47, 48, 49].

One of the main achievements of using organic model systems was the discovery of the critical role of crystalline anisotropy in interface dynamics. Experiments employing the ability to control the orientation of the crystal grown in a thin sample showed that with the $\langle 100 \rangle$ direction oriented parallel to the direction of temperature gradient the stable cellular/dendritic structures are obtained, whereas with $\langle 111 \rangle$ direction oriented normal to the sample plane a seaweed structure with no preferred growth orientation is observed due to no effective in-plane anisotropy [42, 43]. It was also found that cellular structures are linearly unstable in the absence of crystalline anisotropy, except in a very narrow range of velocity near onset of instability [50].

Much recent progress has been made to characterize some aspects of the in-

terface pattern of arrays of cells or dendrites, such as the shape of the dendrite tip, and the role of noise in sidebranching [51, 52]. However, few models exist for the spacing between cells and dendrites, even though it is one of the key characteristic features of the interface pattern.

One model by Spencer and Huppert [53, 54] develops a connection between the interdendritic spacing λ and the roughly parabolic shape of a single dendrite tip. While the tip radius r of a single dendrite can not be inferred from surface tension and diffusion of the second alloy component (solute) alone [55], r is directly connected to λ for an array of dendrites. The tip radius determines the diffusion field of the solute and thus yields a minimum spacing λ_{Min}, at which neighboring dendrites affect each other so strongly that they overgrow each other. The tip radius r increases with increasing λ. Since tips with too large radius are unstable, the maximum possible spacing λ_{Max} is given in this model by the marginal stability for a dendrite tip. Larger spacings would lead to a tip splitting instability.

Simulations by Lu and Hunt [56] of arrays of dendrites include the effect of surface energy and of neighboring dendrites. The simulations compute smooth shapes without sidebranches and predict a lower limit for λ for both cells and dendrites and an upper limit for cells. For dendrites the upper limit is suggested to be twice the lower limit.

For analytical descriptions, further simplifications were needed. A stability analysis of dendritic arrays was carried out by Warren and Langer [57]. The theory models dendritic arrays as rows of parabolic tips, which serve as sources of the second alloy component. The tip radius is determined from surface free energy

considerations, using microscopic solvability theory. These calculations, derived for the limit in which dendrites only interact weakly, also ignore the role of sidebranches. The model yields a range of stable spacings, and indicates that period doubling is the most unstable mode of the system. The existence of the most unstable mode and the assumption of a range of stable primary spacings used in the Warren-Langer stability analysis have been confirmed by experimental observations [58, 59, 22, 60]. The prediction of average primary spacing was made based on the model of history-dependent selection of the primary spacing, in which dendrites are continuously eliminated during the long transient from the initial morphological instability of the planar interface until the steady state with every spacing being in the stable range. Spacing selection and array stability are discussed in Chapter 5 and 6.

Sidebranching was not included in any of the calculations. Indeed, the nature of the sidebranching mechanism is still somewhat uncertain: Both a noise-amplification mechanism [61] and nonlinear global oscillations [62] have been proposed. Earlier experiments showed that noise can trigger sidebranching under many circumstances [63, 64]. However, van Saarloos [65] and Caroli [66] predicted that tip oscillations can occur, caused by strong coupling between tips and sidebranches. Recently, similar oscillatory modes of the dendrite tip have been observed in simulations [67]. Sidebranches become visible close to the tip and are synchronized in space and time, if created by tip oscillations.

The relationship between sidebranching and the dendritic spacing has not been studied directly, but studies of the cell to dendrite transition provide important insights. Experiments by Georgelin and Pocheau [23] showed that an increase of

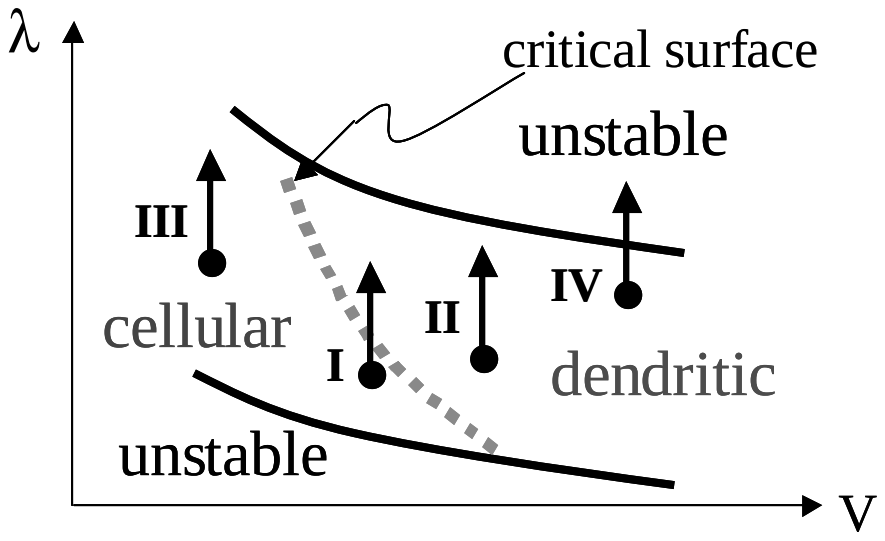

Figure 2.2: Schematic phase diagram of the solid-liquid interface pattern as a function of growth speed V and interdendritic spacing λ.

the thermal gradient at fixed growth speed and spacing enhances sidebranching. This is opposite to the well-known primary effect of the thermal gradient stabilizing the growth front by narrowing the isothermal lines. No jump of order parameter (maximum sidebranching amplitude) is observed at the transition to sidebranching, indicating that the sidebranching instability is supercritical for the parameter range investigated in their study.

A schematic phase diagram based on experimental observations [22, 60] and consistent with numerical results [56, 67] is shown in Fig. 2.2. It shows the solid-liquid interface pattern as a function of growth speed V and interdendritic spacing λ. A range of λ of cellular and dendritic arrays is stable at a given V, and the stable λ decreases with increasing V. The transition from stable cellular to dendritic regions (critical surface marked as a dotted line) was found to be supercritical [23]. Within

the range of stable λ, the selected λ and structure exhibit strong hysteresis [16]. The arrows I, II, III, and IV indicate transitions from one state to another, and will be discussed in Chapter 4.

Chapter 3

Instruments for Microstructure Imaging and Control

3.1 The Alloy Model System

For the study of grain boundaries and dendrites, we used the organic crystal succinonitrile (SCN) (Sigma-Aldrich, St. Louis, MO) with the laser dye coumarin152 (C152) (Sigma-Aldrich, St. Louis, MO) added in small concentration of ≤ 0.51 wt% as a dilute alloy model system, which was first introduced by Qian and Cummins. [21]. When solidified, SCN forms a body-centered cubic crystal. Because the solute C152 is a fluorescent dye, the local variation in composition of the alloy can be measured directly by fluorescence imaging. In addition, C152 can absorb sufficient energy under UV light or laser illumination to locally heat the sample. This local heating perturbs the interface pattern and thus the C152 concentration field as explained in more detail in [48, 68]. Such local perturbations through heating were first employed in solidification experiments by Qian and Cummins [21]. We use this local heating to perturb the interface pattern or to control the microstructure.

Because SCN-C152 degrades quickly under contact with air by absorbing water, the sample needs to be filled and sealed under vacuum (Appendix B). SCN with 99% purity is three times vacuum distilled ($P < 200$mTorr) and then mixed with C152 powder under vacuum. The mixture is filled under vacuum into precleaned glass capillaries (Vitro Dynamics, Mountain Lakes, NJ) with inner dimensions 100

μm $\times$ 2 mm $\times$ 30 cm or 200 μm $\times$ 4 mm $\times$ 30 cm. Since epoxies also cause degradation of SCN-C152, the capillaries are sealed with a torch while connected to the vacuum pump. Details of the sample preparation procedure are described in Appendix B.

In the study of eutectic growth (Appendix A) we used the CBr_4-C_2Cl_6 system, which solidifies into transparent, nonfaceted, cubic phases (α: hypoeutectic, face-centered cubic phase; β: hypereutectic, body-centered cubic phase) (sample prepared by a collaborator in France, S. Akamatsu). The alloys are prepared by mixing zone-refined and outgased CBr_4 and C_2Cl_6 ($T_E = 84.4^oC$; $\lambda_m^2 V \approx 185 \mu m^3 s^{-1}$) [19]. Thin samples (8 mm x 70 mm x 12 μm) are filled under controlled Ar atmosphere ($\approx$ 10mbar), and sealed after a rapid cooling at room temperature. The amount of residual impurities in the samples is of about 10^{-4} (mole fraction) [20], and its influence on the phenomena shown in this study is weak, unless otherwise noted.

3.2 Directional Solidification Setup

In directional solidification, the material is solidified by pulling it through a linear temperature gradient. Therefore, it is important to have a well-established temperature gradient and an accurate control of sample movement.

A schematic of the temperature gradient setup is shown in Fig. 3.1. The glass capillary sample glued to a holder is inserted into an oil-filled stainless steel chamber that has two sapphire windows for visual observation of the microstructure. The

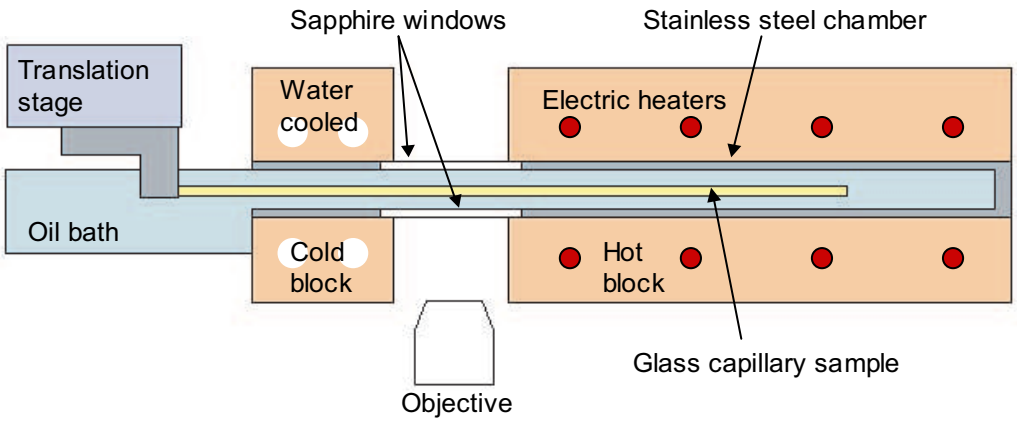

Figure 3.1: A schematic of a temperature gradient setup.

chamber is surrounded by hot and cold copper blocks and brought into good thermal contact with both blocks so that a linear temperature gradient is established in the chamber between the blocks. The gap between the hot and the cold blocks is 5mm. The glass capillary sample is immersed in light mineral oil, which approximately matches the index of refraction of the glass capillary, for uniform thermal conduction and good imaging. The whole system is enclosed by a acrylic box for thermal insulation.

The hot block is held at constant temperature by an electronic proportional temperature controller (YSI Model 72, Yellow Springs Instruments, Yellow Springs, OH). The range of available temperature is 30 °C to 120 °C with an accuracy of ±0.01K. The cold block is cooled with a water bath (Lauda RM6, Lauda GmbH, Lauda-Konigshofen, Germany). The available temperature range is 10 °C to 80 °C with an accuracy of ±0.01K. We measured the actual temperature profile in the chamber by pulling a thermocouple through the temperature gradient and found a linear temperature gradient across the region of observation. The actual tem-

perature gradient inside is about four times smaller than the one expected by the temperatures of the blocks because of constant heat loss to surroundings. For example, when the temperatures of the cold and hot blocks (with the gap 5mm) are 45 °C and 70 °C respectively, the actual temperature gradient is 12.7K/cm.

In the directional solidification experiments, the glass capillary holder is attached to a translation stage (CTC 462-1S by Micro Kinetics, Laguna Hills, CA) that is driven with a computer-controlled DC motor (MicroMo Electronics Inc., St. Petersburg, FL). The motor is controlled by a feedback motor controller (GCA/ McPherson Instrument, Acton, MA) connected to a PC and held at constant speed with an optical decoder with an accuracy of $\pm 0.5\%$. The motor is attached through a gearhead to the translation stage, which controls the sample position to within 0.5μm. The pulling speed can be set in 127 increments and ranges from 0.05μm/s to more than 100μm/s depending on the gearhead used. In grain growth experiments, the glass capillary sample is securely attached to the translation stage without the motor drive.

3.3 Laser Scanning Confocal Microscope

We use a laser scanning confocal microscope for imaging of grain boundaries and dendrites. The fluorescent dye C152 offers a chance to image the concentration field directly [48]. Fig. 3.2a shows a confocal microscope image of growing dendrites. As mentioned in Chapter 1, the solute is rejected from solid and piles up in front of the solidification front. The intensity profile along the green line directly gives the

concentration field in the liquid ahead of the dendrite tip as shown in Fig. 3.2b. A confocal microscope can image thin cross-sections of a thick sample and enables us to obtain the concentration field in 3-D. However, due to the mismatch of refractive index between liquid and solid, we could not image details of dendritic structures in 3-D. Imaging 3-D grain boundaries is still possible because of their relatively simple structure. Also, we use reflection confocal microscopy for imaging eutectic samples without any fluorescent dye. Due to its capability of obtaining 3-D structures confocal microscopy has been used in many areas of materials science research. For example, the 3-D pore structure of geomaterials was imaged by filling the void space with an epoxy doped with a fluorochrome [69]. Also, the liquid fraction of a liquid foam was three-dimensionally imaged by adding a fluorescent material to the liquid to study the foam structure [70] and the foam drainage [71]. However, the three-dimensional evolution of grain boundaries in polycrystalline materials have never been visualized until this study.

The principle of laser scanning confocal microscope is schematically presented in Fig. 3.3. A laser is reflected by a dichroic mirror (a mirror that reflects a particular band of wavelengths and transmits all others) and scanned across the sample by the movement of the mirror. Then, fluorescence emitted from the sample passes back through the dichroic mirror and comes toward the photomultiplier. The pinhole placed in front of the photomultiplier blocks out-of-focus light and allows only the light emitted from the focal point to be detected [72, 73]. Therefore, we can obtain a series of thin optical sections of a thick sample to reconstruct 3-D structures.

The resolution of the laser scanning confocal microscope depends on many

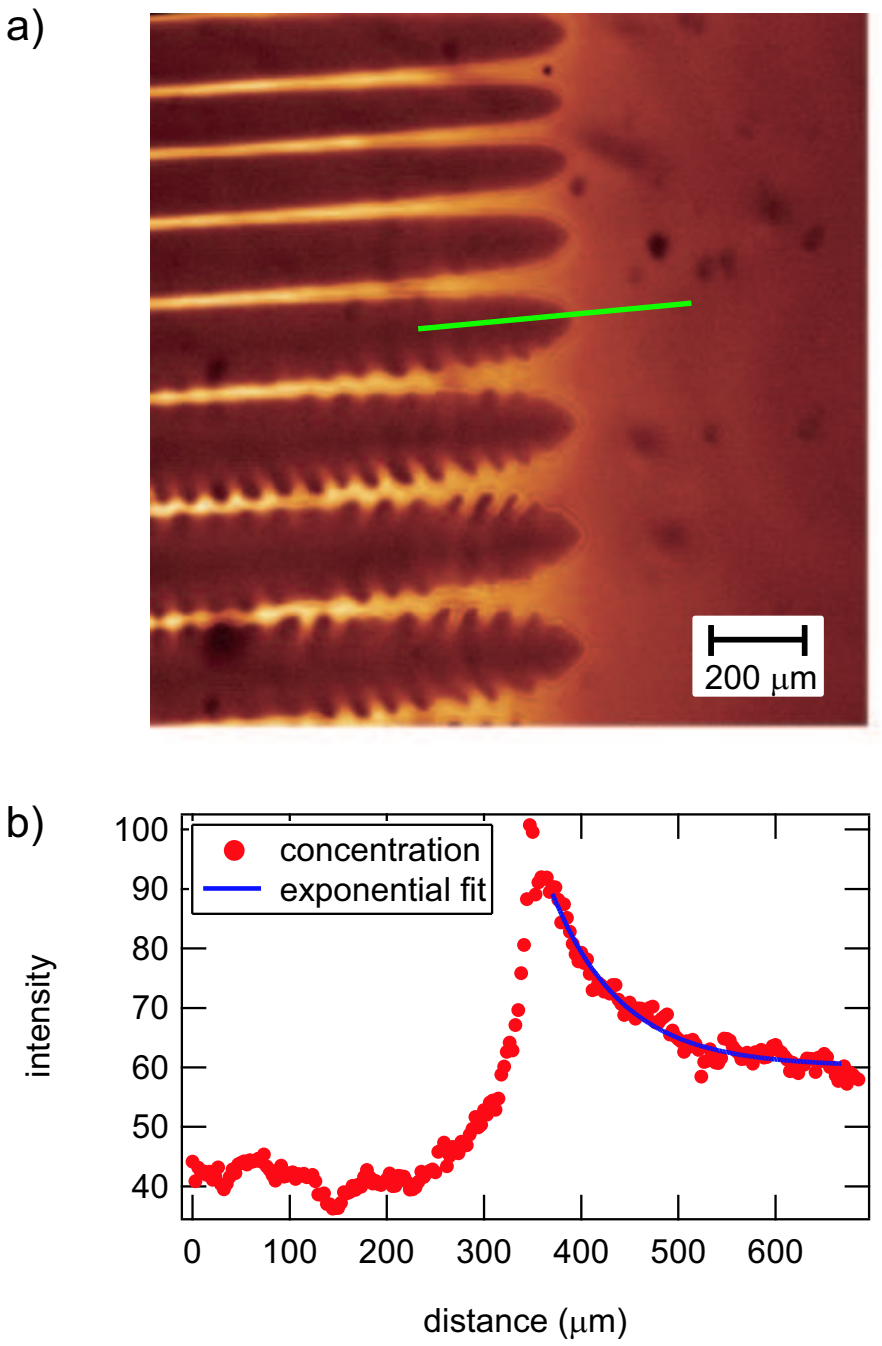

Figure 3.2: (a) A confocal microscope image of growing dendrites. (b) A plot of concentration field along the green line in (a). An exponential fit yields a diffusion length of approximately $78\mu m$ in the liquid ahead of the dendrite tip.

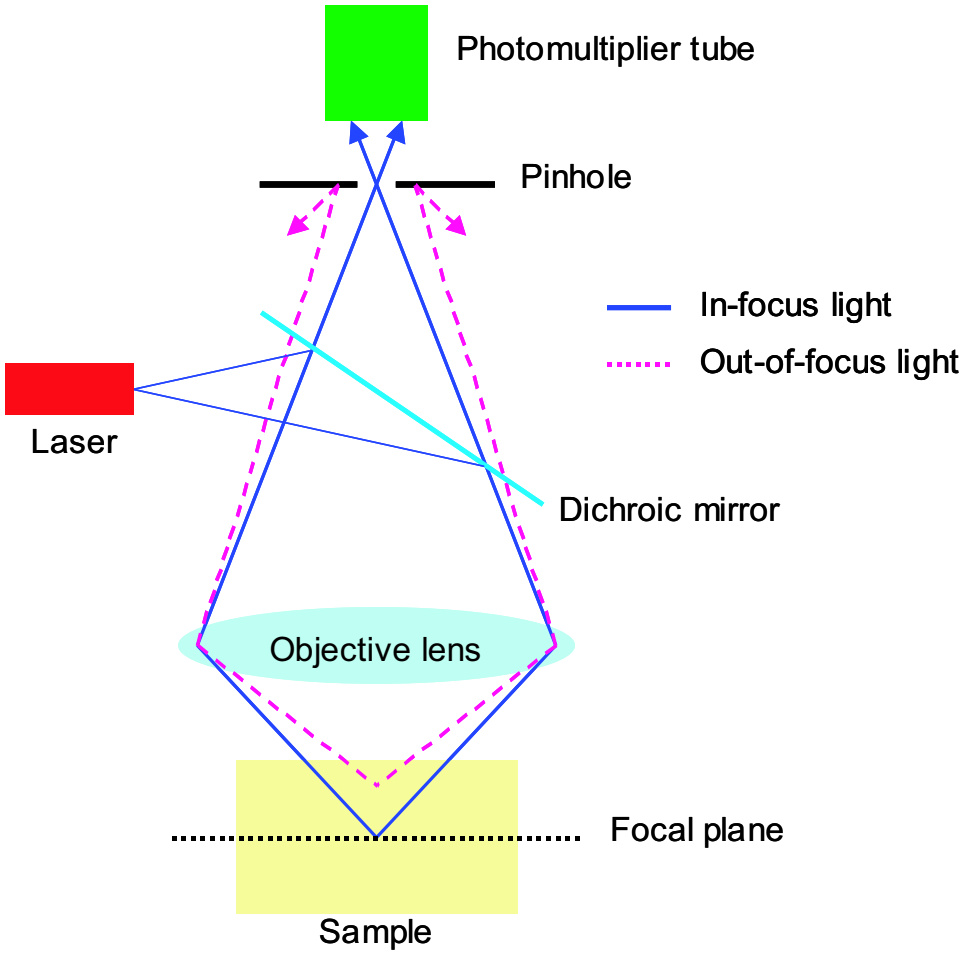

Figure 3.3: Schematic diagram showing the principle of a laser scanning confocal microscope.

factors. The lateral resolution is determined by the numerical aperture NA of the objective and the wavelength λ of the light as follows [74]:

$$R_{lateral} = \frac{0.4 \cdot \lambda}{NA}. \tag{3.1}$$

For this resolution to be fully appreciated we need to use a proper pixel size, which is determined by the electronic zoom factor and the scan format. The optimum pixel size is a third to a half of $R_{lateral}$.

The axial (the direction normal to the sample plane) resolution depends on the pinhole size in addition to the numerical aperture of the objective and the wavelength of the light. The optimum pinhole size d_{Airy} (the Airy disk) for the best axial resolution depends on the wavelength, the numerical aperture, the magnification M of the objective and the beam expansion factor B as [74]:

$$d_{Airy} = \frac{1.22 \cdot \lambda \cdot M \cdot B}{NA}. \tag{3.2}$$

B is dependent on the set beam expander, which determines the diameter of the laser beam to the lens of the objective: In our system B = 3.6 for beam expander number 6, B = 1.8 for beam expander number 3, and B = 0.6 for beam expander number 1. For the optimum pinhole size the axial resolution for NA$<$ 0.5 is given by

$$R_{axial} = \frac{1.67 \cdot \lambda \cdot n}{NA^2}, \tag{3.3}$$

where n is the index of refraction of the sample. We can see that using a high NA objective is crucial for the resolutions in confocal microscopy. For the best 3-D image the optimum axial pixel size, i.e. the step size between two optical sections, is half the axial resolution.

The laser scanning confocal microscope used in this study (Leica TCS SP2) has multiple laser excitation sources (458, 488, 514 and 543nm). In most experiments, a Nikon 10×, 0.25 NA dry objective is used due to its relatively long working distance (WD 10.5mm) despite its low NA. The laser of wavelength 458nm is found to be enough to excite C152 because of its broad absorption spectrum with the peak at 394nm. The beam expander 6 and the optimum pinhole size (1 Airy disk) are used for the best axial resolution (7μm for the objective used). With an in-plane resolution 512×512 pixels and 8-bit grayscale, images can be captured at a rate of up to 3 frames per second. Digital images collected by the microscope are processed by the Leica Confocal Software for three-dimensional reconstructions.

3.4 Two-photon Laser Scanning Microscope

In Chapter 4 we will use a two-photon laser scanning microscope to heat the interior of bulk samples. 3-D grain boundary structures are controlled through a local temperature gradient generated by this heating. In two-photon microscopy, two-photon excitation is confined to the focal region because the probability of two-photon absorption decreases as the fourth power of the distance from the focal plane [75]. Therefore, we can heat the interior spot of a bulk material by focusing and holding the laser beam at the spot.

This highly localized two-photon absorption process has been used in materials science for 3-D fabrication purposes. In two-photon photopolymerization [77], the laser is focused into a photopolymerizable liquid and due to the two-photon

absorption process solidification occurs only at the focal region. Therefore, a 3-D solidified structure is formed by placing the focal point in a controlled way. With this method, various micromachines [78, 79] and photonic crystals [80, 81, 82, 83] have been produced. While in these applications the two-photon absorption process is used for direct shaping of 3-D structures, in our study it is used for guiding the formation of 3-D structures in an area near the heating spot.

The principle of two-photon absorption process [75] is illustrated in Fig. 3.3a (from [76]). At high photon densities, two photons can be simultaneously absorbed (mediated by a virtual state) with a combined energy. Since each photon contributes a half of the excitation energy, the wavelength of the photon is about twice that required for single-photon excitation. For example, in our experiments two photons having a wavelength of 788nm combine to excite C152 in the 394nm excitation region.

The high photon densities required for the two-photon process is provided by a mode-locked pulsed femtosecond laser, which generates a stream of high-peak-power laser pulses. When the beam is focused, the beam intensity drops as the square of the distance from the focal plane. Because the energy is proportional to the square of the photon intensity, the probability of two-photon absorption outside the focal region decreases as the fourth power of the distance along the optical axis. This is illustrated in Fig. 3.3b compared with the case of single-photon absorption.

The two-photon laser scanning microscope used in this study consists of a scan head, a computer (the same ones as for the laser scanning confocal microscope), and a Tsunami Ti:sapphire mode-locked pulsed laser (82MHz pulse rate).

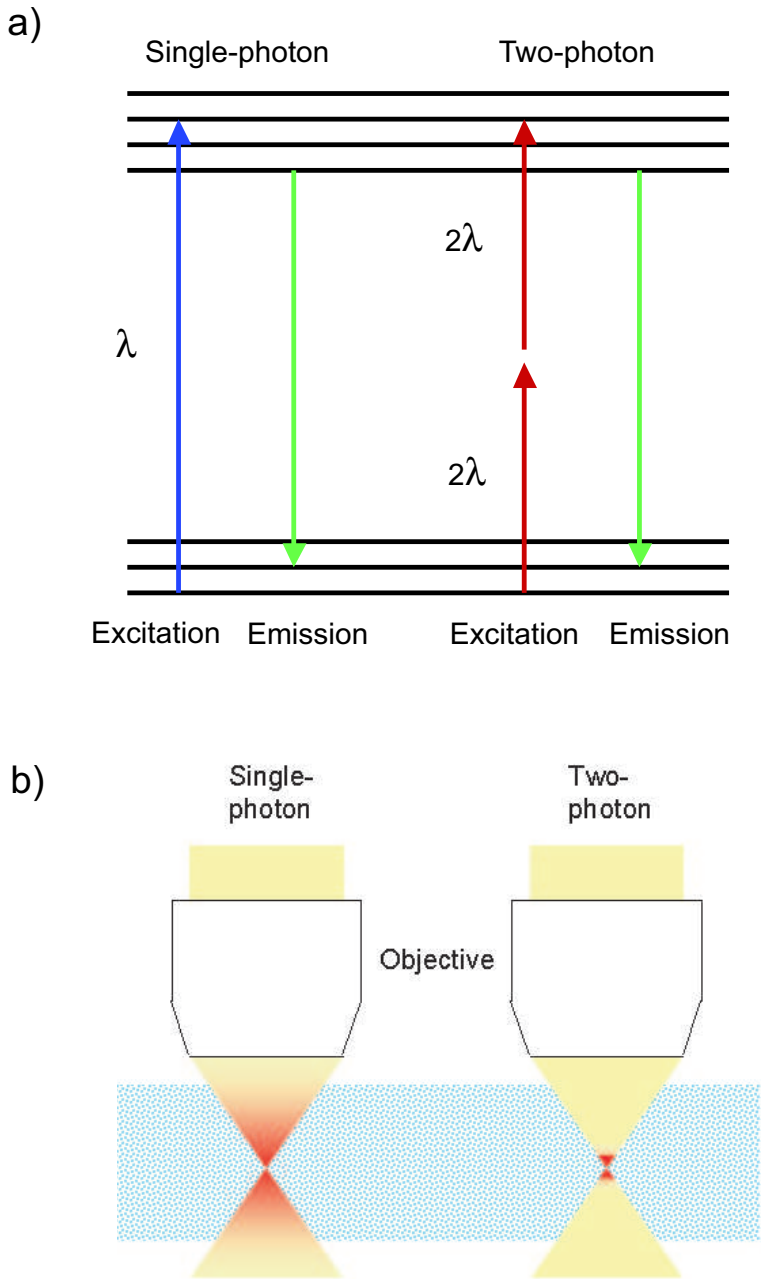

Figure 3.4: (a) Schematic diagram showing the principle of two-photon absorption process. (b) Two-photon absorption process occurs only at near the focal point thus heating the interior of a sample. (from [76])

The laser provides a large wavelength tuning range, from 690 to 1080nm, with pulses approximately 100 femtoseconds in length. In the experiments with samples containing C152, the wavelength is tuned to 788nm and the average power of 1.5W is used. Again, a Nikon 10×, 0.25 NA dry objective is used due to its relatively long working distance (WD 10.5mm). Imaging procedure is similar to that of confocal microscopy except for the beam expander and the pinhole settings. The beam expander is not used because it lowers the photon densities at the focal point. Since there is no out-of-focus light to block, we open the pinhole all the way.

3.5 Holographic Optical Tweezer Array

A holographic optical tweezer array generates multiple laser traps to trap and move micrometer scale particles. Due to its capability of manipulating particles, it has been widely used for nanofabrication [83, 84, 85, 86, 87] in the physical sciences. In our study we use the optical traps as independently movable spatio-temporal sources of local heating. With this technique we control dendritic spacings (Chapter 5) and trigger instabilities in eutectic growth (Appendix A).

Fig. 3.5 shows a schematic of a typical holographic optical tweezer array [88]. Holographic optical tweezers (HOT) first bounce the beam off of a spatial light modulator, which is a liquid crystal display designed to modulate the phase of the laser front. The modulator serves to introduce a complex diffraction pattern (Fig. 3.5(a)) to the laser light distribution, producing a hologram. This hologram then enters the objective lens to be focused to a diffraction-limited spot. Fig. 3.5(b)

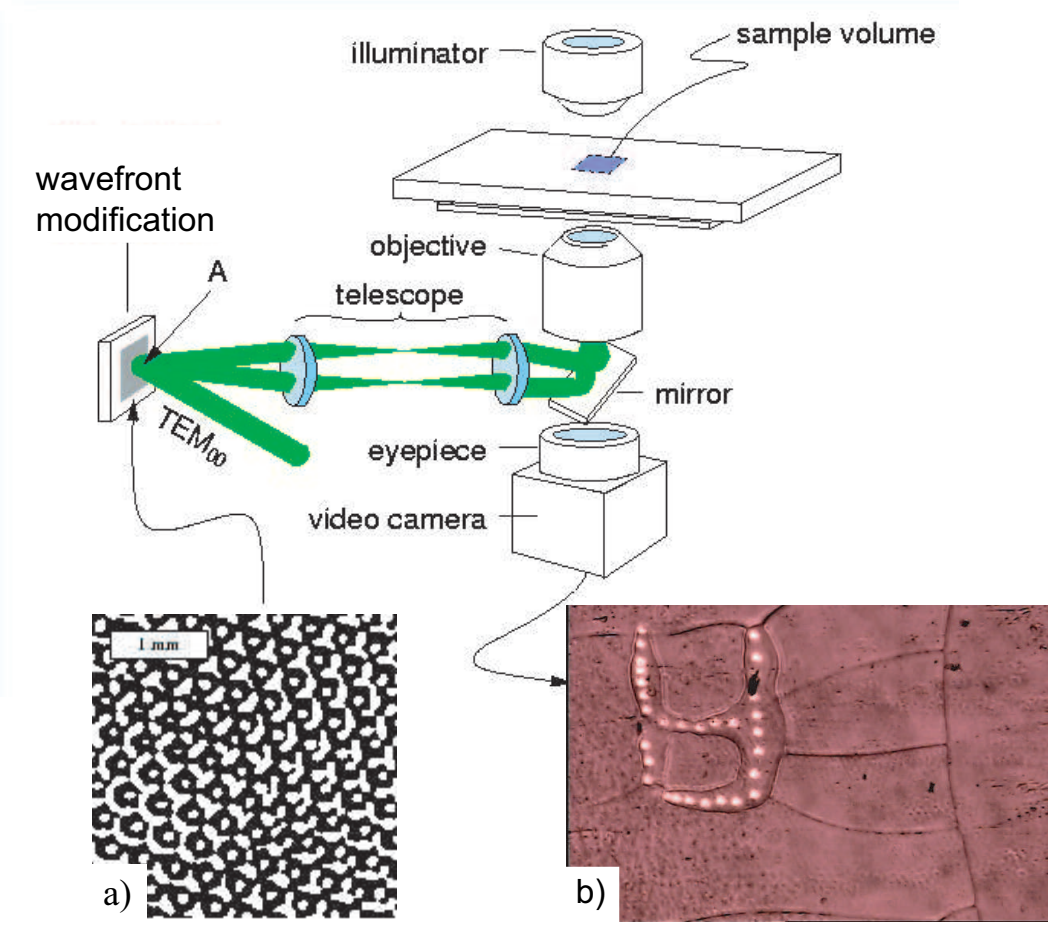

Figure 3.5: A schematic of a typical holographic optical tweezer array. a) The phase pattern generated by the programmable phase modulator(DOE). b) Melting around individual grains near the solid-liquid interface using multiple laser spots. (from [88])

shows multiple laser spots used to melt around individual grains near the solid-liquid interface.

The holographic optical tweezer array used in this study (Bioryx200 from Arryx Inc.) can create up to 200 independently movable laser spots. The range of the laser power is 0.2W to 2W, which is evenly distributed to the spots created. The laser with the wavelength 532nm is absorbed by C152 and CBr_4-C_2Cl_6. The sizes of the heated region depends on the magnification of the microscope objective. With 4x magnification objectives laser spot sizes are of the order of 10 μm.

Chapter 4

Controlled Dynamics of Grain Boundaries in Binary Alloys

4.1 Overview

Grain boundaries in polycrystalline materials have been extensively studied because of the importance of their effects on various material properties. While many properties are simply dependent on the average grain size, thus the total area of grain boundaries, grain boundary orientation also plays an important role in certain properties such as the creep fracture mechanism [6] and the crack growth direction [5]. Also, the electrical resistivity can be influenced by grain boundary orientation since grain boundaries scatter electrons and increase resistivity. In this study we focus on the effect of a temperature gradient on grain boundary motion. We show how we can control grain boundary orientations by generating a local temperature gradient. We also show the dynamics of 3-D grain coarsening imaged by a two-photon laser scanning microscope.

4.2 Experimental Detail

We use 100 μm $\times$ 2 mm $\times$ 20 cm and 200 μm $\times$ 4 mm $\times$ 10 cm sample capillaries filled with succinonitrile-coumarin152 (SCN-C152) (C=0.31wt%). For observation of grain coarsening the sample is melted and cooled rapidly to produce small grains

distributed uniformly throughout the sample as an initial state. Then, it is placed in a temperature gradient stage under a microscope. An optical microscope with a CCD camera is used to capture the two-dimensional (2-D) dynamics of grain coarsening with the 100μm-thick sample, and a two-photon laser scanning microscope is used to capture the three-dimensional (3-D) dynamics with the 200μm-thick sample. We use UV light (100W mercury lamp) to locally heat the two-dimensional sample. A two-photon laser scanning microscope is used to locally heat the quasi three-dimensional sample. The grain boundaries are extracted from the captured images and analyzed using our image analysis programs (Appendix C).

4.3 Results and Discussion

Normal Grain Growth at a Uniform Temperature: Fig. 4.1 shows two-dimensional grain growth at a uniform temperature, similar to the one observed with pure SCN by Palmer et al. [24, 25]. The grain boundary energy is independent of the orientation of the boundaries because all grain boundaries are wet. Since the surface tension forces acting at a trijunction must be in equilibrium, the angles between the boundaries strictly at the trijunction have to be 120 ° [2, 34, 93]. Some of the angles in our images do not look like 120 °, but when zoomed in, exactly at the trijunction the boundaries form 120 ° angle with high curvature. We observe that the grain growth satisfies the Burke - Turnbull law [33]:

$$\bar{A}(t) - \bar{A}(0) = K_A t, \tag{4.1}$$

where $\bar{A}$ is the average grain area and K_A is a constant which is proportional to the grain boundary mobility [25]. The average grain area grows linearly in time as shown in Fig. 4.2 (the fluctuations are due to measurement errors in extracting grain areas). The slope of the fit to the data yields $K = 3.53(\mu\text{m})^2/\text{s}$. This indicates our model system mimics metallic alloys in the realm of ideal grain growth.

Another indication is that the grains with number of sides larger than six grow and smaller than six shrink, satisfying the Mullins - von Neumann law [31, 32]:

$$\frac{dA}{dt} = K_N(N-6), \tag{4.2}$$

where A is the area of a grain, K_N is a constant which is proportional to the grain boundary mobility [25], and N is the number of sides of the grain. Fig. 4.3 shows the individual grain area change in time for ten grains. The grains with the same number of sides have similar slopes. Note that the slope of the curve changes when the number of the grain sides changes. The slopes, i.e. the grain growth rates, are obtained from fitting of linear portions of the curves (during which the grain maintains the same number of sides), and are plotted against $N-6$ in Fig. 4.4, which is in a good agreement with the Mullins - von Neumann law. The slope of the fit to the data yields $K_N = 3.27(\mu\text{m})^2/\text{s}$.

One interesting observation from this experiment is the metastability of a quadrijunction in the 2-D grain growth with a single surface energy, which has been pointed out by J.W. Cahn [93]. Fig. 4.5 shows shrinking of a usual four-sided grain. Two pairs of trijunctions merge separately as the grain vanishes, and then the two resulting trijunctions recede immediately due to the high curvature as shown in

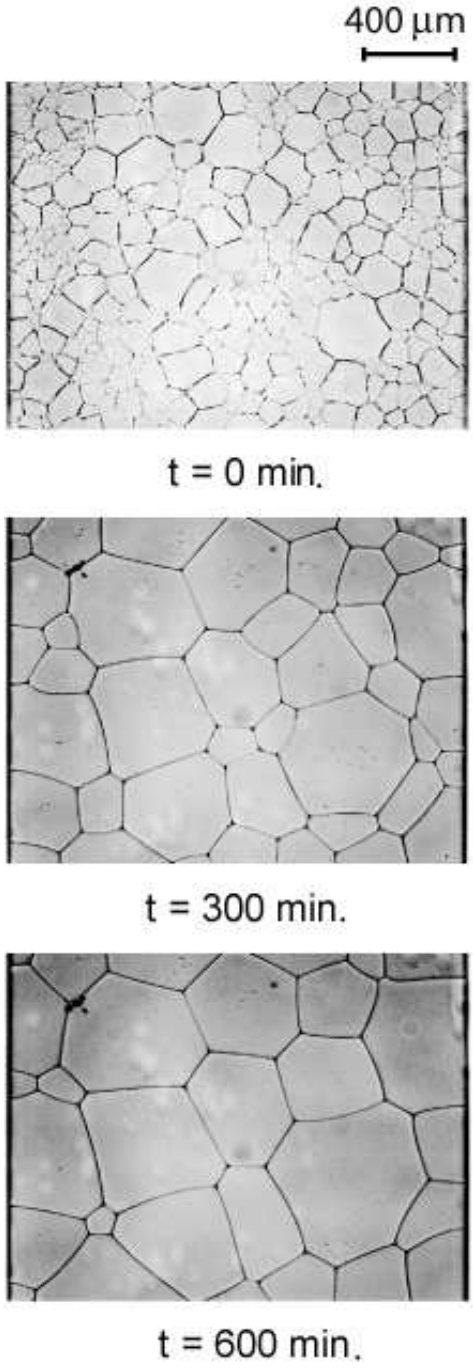

Figure 4.1: Ideal grain growth at a uniform temperature (T=55 °C). The grains with number of sides larger than six grow and smaller than six shrink.

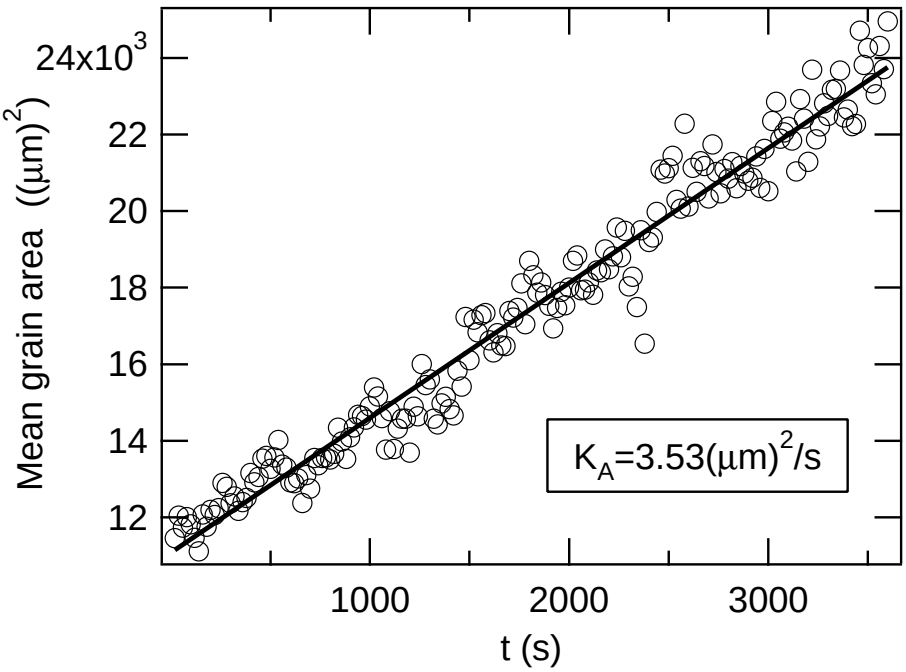

Figure 4.2: A plot of the average grain area vs. time. The fluctuations are due to measurement errors in extracting grain areas. The average grain area increases linearly in time. The black line is a linear fit.

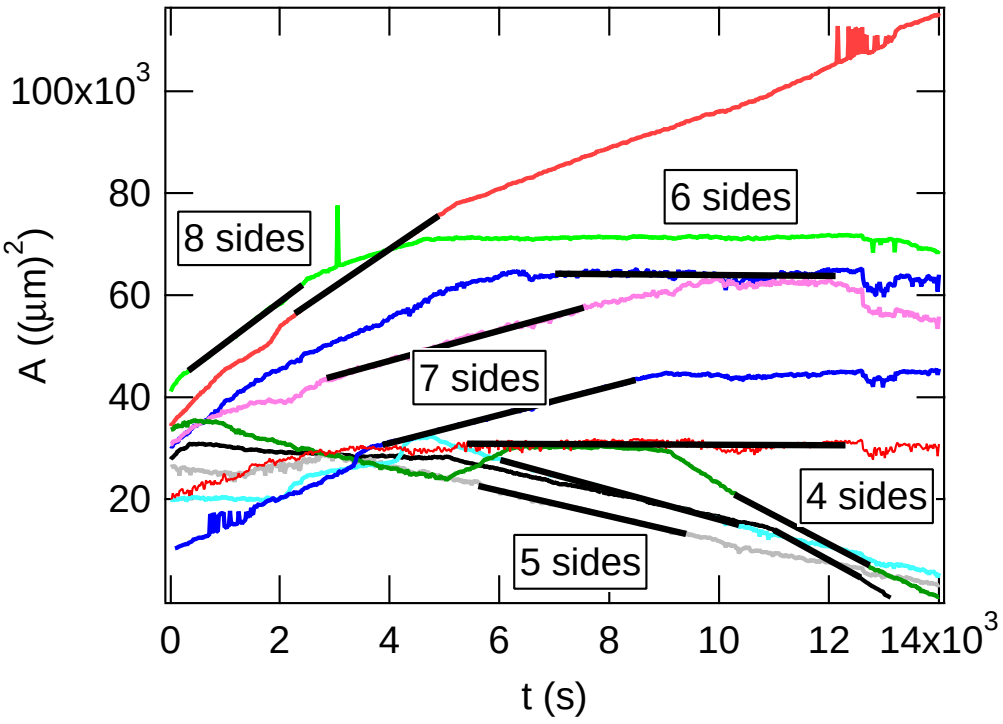

Figure 4.3: A plot of the grain area vs. time for ten grains. The grain with number of sides larger than six grows and smaller than six shrinks. The black lines are fits of the linear portions of the curves (during which the grain maintains the same number of sides).

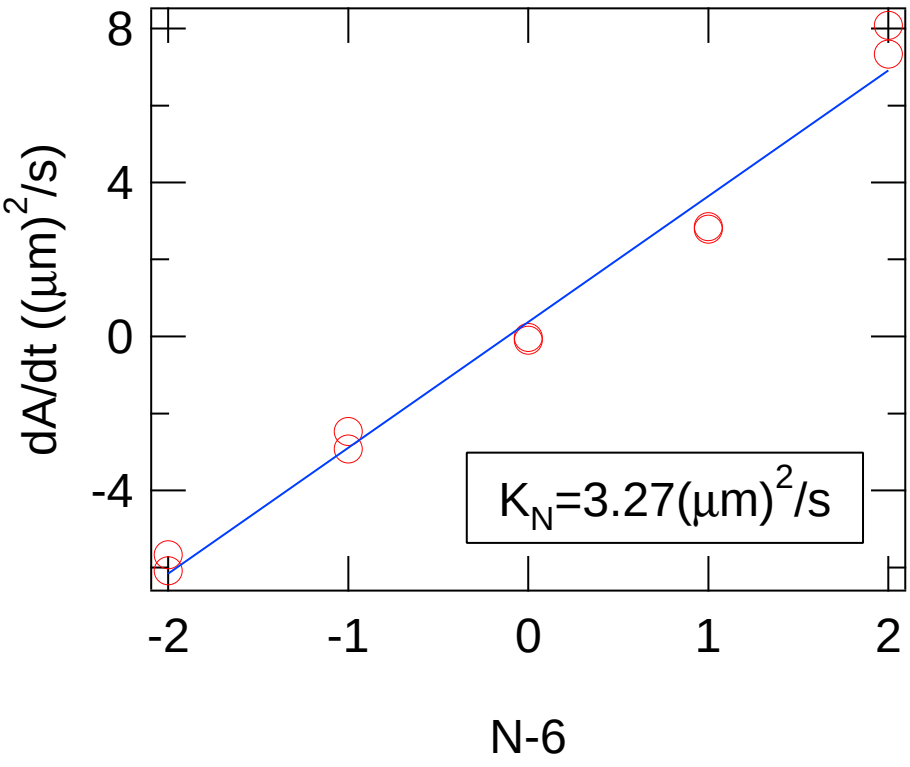

Figure 4.4: A plot of the rate of grain area change (the slope of the fit in Fig. 4.3) vs. $N-6$, where N is the number of sides. The blue line is a linear fit.

Fig. 4.6. However, when four trijunctions meet at one point as in Fig. 4.7, the resulting quadrijunction stays in that metastable state for several minutes before it finally dissociates into two trijunctions (Fig. 4.8). This is because the energy of the boundary between the two trijunctions created by the dissociation of the quadrijunction is high enough to temporarily keep the qudrijunction stable to dissociation. The quadrijunction eventually dissociates confirming that the trijunctions are the only stable line junctions when all the grain boundary energies are equal.

Grain Boundary Motion in a Temperature Gradient: When the sample is placed in a temperature gradient, in addition to curvature-driven grain growth, the grain boundaries drift toward the high temperature region (Fig. 4.9). Note that the apparent movement of grains in the direction of the temperature gradient is due to melting and solidification at grain boundaries, not motion of the bulk of the grains. The grains become more elongated in the temperature gradient direction as they move, indicating that the motion of the grain boundary is accelerated.

Using boundary extraction and tracking programs [developed using the Interactive Data Language (IDL from RSI, Inc.)], we obtain the velocity component V (of the grain boundary) parallel to the temperature gradient. This process is explained in Appendix C.

Curvature-driven grain growth is isotropic and generally slow compared to temperature gradient driven growth. While the boundary speed of disappearing grains due to curvature-driven grain growth is comparable to the one due to the temperature gradient, such events are rare and do not notably affect the time averaged V. Fig. 4.10 shows the plot of the average velocity V divided by the temperature

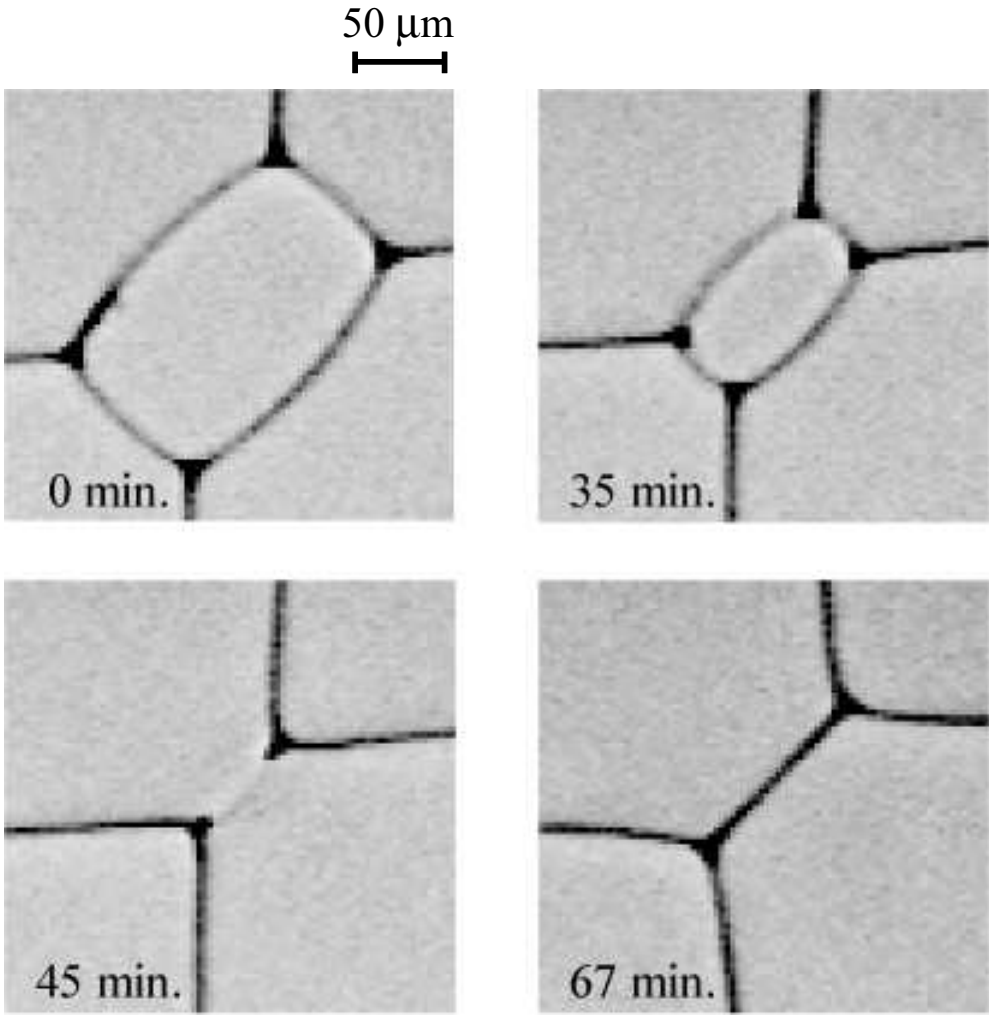

Figure 4.5: As a rectangular grain shrinks, two pairs of trijunctions merge. The resulting trijunctions move apart. (The picture has low quality because it has been magnified.)

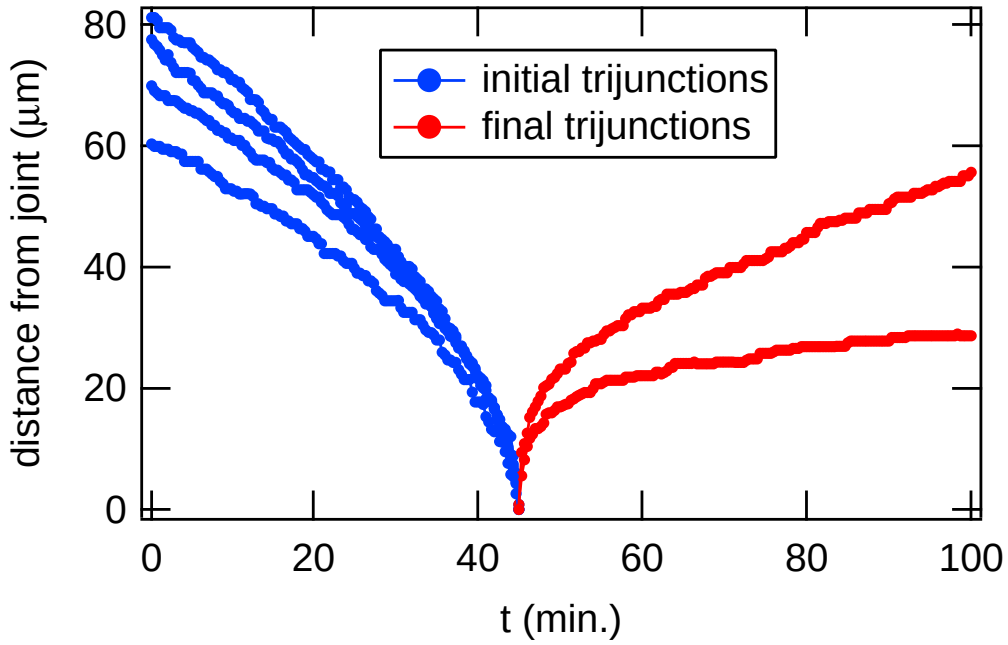

Figure 4.6: A plot of the distance between a trijunction and the merging point versus time for Fig. 4.5. After two pairs of trijunctions (blue lines) merge, two newly created trijunctions (red lines) immediately move away from the merging point.

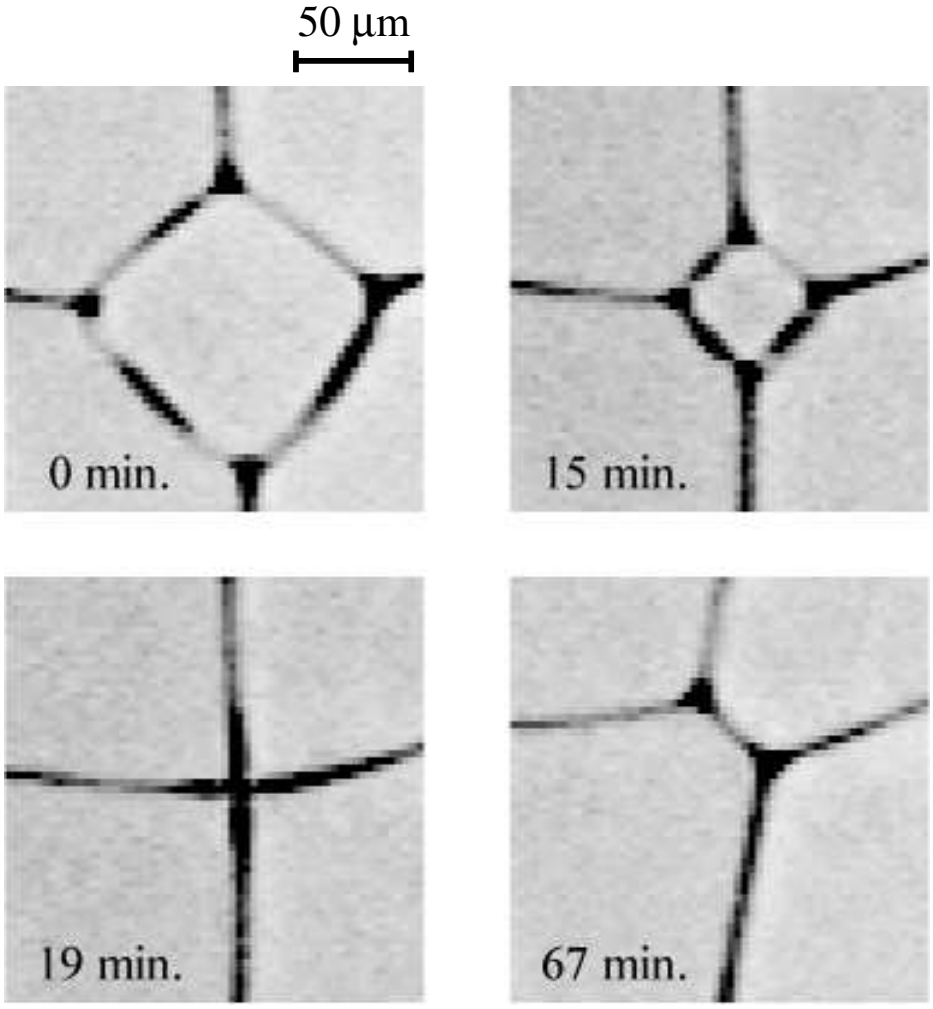

Figure 4.7: As a four-sided grain shrinks into a point, four trijunctions become one quadrijunction. (The picture has low quality because it has been magnified.)

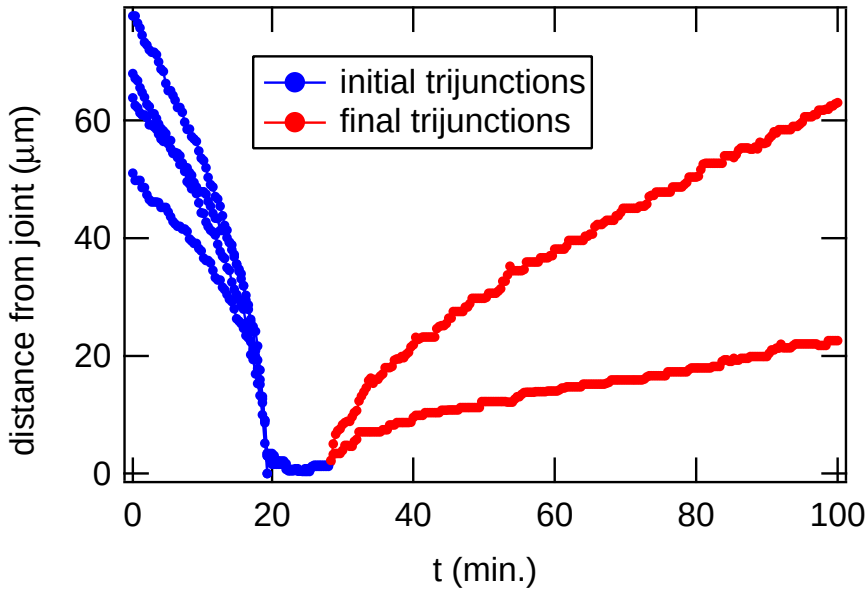

Figure 4.8: A plot of the distance between a trijunction and the merging point versus time for Fig. 4.7. The quadrijunction formed from merging of four trijunctions stays at the merging point for a while (blue lines) before it dissociates into two trijunctions (red lines).

gradient G as a function of local temperature T in the sample, which is obtained from the grain boundary position in the temperature gradient field. Six different data sets, which have either different temperature gradient or different range of local temperature, collapse on a single curve that can be fit to [95]:

$$V = \frac{DG}{(1-k)(T_0 - T)}, \tag{4.3}$$

where D is the solute diffusion coefficient in the liquid, T_0 is the melting point of pure SCN. We assume that the temperature dependence of D is negligible in this case, because the range of temperature investigated is narrow. The segregation coefficient k of SCN-C152 is 0.05 [48]. Fitting of all data points in Fig. 4.10 yields: $D = 300 \pm 30\ \mu m^2/\text{s}$ and $T_0 = 57.9 \pm 0.1$ K, in a good agreement with experimental values determined independently [48].

We suggest that measurement of grain coarsening in a temperature gradient may be useful to obtain a effective D and T_0 of the material studied. The equation for the drift speed V can be theoretically derived if the grain boundary is considered as a liquid channel in a solid subjected to a temperature gradient [94]. If we assume local thermodynamic equilibrium at the solid-liquid interface, the concentration at the cold side of the boundary is higher than that of the hot side, leading to a concentration gradient across the grain boundary (Fig. 4.11). Therefore, solute diffuses from the cold side to the hot side, which causes solidification at the cold side and melting at the hot side. Eq. (4.3) is then obtained from the solute balance at the solid-liquid interface [95].

Fig. 4.12 shows a four-sided grain shrinking in a temperature gradient. If

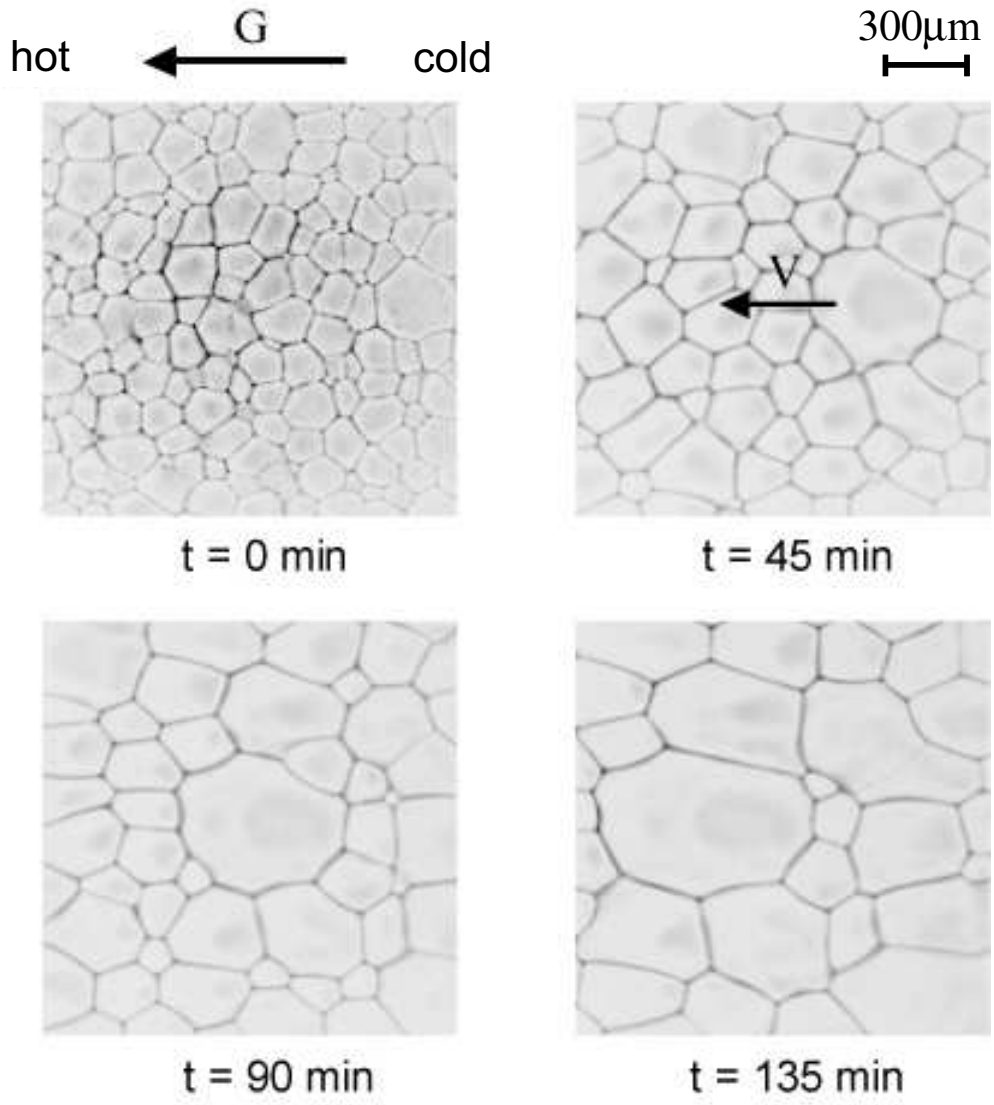

Figure 4.9: In a temperature gradient (G=2.5K/cm) the grain boundaries drift toward the high temperature region. As grains approach the hot side, they become larger and elongate in the direction of motion.

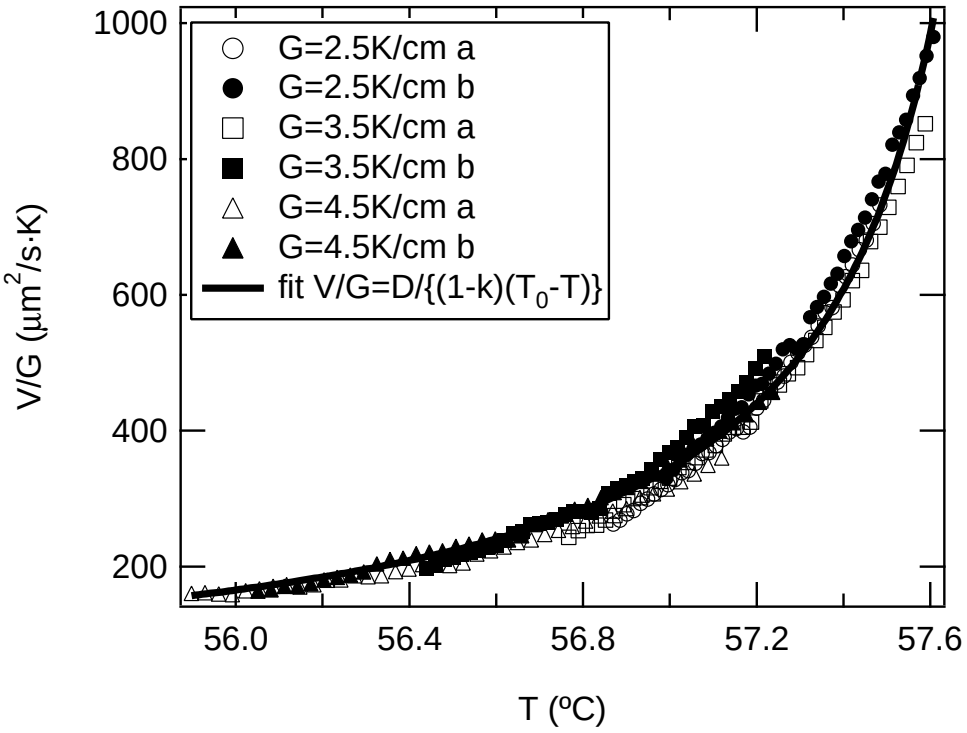

Figure 4.10: Speed of grain boundary motion divided by temperature gradient vs. local temperature for six different data sets. All data sets fall on the same curve fit to $V = DG/\{(1-k)(T_0 - T)\}$.

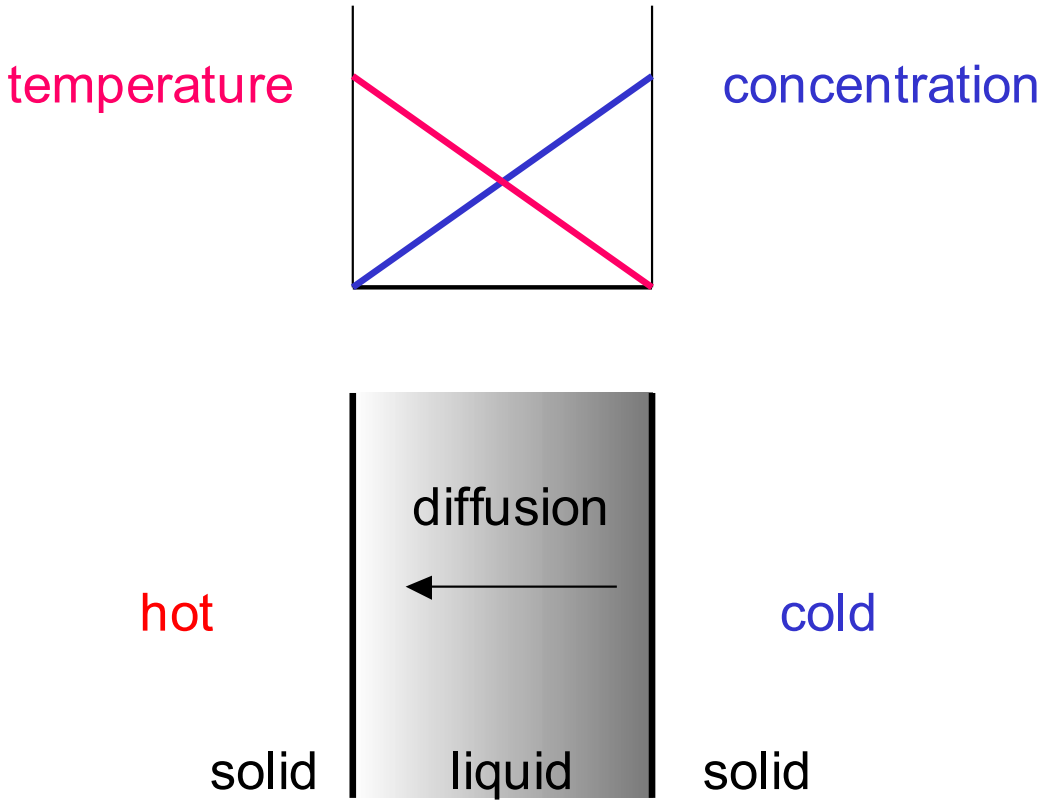

Figure 4.11: A schematic showing a grain boundary considered as a liquid channel. The concentration gradient across the wet grain boundary induces diffusion of the solute.

the average drift toward the high temperature region is subtracted, the shrinking behavior is similar to that of normal grain coarsening at a uniform temperature. When the effect of the drift due to the temperature gradient is separated out, the trijunctions follow qualitatively the same trajectories (Fig. 4.13) as in the case of a uniform temperature (Fig. 4.6). Log-log plots of the trajectories for the case of a uniform temperature and the case of a temperature gradient (again the effect of the drift is separated out) are shown in Fig. 4.14 (a) and (b) respectively. In both cases, after the transient near merging points the trajectories exhibit power law behaviors, $s \propto |t - t_0|^{\alpha}$, where s is the distance between a trijunction and the merging point and t_0 is the time when the trijunctions merge. The average α for the initial trijunctions are similar for both cases: 0.55 and 0.52 for the case of a uniform temperature and the case of a temperature gradient respectively. The average α for the final trijunctions are different for the two cases: 0.30 and 0.60 for the case of a uniform temperature and the case of a temperature gradient respectively. The difference in α for the final trijunctions between the two cases may arise from the difference in geometry of surrounding grains. More investigation is needed to explain this observation. Also, the temperature dependence of the surface tension may alter the balance of the boundary tensions at the trijunction influencing the trijunction movement. At present, the crude conclusion from our observations is that the motion of grain boundaries in a temperature gradient can be approximated by a superposition of the drift due to the temperature gradient and the migration associated with the normal grain coarsening.

Control of Grain Boundaries Through Local Temperature Gradients:

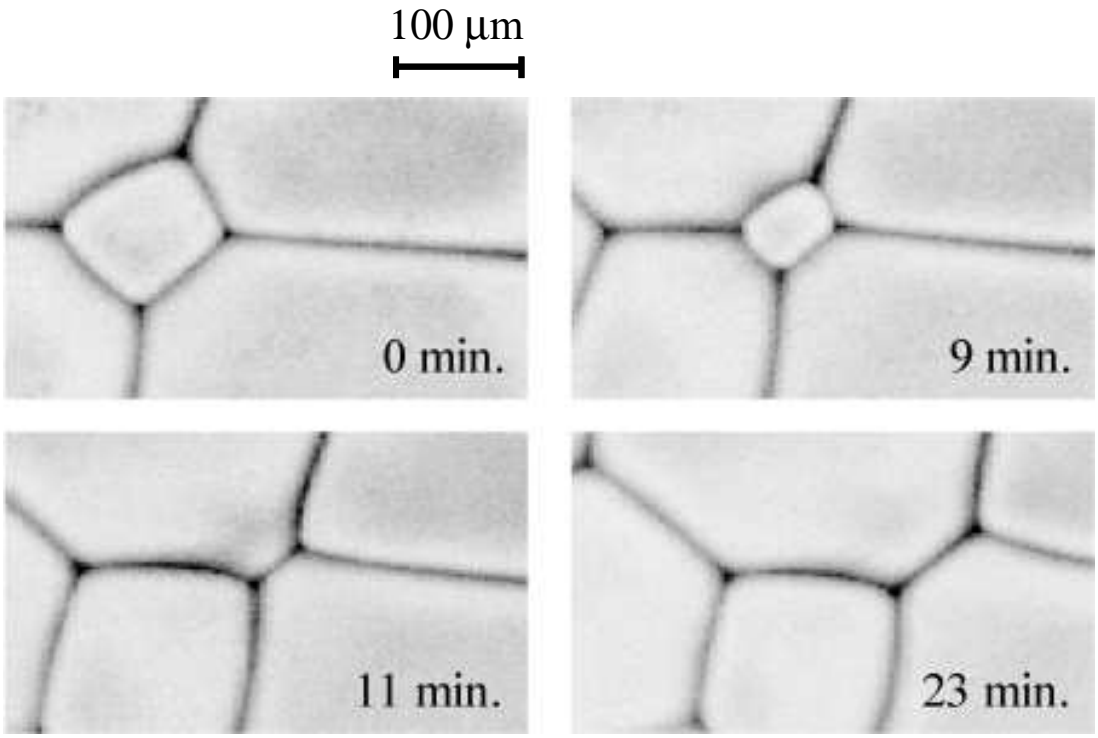

Figure 4.12: A four-sided grain shrinks while drifting in a temperature gradient. (The picture has low quality because it has been magnified.)

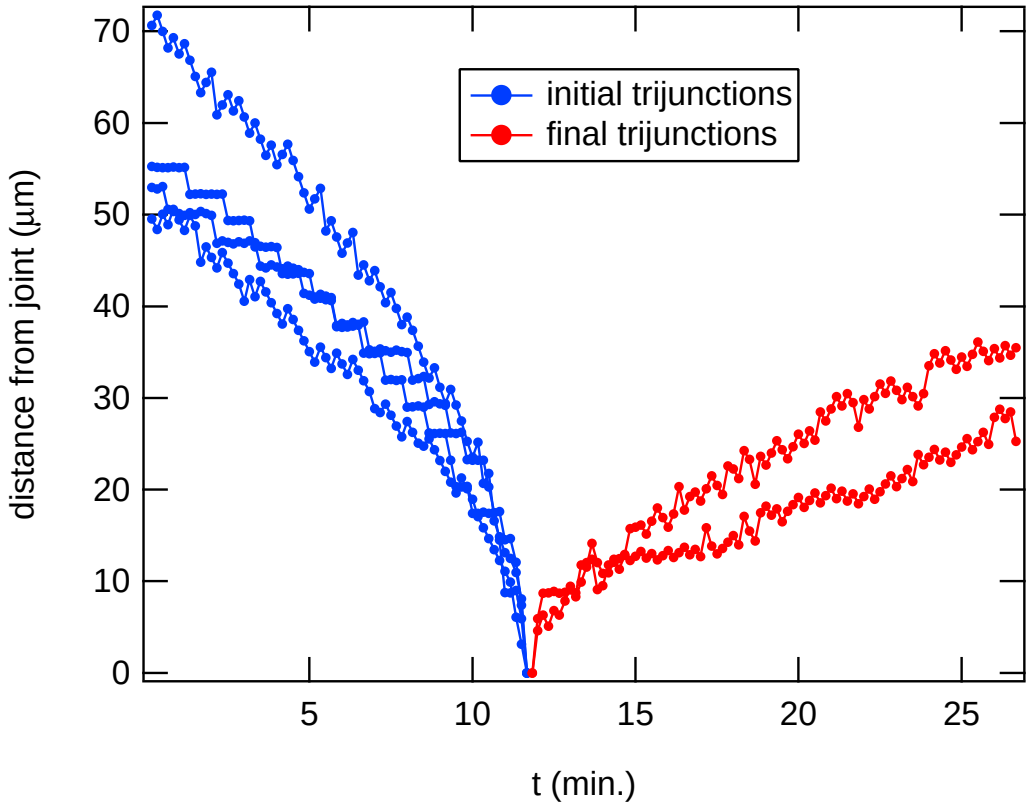

Figure 4.13: A plot of the distance between a trijunction and the merging point versus time after subtracting the effect of motion in a temperature gradient for Fig. 4.12. After two pairs of trijunctions (blue lines) merge, two newly created trijunctions (red lines) immediately move away from the merging point.

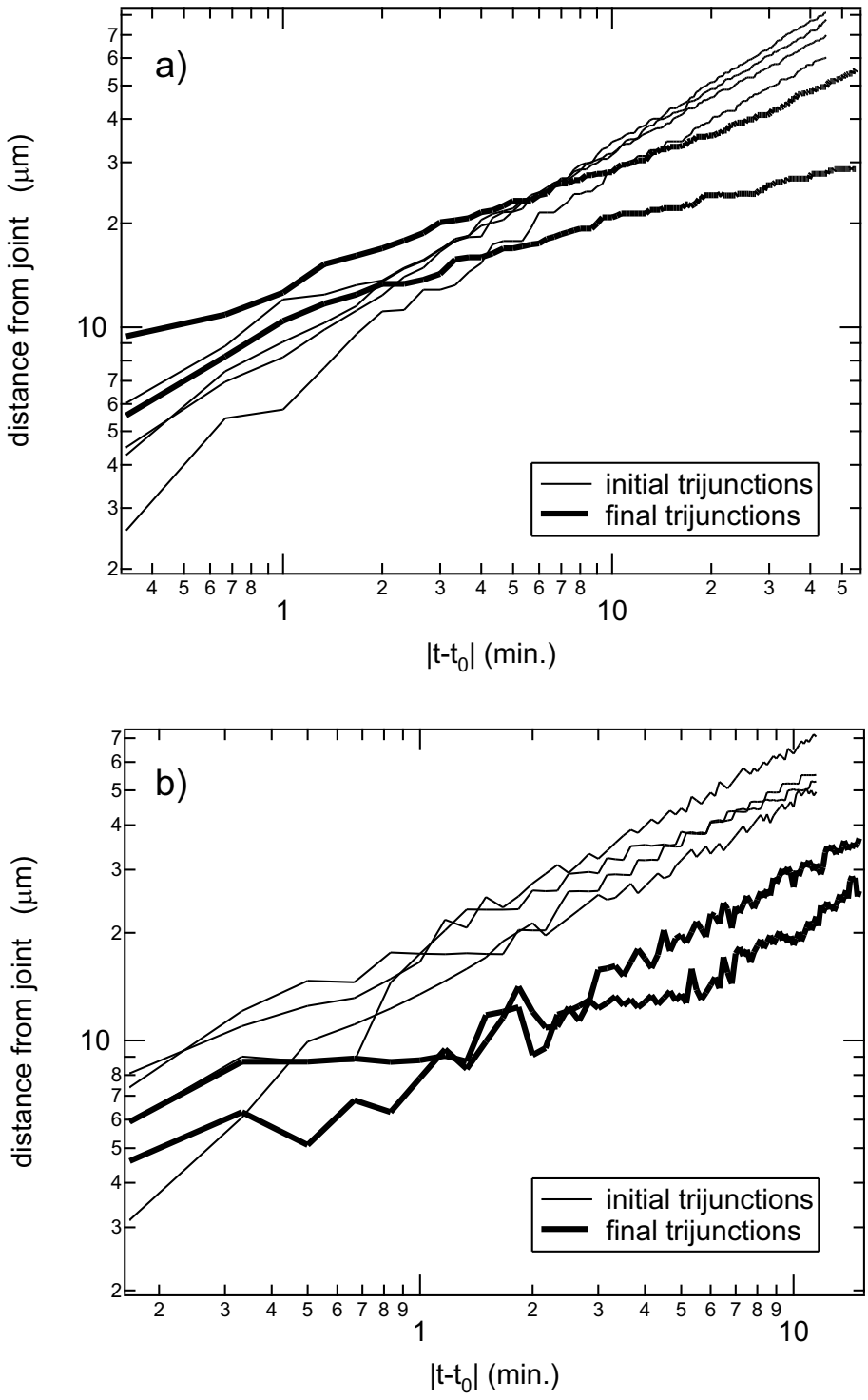

Figure 4.14: Log-log plots of the trajectories for (a) the case of a uniform temperature and (b) the case of a temperature gradient.

Since the speed of grain boundaries is proportional to the local temperature, grain boundaries tend to align with the temperature gradient. We can thus control grain boundary orientation by applying a local temperature gradient. Fig. 4.15 shows grain growth with a UV spot illumination applied to grains subjected to a uniform temperature. The UV spot locally heats the sample and creates a local temperature gradient around it causing grain boundaries to move toward the spot. Fig. 4.16 shows a plot of the mean absolute angle $\langle|\phi|\rangle$ between the grain boundaries and the radial line as a function of time. For comparison it also shows the plot for the case without UV spot heating. When there is no local spot heating, $\langle|\phi|\rangle$ stays around $\pi/4$ (the horizontal line), which means that the grain boundaries are randomly oriented all the time. In the case of spot heating, $\langle|\phi|\rangle$ decreases continuously in time, indicating that the grain boundaries gradually align along the radial direction.

We also measure the distance from the heated spot over which grain boundaries align. Fig. 4.17 shows a plot of $\langle|\phi|\rangle$ vs. R at four different time intervals. In each time interval, the circular range of radius 600μm around the heating spot is divided into ten concentric rings with same ΔR and $\langle|\phi|\rangle$ is averaged over each ring. We applied binomial smoothing on each curve to smooth out local fluctuations. Initially $\langle|\phi|\rangle$ for all R is about $\pi/4$, i.e. grain boundaries are randomly oriented throughout the sample. In the next time interval the boundaries adjacent to the heating spot starts to align in the radial direction. The curves in the following time intervals show that the boundaries adjacent to the heating spot align more strongly in the radial direction ($\langle|\phi|\rangle = 0$). We also note that as time goes on, more distant boundaries are affected by the local heating.

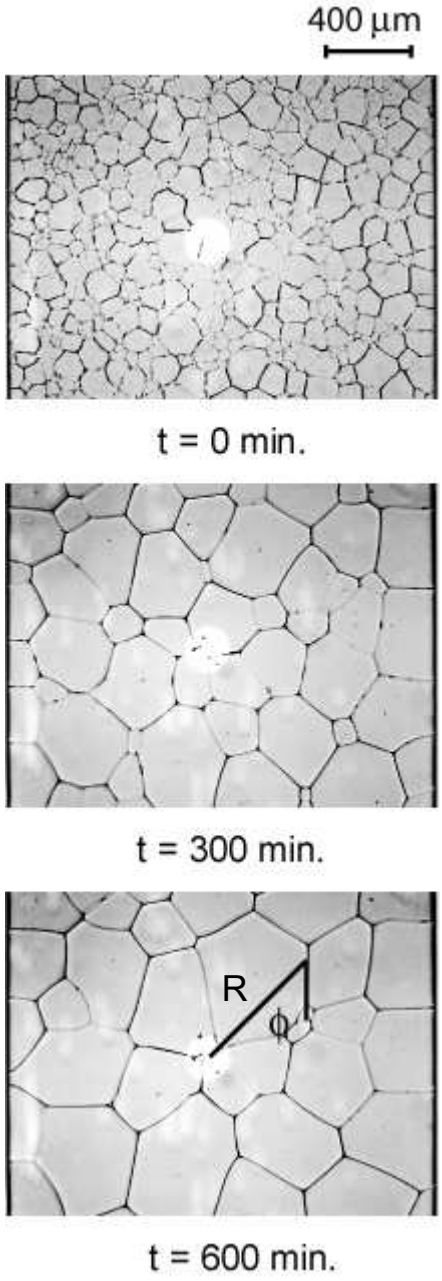

Figure 4.15: The UV spot heating causes the boundaries to align along the radial line. At each point on a grain boundary, we define ϕ as an angle between the tangential line to the boundary and the radial line from the UV spot. R is the distance between the center of the spot and the point.

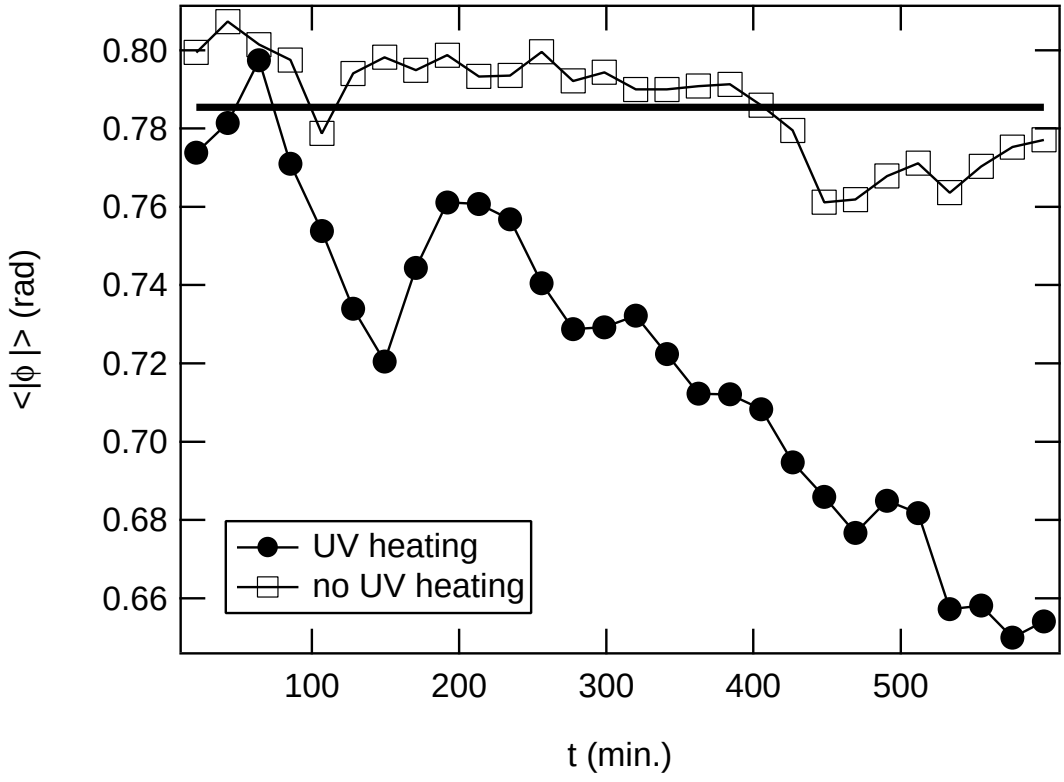

Figure 4.16: With the UV spot heating the mean absolute angle $\langle|\phi|\rangle$ decreases in time, while it stays around $\pi/4$ (indicated by a black line) in the absence of UV spot heating.

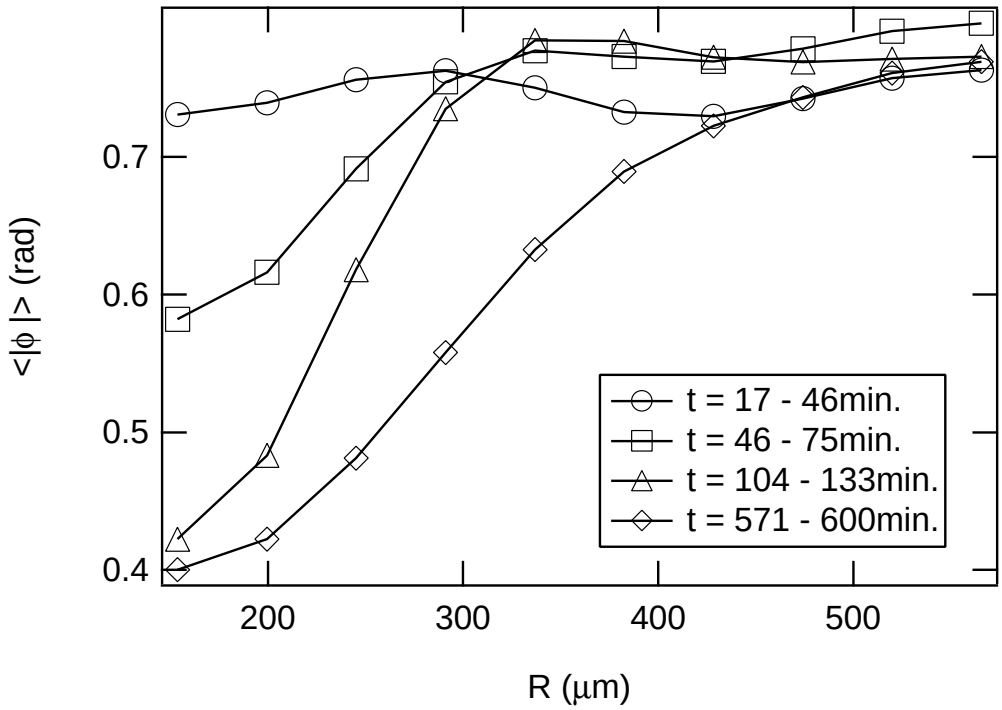

Figure 4.17: A plot of $\langle|\phi|\rangle$ vs. R at four different time intervals shows that the distance over which grain boundaries become radially aligned (lower $\langle|\phi|\rangle$) due to local heating increases with time.

Fig. 4.18 shows another example of controlling grain boundary orientation with local heating. A UV line illumination is applied to grains in a uniform temperature. The grain boundaries move toward the line from both sides, and become more perpendicular to the heating line. Fig. 4.19 shows a histogram of mean absolute angle $\langle|\theta|\rangle$ between the grain boundary and the heating line for initial and final states. The initially uniform distribution of boundary orientation changes into a distribution with peaks around 0 and $\pi/2$. Note that grain boundaries run along the heating line in the final state. Thus, placing the lines of heat source in desired orientations seems the most efficient way of controlling the grain boundary orientations.

We were also able to heat a spot in the interior of a 3-D sample using two-photon absorption, as explained in Chapter 3. Fig. 4.20 shows the change of grain structure around a heating spot in 3-D obtained by a series of alternate heating and imaging. Each heating is applied for five seconds at the same spot. After each heating we imaged 50 cross-sections around the spot to visualize the 3-D structure. We observe grain boundaries drifting toward the spot from all directions. The grains become three-dimensionally elongated and the boundaries become more parallel to the direction of the local temperature gradient.

4.4 Conclusion

In summary, we have studied experimentally how to control grain boundary orientations with a model binary alloy SCN-C152. In a temperature gradient the motion of the grain boundaries can be approximated by a superposition of normal grain

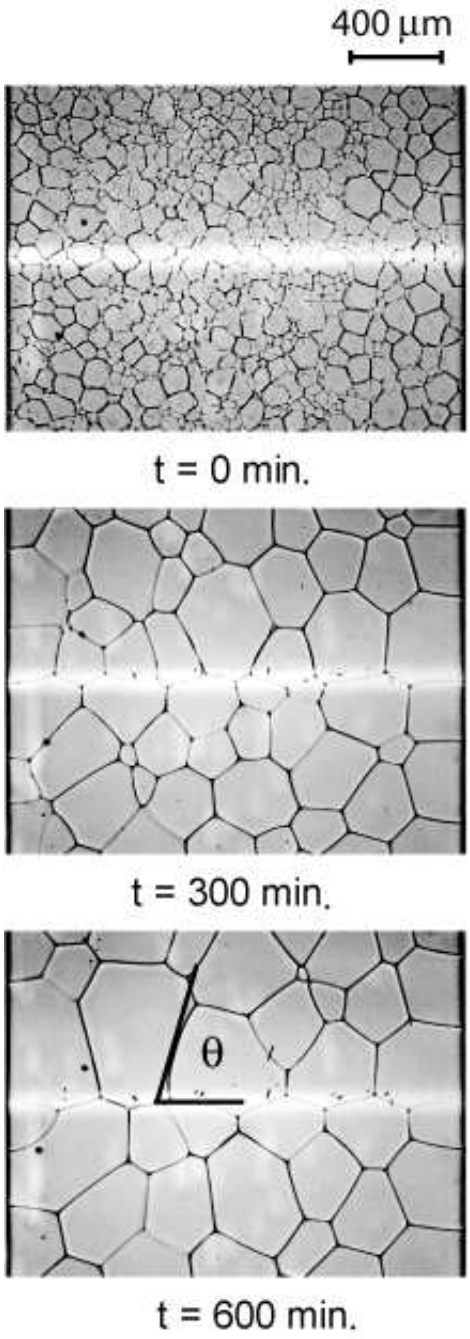

Figure 4.18: The UV line heating causes the boundaries to align along the UV line. At each point on a grain boundary, we define θ as an angle between the tangential line to the boundary and the heating line.

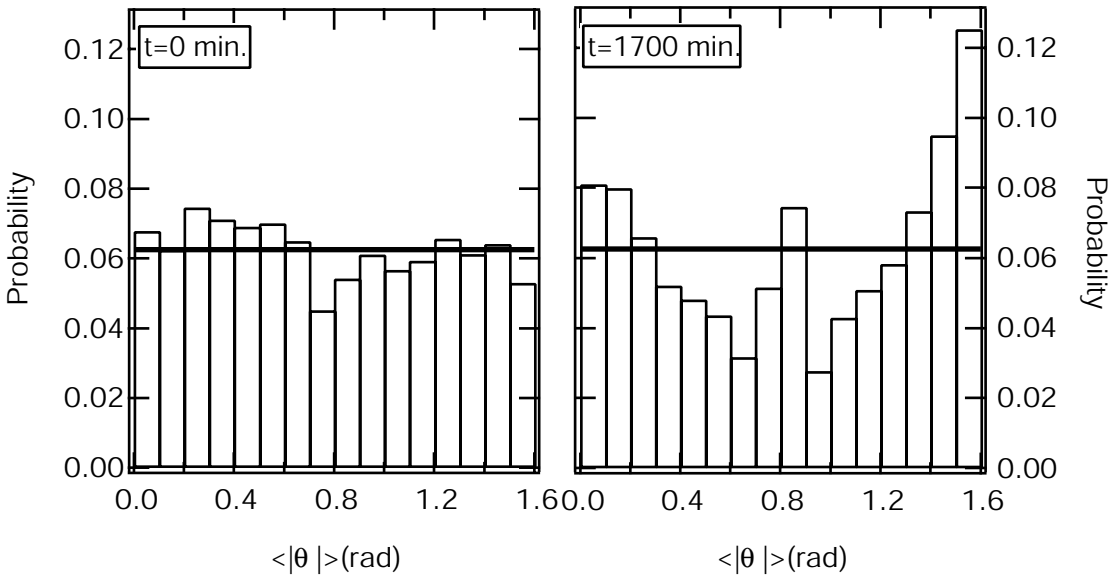

Figure 4.19: The histogram of the mean absolute angle $\langle|\theta|\rangle$ shows the development of preferred orientation due to the line heating. The black line indicates a uniform distribution.

growth and drift due to the temperature gradient. The drift speed V is a function of temperature gradient G and local temperature T as in Eq. (4.3). We use this drift to control the grain boundary orientations by applying local temperature gradients through UV heating in 2-D samples. We also demonstrate the potential of nonlinear absorption, the two-photon technique to control grain growth in 3-D samples.

There are still many interesting open questions in the dynamics of grain coarsening and control of grain structures that can be studied using the model binary alloy system. In 2-D grain growth, the power law behavior of trijunction movement has not been fully understood. In a temperature gradient, the temperature dependence of the surface tension may play an important role in the behavior of trijunction movement. Also, we need to check the validity of the assumption that

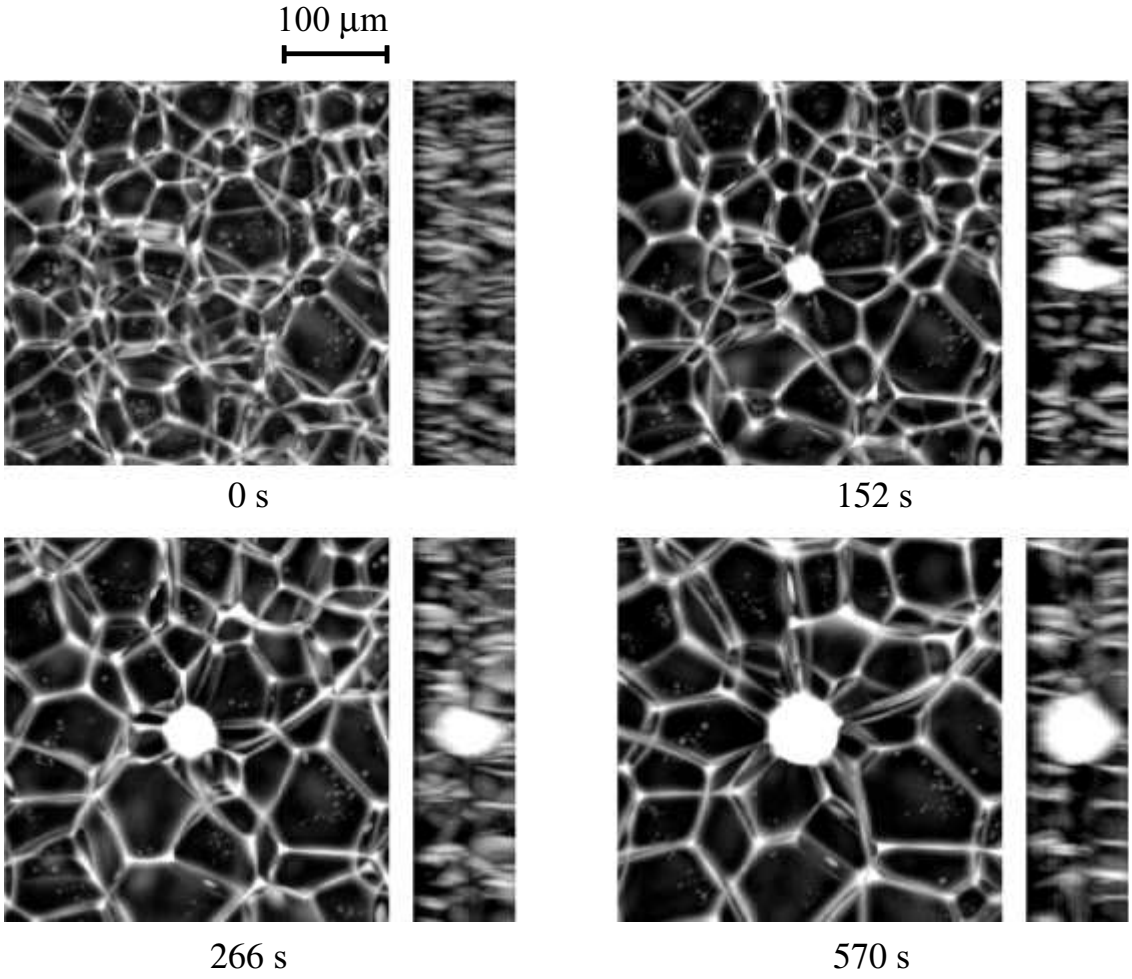

Figure 4.20: Two-photon laser scanning microscope image of 3-D grain structure around a heating spot generated by focusing the laser beam. The front view and the corresponding side view are shown.

the temperature dependence of the surface tension is negligible in the drift of grain boundaries in a temperature gradient. In 3-D grain growth, analyzing the data is the most critical part. Since only the edges of grain boundaries appear in the images of grain structures obtained by confocal laser scanning microscopy or two-photon microscopy, we need algorithms to reconstruct grains from the edges. Two candidates are Mousse software (Noesis Inc.), which was used by Monnereau and Vignes-Adler [40] to analyze 3-D foam structures, and the Surface Evolver developed by Ken Brakke [89]. Once the grains are reconstructed from the edges, the total number of grains, the number of faces of a grain, and the approximate (due to the lack of exact boundary shapes) volume of a grain can be obtained to study 3-D grain coarsening mechanism. Also, it will be interesting to apply feedback-controlled heatings to obtain desired grain boundary orientations in more systematic ways.

Chapter 5

Local Control of the Dendritic Microstructure Through Perturbation

5.1 Overview

This chapter focuses on control of microstructures within an individual grain. Our aim is to control cellular and dendritic microstructures which develop during directional solidification of binary alloys. Changes in pulling speed, temperature gradient, or alloy composition alter the microstructure. However, at a given pulling speed, temperature gradient, and alloy composition there are still often many microstructures possible. For example, the spacing between cells or dendrites λ (see Fig. 2.2) can only be controlled within a factor two or less and with great uncertainties at transitions between patterns such as the cell-dendrite transition, since they often exhibit strong hysteresis. Here we demonstrate that a local perturbation technique can provide accurate control of the microstructure. We show that this technique also provides valuable quantitative data on microstructure stability. Our study shows how the primary dendritic spacing λ can be selected in a controlled way at the start of solidification, and how it can be adjusted dynamically. The investigation focuses on the regime close to the cell to dendrite transition (see Fig. 2.2), where dendrites interact strongly with each other.

5.2 Experimental Detail

We used a 100 μm $\times$ 2 mm $\times$ 20 cm sample capillary filled with succinonitrile-coumarin152 (SCN-C152) (C=0.31wt%). The temperature gradient G is varied from 4.4 K/cm to 30.2 K/cm, and the pulling speed is varied from 0.9 μm/s to 31.0 μm/s.

We use UV light spots (100W mercury lamp) with controlled masks that generate UV light patterns or laser spots from a holographic laser tweezer to locally heat the sample. The sizes of the heated region depends on the magnification of the microscope objective, through which both UV and laser light is guided to the sample. Laser spot sizes are of the order of 10 μm and UV spot sizes are 65-350 μm with 4x magnification objectives.

We emphasize that we use thermal perturbations to control an interface whose shape is otherwise determined from solute diffusion. In order to allow the solute field to adjust to the altered interface shape, it is hence necessary to apply the perturbations for some time comparable to the solute diffusion time between two laser spots, i.e. of order 1 min for 200 μm separated spots (diffusion time $t = L^2/D$, where L is a length scale and D is the diffusion coefficient). This approach should generally work if the perturbation is applied long enough to allow adjustment of the solute field.

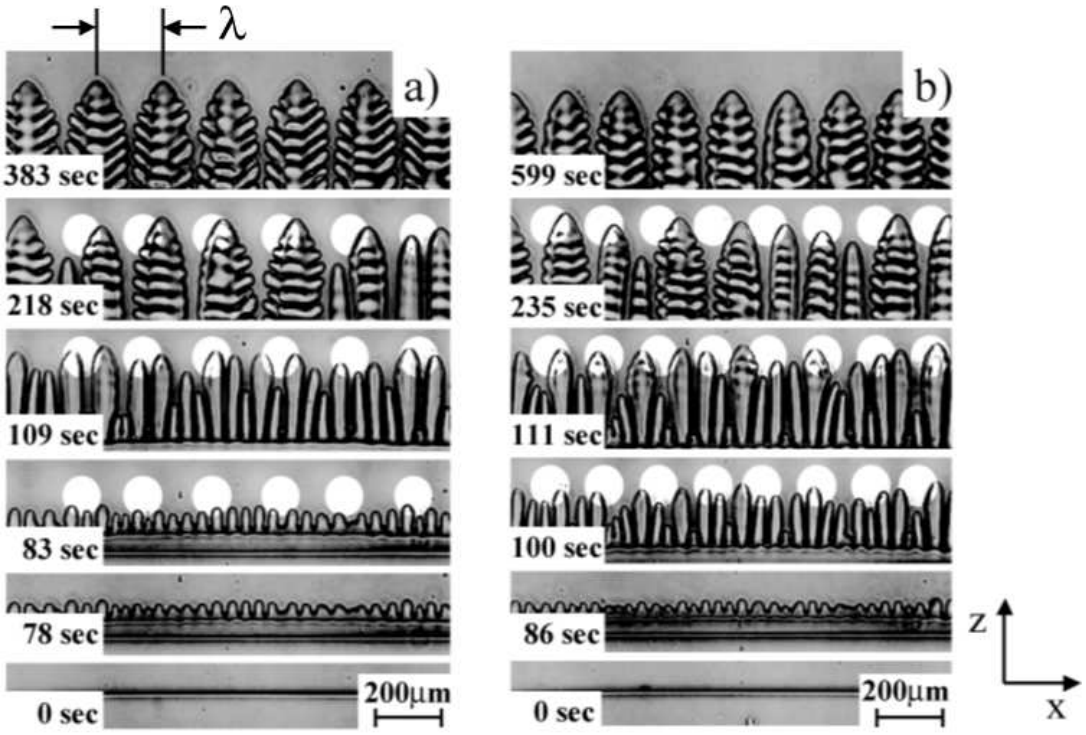

Figure 5.1: Uniform dendritic arrays with controlled interdendritic spacing λ are obtained through spatially periodic UV perturbations (bright spots). UV spots: (a) spacing 235 μm, Gaussian width 70 μm, duration 247 s; (b) spacing 190 μm, Gaussian width 65 μm, duration 434 s.

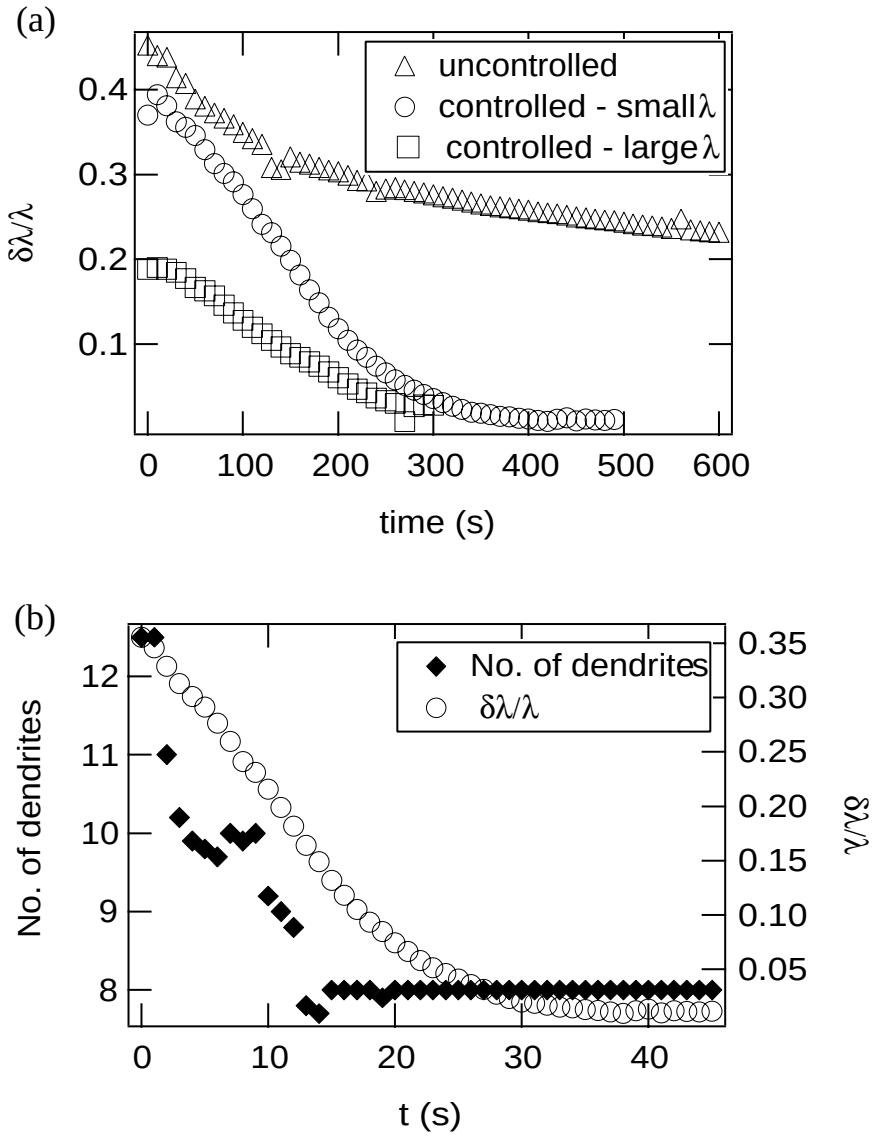

Figure 5.2: (a) The standard deviation of interdendritic spacings $\delta\lambda$ decreases to zero more rapidly under perturbations than in a reference experiment without perturbation. (same run as in Fig. 5.1; small and large λ correspond to (a) and (b) respectively) (b) The number of dendrites reaches a steady state at an early stage while $\delta\lambda$ shows continuous adjustment toward uniform λ before and after that. ($G = 7.5$ K/cm, $V = 8.8$ μm/s)

5.3 Results and Discussion

Planar to pattern transitions: The best time to control λ of cellular or dendritic arrays accurately is during the initial instability, when crystal growth starts. Here, we selectively heat regions in the liquid ahead of the solid-liquid interface by applying a row of uniformly spaced UV spots while the interface undergoes a planar to dendritic transition (Fig. 5.1). The UV light spots have Gaussian intensity profile with width of about a quarter of the distance between the spots, which effectively form a sinusoidal perturbation. We have not yet investigated the dependence on spot size systematically, but we find that for spot sizes much smaller than the spacing between spots (e.g. using laser spots), the resulting interdendritic spacing becomes less uniform. Simulations and theoretical analyses have indicated that for optimal control of the shape of the planar front perturbations should be applied a distance of the order of the diffusion length ahead of the front [96]. Here, we find that positioning the UV perturbations approximately one diffusion length (45 μm at $V = 10$ μm/s) ahead of the interface works best for triggering a controlled instability of a planar interface. The position of UV spots is manually adjusted in the z-direction, but fixed in the x-direction (see axes in Fig. 5.1). Although the UV spots heat the sample by less than ~ 0.2 K ($<$0.1% of the melting temperature and $<$1.2% of the latent heat/specific heat ratio of SCN) the dendrites align between UV spots and form a regular array. When the perturbation is removed, the dendritic array remains uniform and stable. Different λ can be selected by varying the spacing of UV spots. Through such perturbations any λ in the stable regime of the phase

diagram can be accurately selected.

With time an initially broad distribution of λ of the order of the wavelength of the planar instability changes into a sharp distribution peaked at the spacing imposed by the UV spot array. The standard deviation of interdendritic spacings $\delta\lambda$ (Fig. 5.2a) for the controlled arrays approaches nearly zero while $\delta\lambda$ for the non-controlled array decreases more slowly and stays far from zero. In general, the appropriate number of dendrites, i.e. the average spacing $\langle\lambda\rangle$, is established at an early stage but the variations in spacing $\delta\lambda$ are initially large and gradually reach a steady state as the system adjusts λ continuously (Fig. 5.2b). This control of λ is more powerful in dendritic arrays at low temperature gradients, where the range of stable λ is broad due to the strong interaction between sidebranches [22].

Pattern to pattern transitions: Transitions from one stable pattern to another are also possible. Fig. 5.3a shows an array of cells close to the cell to dendrite transition. This pattern is stable; small perturbations like the ones applied to a planar front are no longer sufficient to control the microstructure. Instead, large perturbations are needed to alter the microstructure as shown in Fig. 5.3. Under strong spatially periodic perturbation of every other cell a transition to a stable dendritic array is observed (Fig. 5.3c). This corresponds to the transition I in Fig. 2.2.

The necessary perturbation strength can be quantified from the response to small perturbations [59]. Fig. 5.4 shows a plot of the modulation amplitude ξ, i.e. the difference in tip position between perturbed and unperturbed cells (see Fig. 5.3a), after perturbations of various strengths are applied to every other tip.

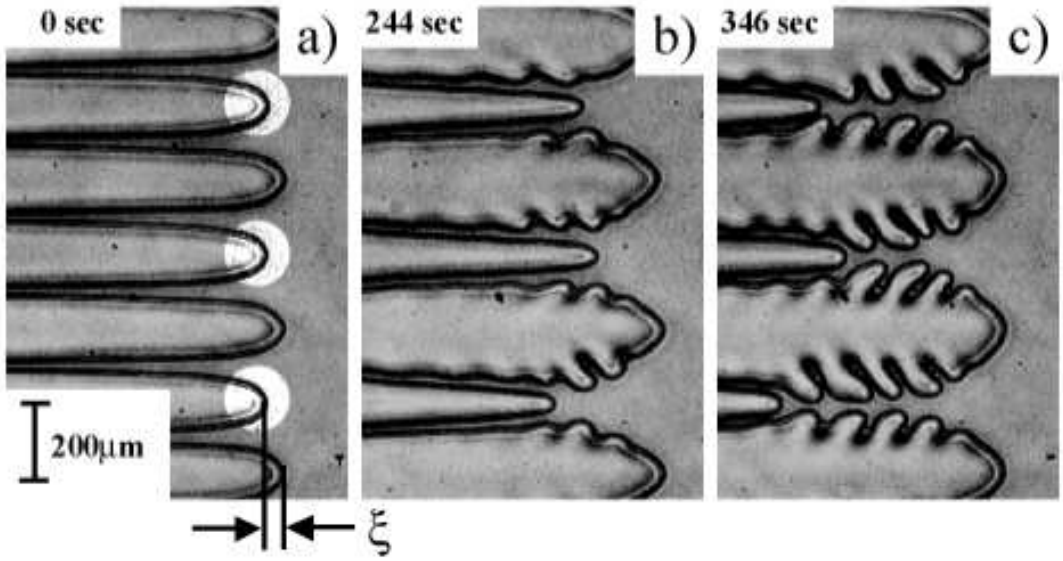

Figure 5.3: Guiding the crystal growth pattern through perturbations: A stable cellular interface pattern (a) is perturbed through localized perturbation of every other tip (UV spots: spacing 386 μm, Gaussian width 96 μm, duration 40 s). This triggers a transition (b) to another stable microstructure, a dendritic array (c).

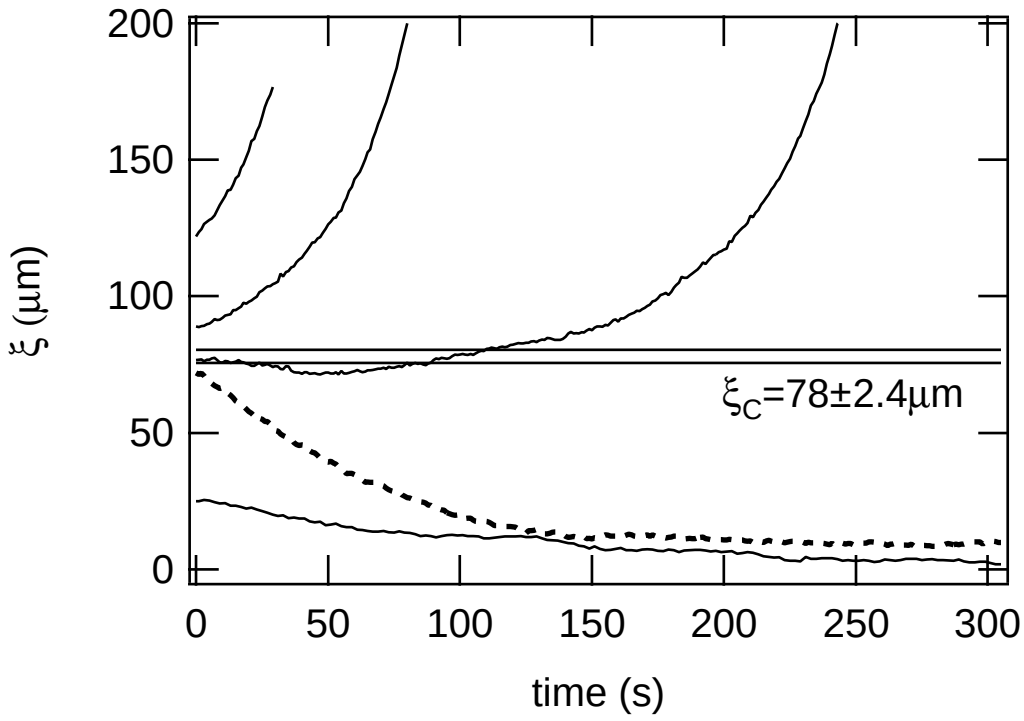

Figure 5.4: Modulation amplitude ξ vs time after perturbations with different strength. The band indicates the critical amplitude with uncertainty. The bottom two lines show weak perturbation, which lead to a decaying ξ. The top three lines show the growth of ξ (which leads to period doubling) after strong perturbations. ($G = 4.4$ K/cm, $V = 5.9$ μm/s)

A third order amplitude equation suffices to characterize the time evolution of ξ during this cell-dendrite transition:

$$\frac{d\xi(t)}{dt} = a_0\xi(t) + a_1 \left|\xi(t)\right|^2 \xi(t). \tag{5.1}$$

Here a_0 and a_1 are linear and third order growth coefficients respectively. Both a_0 and a_1 depend on the wavelength of the perturbation (i.e. the spacing between UV spots) and the spacing between cells or dendrites, but do not depend on the strength of the perturbation.

Small ξ decay exponentially. When ξ starts above a critical value, ξ grows with time, leading to the period doubling transition shown in Fig. 5.3 (note that the third order amplitude equation can only describe that initial amplitudes above a critical threshold grow, and does not capture the transition to a new stable pattern). The critical initial amplitude from Eq. (5.1) is given by $\xi_C = \sqrt{-a_0/a_1}$. Nonlinear fitting [59] of the decaying ξ for the dashed line shown in Fig. 5.4 yields a value of $\xi_C = 78 \pm 2.4\mu$m (shown as a band), in good agreement with the amplitude at which perturbations grow.

Other transitions: It is also possible to trigger a transition from a stable dendritic array to a period doubled dendritic array as indicated by the arrow II in Fig. 2.2. Experimentally transitions to other than period doubled patterns require stronger perturbations, which is not surprising since period doubling has been found to be the most unstable mode of the system [58].

In addition, a period halving transition from a dendritic to a cellular array can

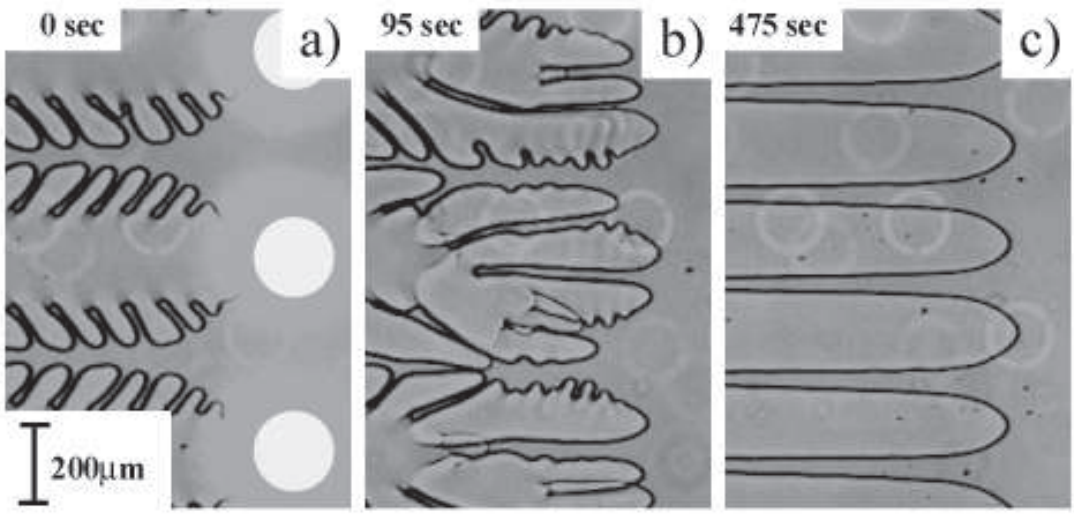

Figure 5.5: A period halving transition from a dendritic to a cellular array is triggered through very strong UV perturbation on every tip. UV spots: spacing 386 μm, Gaussian width 96 μm, duration 76 s.

be triggered through very strong UV perturbation on every tip but this transition is less accurately controllable (Fig. 5.5).

We could not trigger a cell to cell transition in several experiments in a parameter range, which corresponds to the transition III in Fig. 2.2, where one might most likely expect such a period doubling instability. This observation, and the visual indication e.g. in Fig. 5.3b that sidebranches prevent the perturbed cells from recovering, point to the important role of sidebranches for array stability and selection. We will present other experimental results in support of this assumption in detail in Chapter 6.

Transient structures: Perturbations can transiently generate microstructures with unsustainably large or small λ (for example, the transition IV in Fig. 2.2).

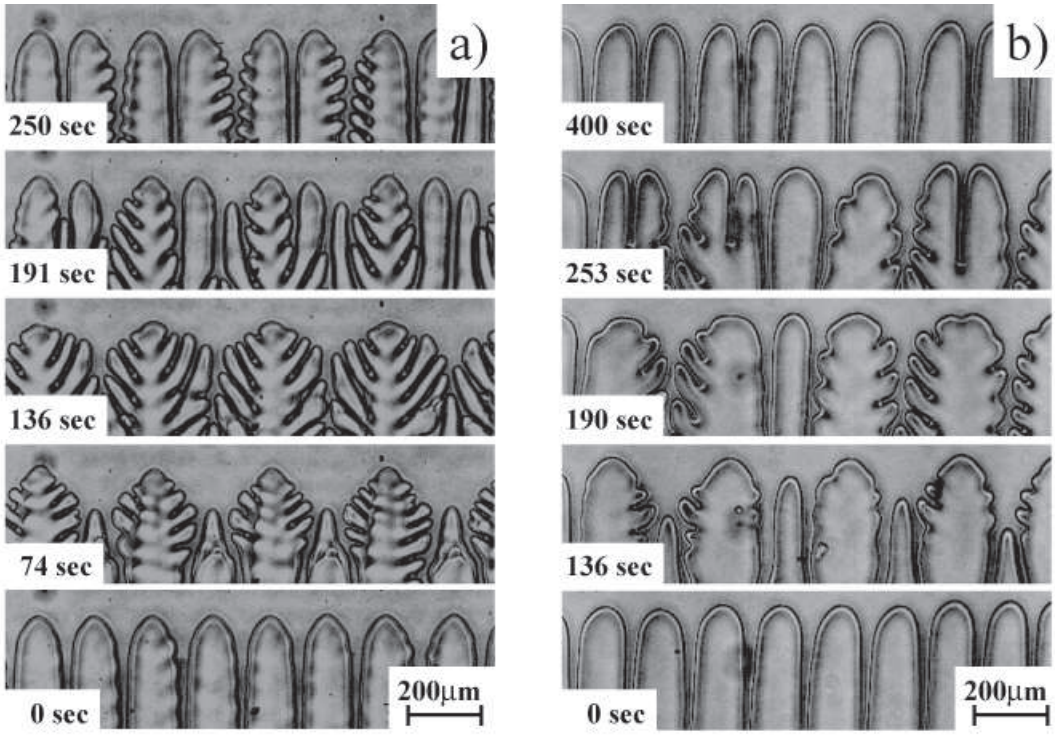

Figure 5.6: Arrays with λ larger than the stable range can be generated transiently through perturbations (second image from below) but the unstable array returns to smaller λ by growing sidebranches (a) or tip splitting (b).

This allows us to study what instability modes limit the range of stable λ. In Fig. 5.6 dendritic and cellular arrays are forced to have λ larger than the upper limit of stable spacings λ_{Max} under spatially periodic perturbation of every other dendrite or cell.

For dendrites λ is limited above λ_{Max} by sidebranches that lead to additional dendrites (Fig. 5.6a). For cells, λ is limited by a tip splitting instability (Fig. 5.6b). For both cells and dendrites, a period doubling instability provides a minimum stable λ_{Min}. Through repeated perturbations on cellular or dendritic arrays of different interdendritic spacing, the perturbation technique can indicate the range of stable λ and the mode of instability (sidebranch growing or tip splitting) that limits stable λ.

The generation of transient structures also allow us to investigate the mode of instability that is not normally observed. Fig. 5.7a is a magnified image of a transient dendrite in Fig. 5.6a. The tip position x and the tip radius of this dendrite oscillate until sidebranch overgrowth occurs as shown in Fig. 5.7c. This reveals the existence of a sideway tip oscillation instability which precedes the sidebranch growing instability. The same instability is also observed in simulations. Fig. 5.7b (simulation by A. Karma, Northeastern Univ.) shows a dendrite in a stable limit cycle state that exists over a finite range of spacing in the absence of noise. The tip exhibits symmetric oscillation. When noise is introduced to this state, the tip oscillates asymmetrically (sideway) and the limit cycle decays through growing sidebranches, exactly same as our observation.

Non-periodic structures: Control of non-periodic microstructures requires

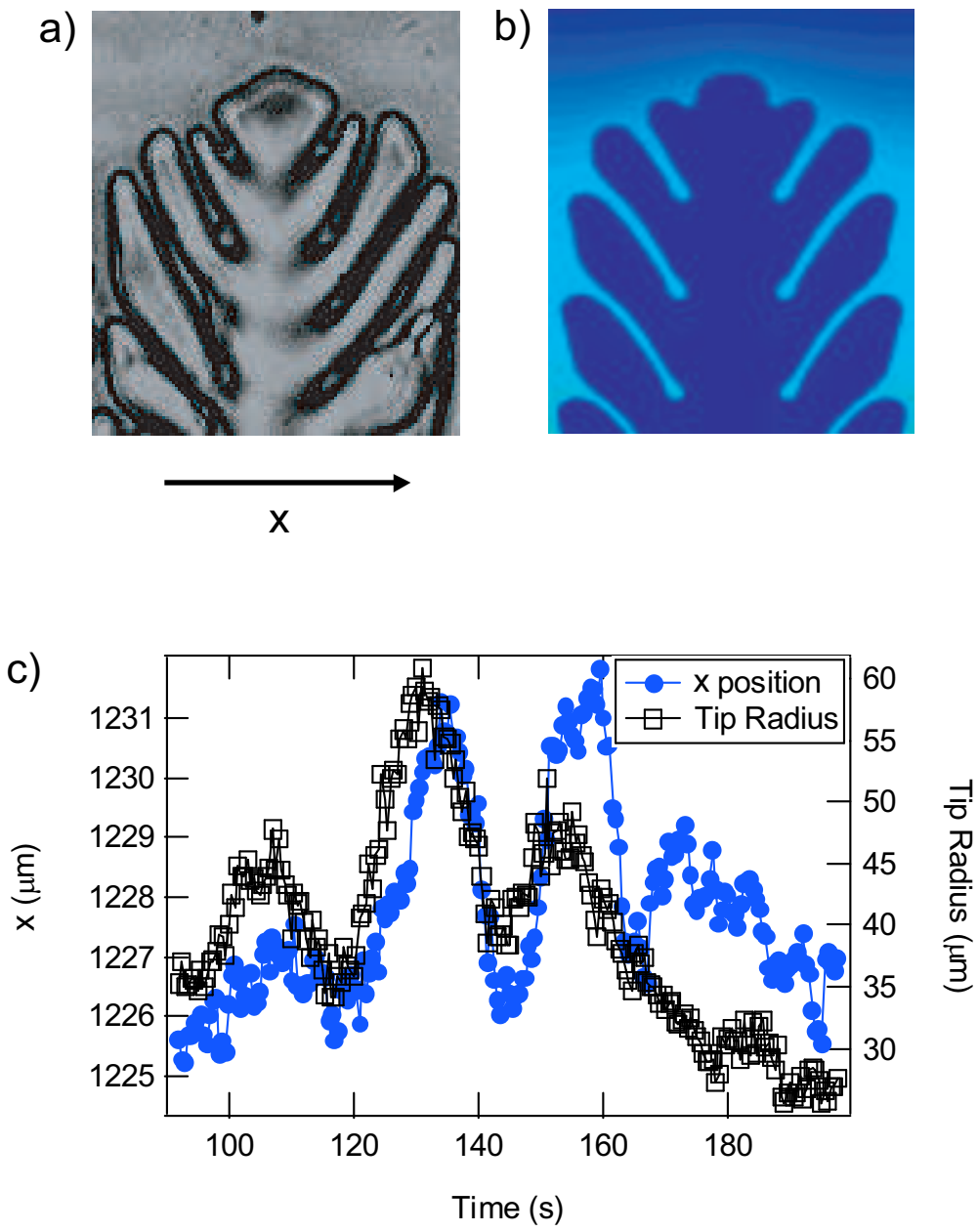

Figure 5.7: (a) A magnified image of a transient dendrite in Fig. 5.6a. (b) A dendrite in a stable limit cycle state (simulation by A. Karma). (c) A plot of the tip position x and the tip radius vs. time for the dendrite in (a).

more complex spatio-temporal perturbations as e.g. generated by our holographic laser tweezer system (Chapter 3). Fig. 5.8 shows the laser spots applied to a cellular front. Through appropriate positioning and motion of the perturbation points as indicated by the arrows, we continuously increase the local interdendritic spacing λ around a dendrite or a cell in an array. When the local λ reaches a threshold value, the array reduces λ by either growing sidebranches (again preceded by sideway tip oscillations) or tip splitting. The critical λ where these instabilities occur is in good agreement with λ_{Max} obtained by the method of step-increase of the growth speed [22]. This indicates that in our parameter range of strongly interacting dendrites, array stability is mostly determined by nearest neighbor interactions.

5.4 Conclusion

In summary, we have studied experimentally how to use thermal perturbations to accurately control solute diffusion generated cellular and dendritic arrays in directional solidification of a model binary alloy SCN-C152. Spatially periodic thermal perturbations during the initial instability create controlled arrays of cells or dendrites with any desired interdendritic spacing in the stable range. Large perturbations can trigger a transition from one stable state to another stable state. Finally, perturbations allow us to temporarily trigger λ that is outside of the stable range. This has allowed us to find tip splitting and sidebranching as the modes of instability at λ greater than λ_{Max}, and period doubling instabilities at λ smaller than λ_{Min}. Holographic techniques are used to generate controlled, non-periodic structures.

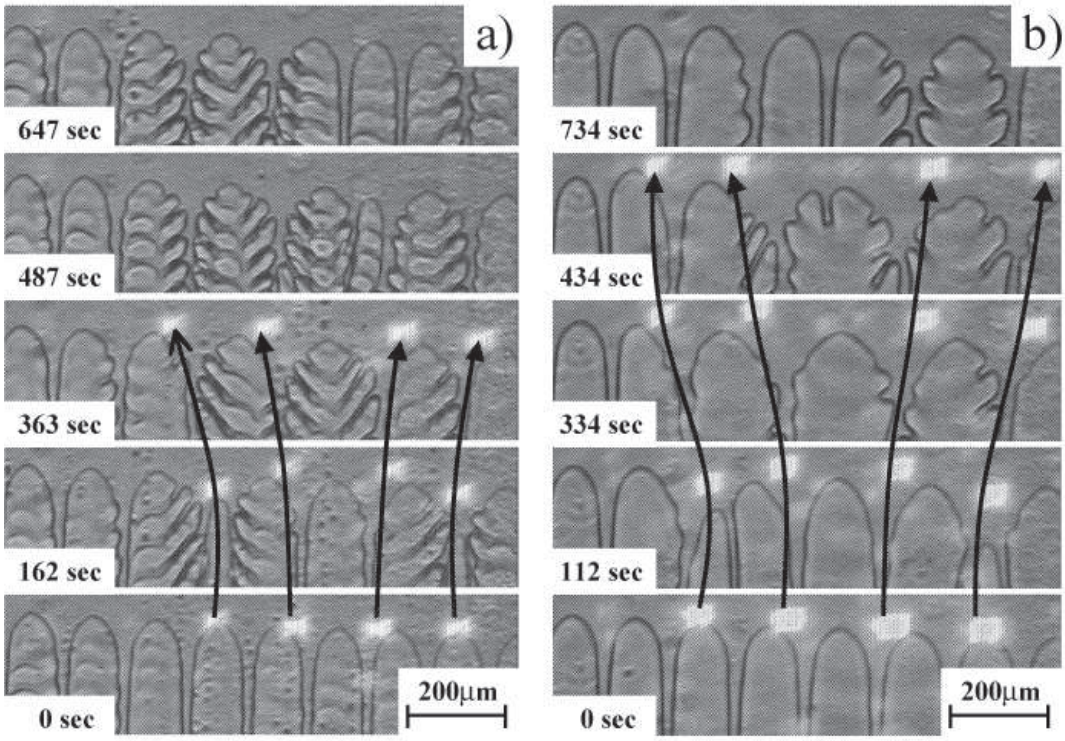

Figure 5.8: Control of non-periodic structures: The local λ is continuously increased by independently movable laser spots (40 μm in diameter) until the system adjusts λ through instabilities - (a) sidebranch growing and (b) tip splitting. The arrows indicate the controlled motion of laser spots.

Recent experimental results point to the possibility of controlling real metallic alloys using similar techniques. Global perturbations through pressure pulses might be sufficient for control of periodic microstructures by exploiting temporal resonances [97]. X-ray imaging of dendritic growth has provided in-situ imaging of pattern formation [98]. We thus anticipate that the control and analysis techniques shown in this paper could be applied to metallic alloys using interference patterns of X-rays of a wavelength that gets partially absorbed, or using other means of perturbations that can penetrate the material such as ultrasound or microwave radiation.

Chapter 6

Studies on Cellular/Dendritic Arrays with Different Crystal Orientations

6.1 Overview

The characteristic shape of dendrites is due to the anisotropy in surface tension. Although the role of crystalline anisotropy in interface dynamics has been studied by some experimental groups [42, 43], the studies were mainly focused on the seaweed and ordinary dendritic structures. In this study we investigate the role of surface tension anisotropy on stability of arrays of cells and dendrites during directional solidification (DS) of binary alloys. We use three crystals of different growth orientations with respect to the surface tension anisotropy to study the relative importance of surface tension in the growth direction and in the direction normal to the growth direction for microstructure selection and stability.

As discussed in Chapter 2, the surface tension is represented in 3-D as Eq. (2.3). Because of the presence of anisotropy there exists a preferred orientation for crystal growth, which is the direction of maximum surface tension. In our thin sample directional solidification because the crystal is constrained to grow in the sample plane, the orientation of the sample plane with respect to the 3-D surface tension anisotropy becomes important. In addition, the growth direction with respect to

the anisotropy in the sample plane, which is equivalent to a slice through the 3-D anisotropy, determines the overall growth patterns.

6.2 Experimental Detail

We used 100μm thin, 2mm wide samples filled with succinonitrile-coumarin152 (SCN-C152) ($C = 0.51$wt% and $C = 0.31$wt%). The temperature gradient G used are 4.4 K/cm and 12.7 K/cm, and the pulling speed is varied from 0.9 μm/s to 31.0 μm/s.

Creating different crystal orientations is at present very difficult and limits more detailed studies. One promising approach for more detailed studies would be a rotating stage that permits directional solidification in any directions in the sample plane [43]. In our experiment the sample is rapidly cooled to develop multiple nuclei. Crystal orientations are selected from the random orientations of spontaneously nucleated crystals. Each nucleus is grown until discernible dendrites appear. Once a suitably oriented nucleus is found, all neighboring nuclei are selectively melted back using laser and UV light spots, giving the desired nucleus space to overgrow all neighbors and completely fill the sample cell. In order to be able to make follow up measurements with each orientation, we used separate samples for the different orientations, but all the samples were made from the same mixture of SCN and C152 during a single sample filling procedure. Note that we produce three samples in a batch as shown in Appendix B. We verified some results on one of the samples, for which we selected more than one orientation.

The physical quantities we measured with the three crystals are the average spacing $\langle\lambda\rangle$, the average tip radius $\langle R\rangle$, the average maximum spacing $\langle\lambda_{max}\rangle$, and the average minimum spacing $\langle\lambda_{min}\rangle$ of cellular/dendritic arrays. For the measurement of $\langle\lambda\rangle$ and $\langle R\rangle$ crystal growth is started from a planar solid-liquid interface at constant speed V. When the cellular/dendritic array reaches the steady state, the spacings and the tip radii are measured and averaged to give $\langle\lambda\rangle$ and $\langle R\rangle$ for that V. $\langle\lambda_{max}\rangle$ is obtained by the method of step-increase of the growth speed [22]. A stable cellular/dendritic array is first formed at a low pulling speed and then the speed is increased in steps and maintained for enough time at each speed step for the array to stabilize. The spacings of the stable array at each speed are measured and averaged. Similarly, the average minimum spacing $\langle\lambda_{min}\rangle$ is obtained by step-decreasing the growth speed of a dendritic array which is first formed at a high pulling speed. Therefore, an approximate range of stable spacings is provided by $\langle\lambda_{max}\rangle$ and $\langle\lambda_{min}\rangle$.

6.3 Results and Discussion

We adopt the notation used by Akamatsu et al. [42] to denote the crystal orientation of the cells/dendrites. A lattice plane $\{hkl\}$ is parallel to the plane of the sample and a lattice axis $\langle uvw\rangle$ is parallel to the growth direction (Fig. 6.1). The cell/dendrite will be said to be $\{hkl\}\langle uvw\rangle$-oriented.

The typical shapes of the dendrites of three crystal orientations are shown in Fig. 6.2: (a) $\{001\}\langle 100\rangle$-oriented dendrites are the ordinary dendrites that have

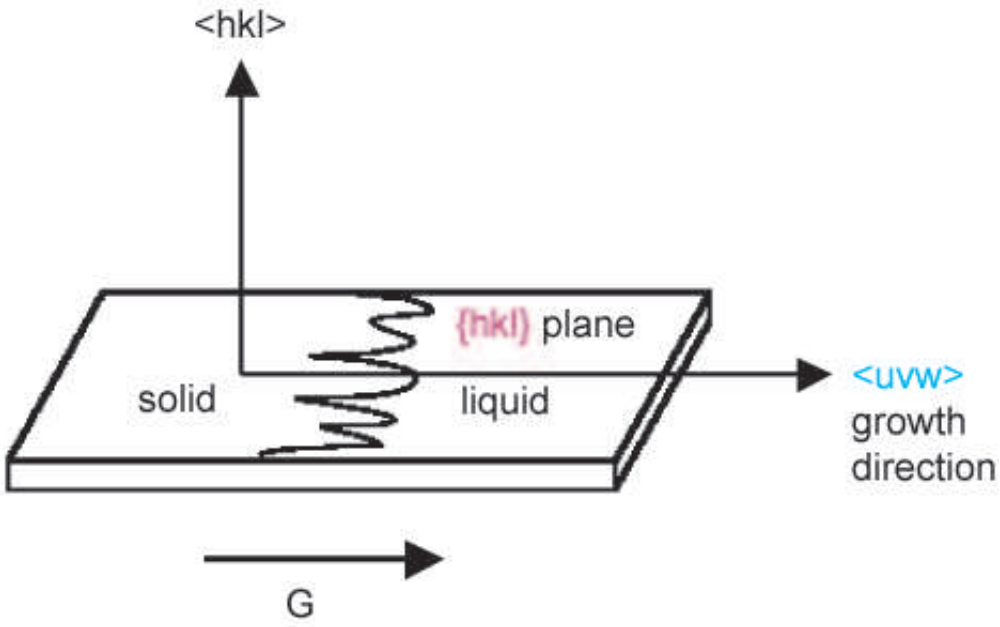

Figure 6.1: $\{hkl\}\langle uvw\rangle$-oriented crystal.

been observed and studied. Two sidebranches grow toward the sidebranches of neighboring dendrites and the other two grow directly into the wall with 90° angle. (b) $\{011\}\langle 100\rangle$-oriented dendrites have sidebranches growing into the wall with 45° angle. (c) $\{\bar{1}01\}\langle 101\rangle$-oriented dendrites have sidebranches growing toward other sidebranches as $\{001\}\langle 100\rangle$-oriented dendrites, but have no sidebranches growing into the wall.

Moreover, each crystal has different (tip) growth direction with respect to the orientation of surface tension anisotropy. Fig. 6.3a, Fig. 6.4a, and Fig. 6.5a shows the growth direction and the surface tension anisotropy in three dimensions for $\{001\}\langle 100\rangle$-, $\{011\}\langle 100\rangle$-, and $\{\bar{1}01\}\langle 101\rangle$-oriented crystals respectively. The figures are exaggerated for clarity as the surface tension anisotropy of SCN is very small.

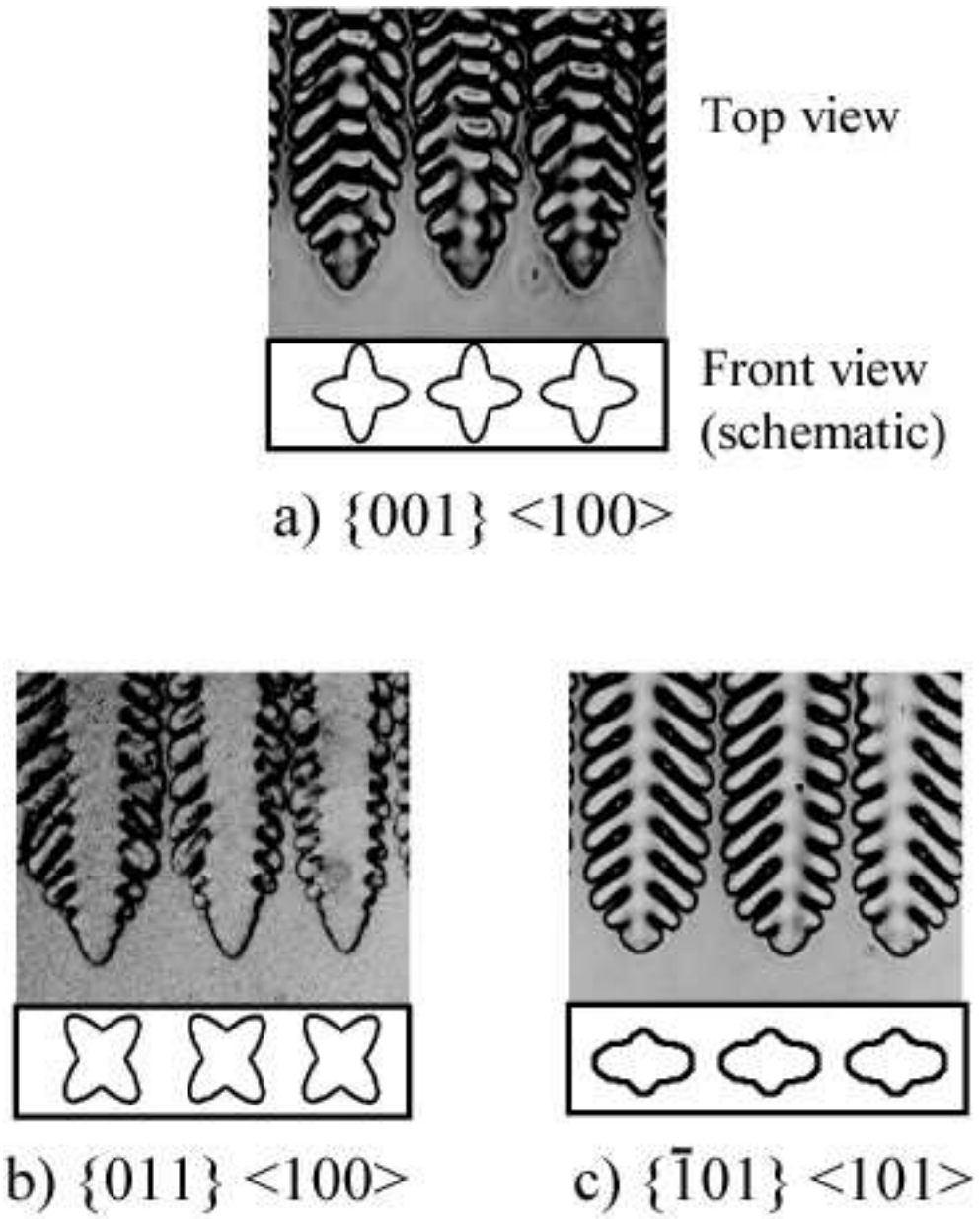

Figure 6.2: (a) $\{001\}\langle 100\rangle$dendrites have sidebranches growing toward each other and growing directly into the wall with 90 ° angle. (b) $\{011\}\langle 100\rangle$-oriented dendrites have sidebranches growing into the wall with 45 ° angle. (c) $\{\bar{1}01\}\langle 101\rangle$-oriented dendrites have sidebranches growing toward other sidebranches but have no sidebranches growing into the wall.

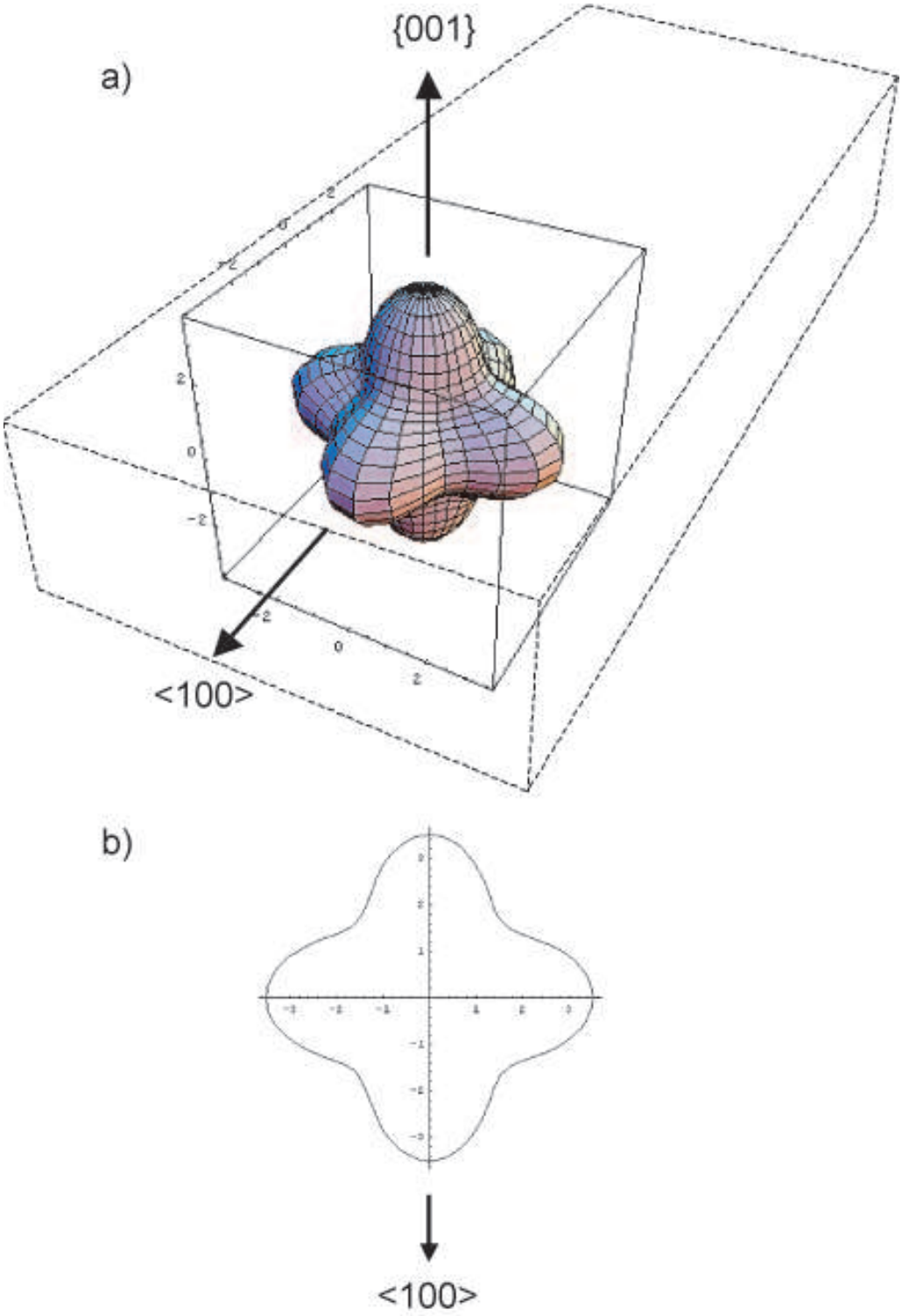

Figure 6.3: $\{001\}\,\langle 100\rangle$-oriented crystal have the strong tip and strong transverse surface tensions.

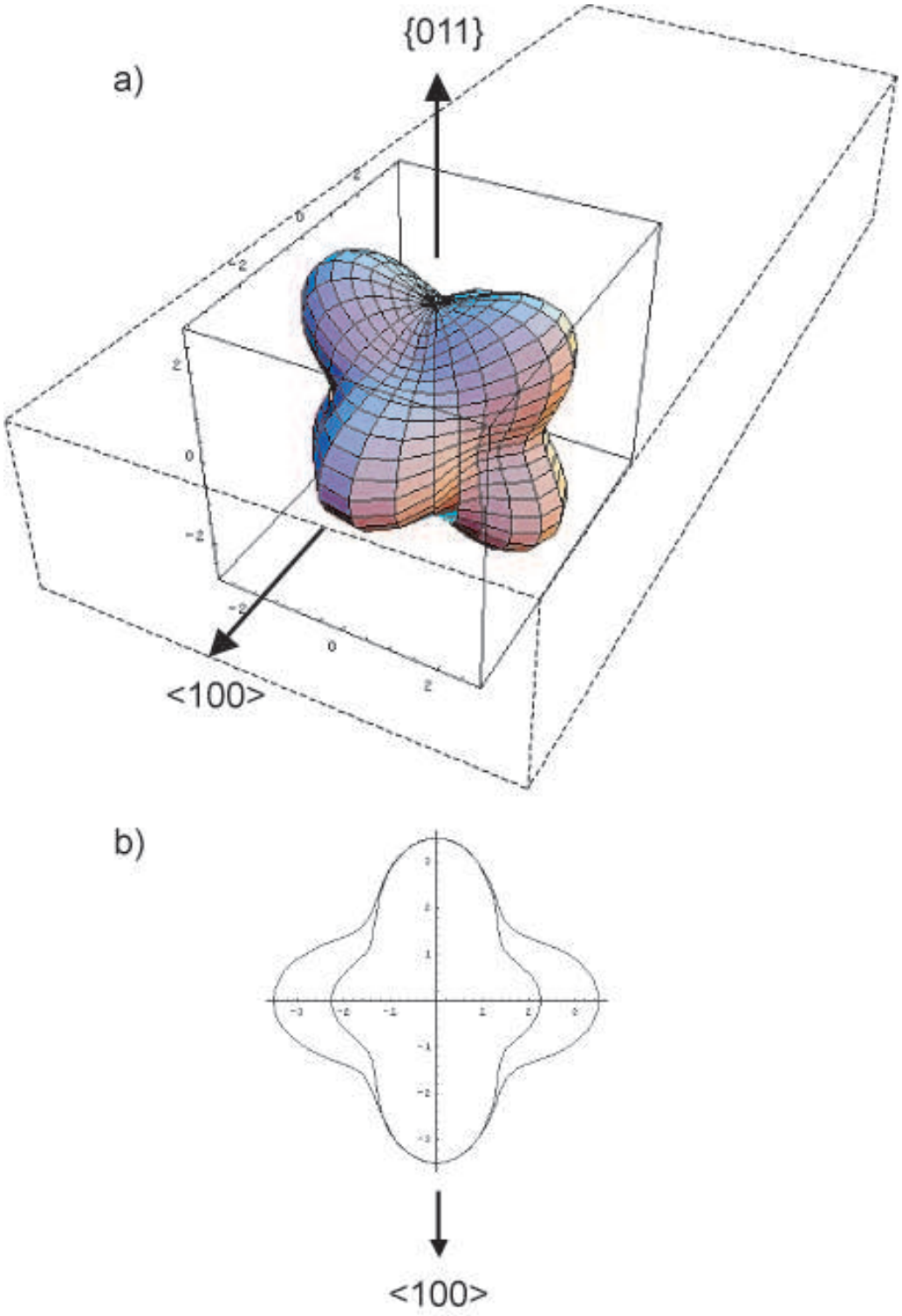

Figure 6.4: $\{011\}\,\langle 100\rangle$-oriented crystal have the strong tip and weak transverse surface tensions.

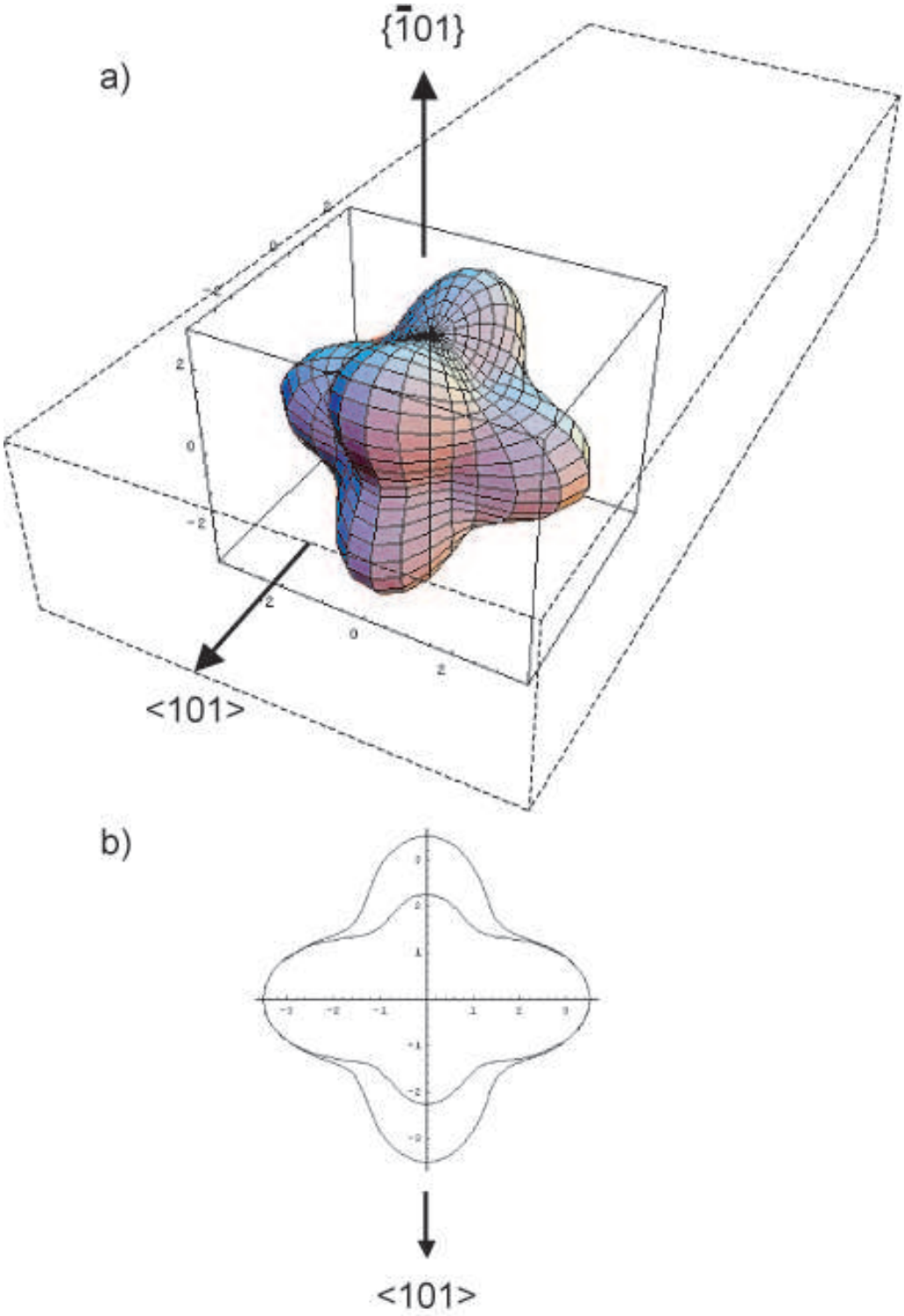

Figure 6.5: $\{011\}\langle 100\rangle$-oriented crystal have the weak tip and strong transverse surface tensions.

In thin sample directional solidification the two-dimensional in-plane surface tension anisotropy is important. As shown in Fig. 6.3b the in-plane surface tension anisotropy for $\{001\}\langle 100\rangle$-oriented crystal has a four-fold symmetry. During directional solidification the tip grows in one of the strong surface tension directions and the two in-plane sidebranches also grow in other directions of strong surface tension. The $\{011\}\langle 100\rangle$- and $\{\bar{1}01\}\langle 101\rangle$-oriented crystals have the in-plane surface tension anisotropy that does not have a four-fold symmetry as shown in Fig. 6.4b and Fig. 6.5b respectively. The $\{011\}\langle 100\rangle$-oriented crystal has tips growing in the direction of strong surface tension as the $\{001\}\langle 100\rangle$-oriented crystal, but it has weak surface tension on the sides of tips, where sidebranches would have appeared if it were the $\{001\}\langle 100\rangle$-oriented crystal. In contrast, the situation is exactly opposite for the $\{\bar{1}01\}\langle 101\rangle$-oriented crystal. The tips grow in the direction of weak surface tension while sidebranches grow in the strong surface tension direction. Note that Fig. 6.4b matches Fig. 6.5b if rotated $90\,^{\circ}$. Thus, the in-plane surface tension anisotropy for the two crystals are the same except for the orientation with respect to the growth direction. The consequence is that the $\{\bar{1}01\}\langle 101\rangle$-oriented crystal is forced to still grow along the sample plane with a tip in the direction of weak surface tension whereas the $\{011\}\langle 100\rangle$-oriented crystal does not have sidebranches growing along the sample plane in the direction of weak surface tension. In the following discussions, the surface tension on the sides of tips in two-dimensional growth, i.e. surface tension in the direction normal to the growth direction, will be called the transverse surface tension. The surface tension in the growth direction will be called the tip surface tension.

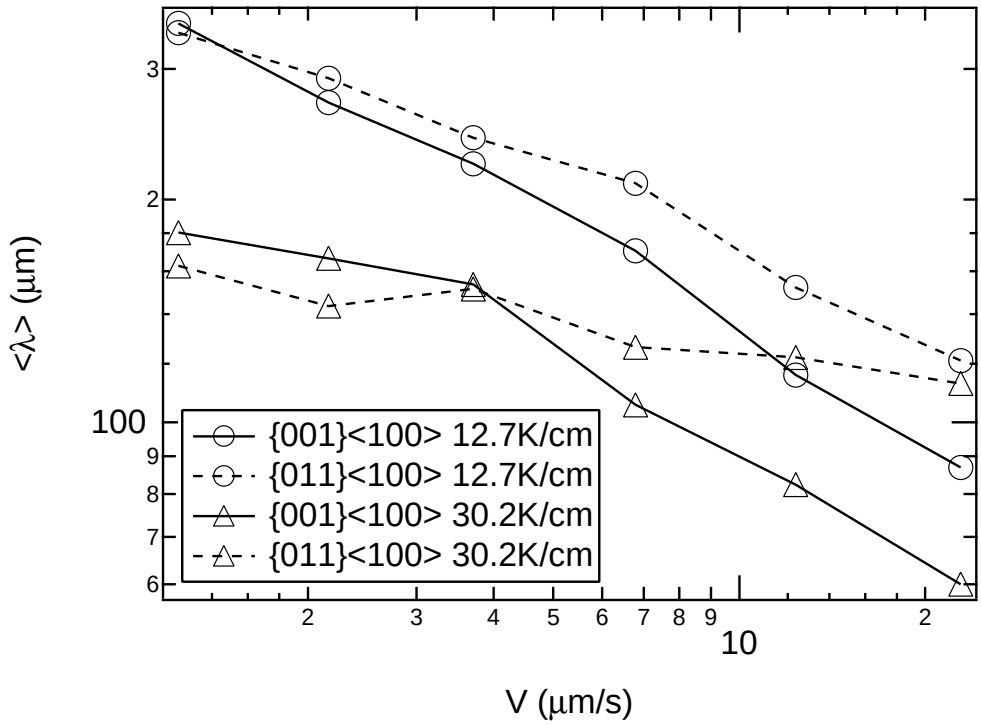

Figure 6.6: A plot of $\langle\lambda\rangle$ vs. V for $\{001\}\langle100\rangle$- and $\{011\}\langle100\rangle$-oriented arrays at two temperature gradients. $C = 0.51$ wt%.

Fig. 6.6 shows $\langle\lambda\rangle$ as a function of V for $\{001\}\langle100\rangle$- and $\{011\}\langle100\rangle$-oriented arrays ($C = 0.51$ wt%) at two temperature gradients. $\langle\lambda\rangle$ decreases with increasing V in all cases. At low temperature gradient ($G = 12.7$ K/cm) both $\{001\}\langle100\rangle$-oriented and $\{011\}\langle100\rangle$-oriented crystals form dendrites at the range of pulling speed we investigated (from 1.2 μm/s to 22.9 μm/s). At high temperature gradient ($G = 30.2$ K/cm) we observe a cell-dendrite transition at the pulling speed between 1.2 μm/s and 2.2 μm/s for the $\{011\}\langle100\rangle$-oriented crystal. The cell-dendrite transition for the $\{001\}\langle100\rangle$-oriented crystal occurs at slightly lower speed between 1.2 μm/s and 0.9 μm/s. This shift of the cell-dendrite transition at high temperature gradient to higher pulling speeds is consistent with other experiments [23]. When both crystals are dendritic, the $\{011\}\langle100\rangle$-oriented dendrites have larger $\langle\lambda\rangle$ than the $\{001\}\langle100\rangle$-oriented dendrites regardless of temperature gradients. However, as the $\{011\}\langle100\rangle$-oriented crystal becomes cellular, the $\{011\}\langle100\rangle$-oriented cells have smaller $\langle\lambda\rangle$ than the $\{001\}\langle100\rangle$-oriented dendrites. There are no prior measurements of how $\langle\lambda\rangle$ depends on growth direction with respect to anisotropy, and no theoretical predictions or simple arguments we are aware of, of what one may expect.

One possible reason for different $\langle\lambda\rangle$ between dendrites may be that the range of stable dendritic spacings (see Fig. 2.2) is different. Fig. 6.7 shows $\langle\lambda\rangle$, $\langle\lambda_{max}\rangle$, and $\langle\lambda_{min}\rangle$ as a function of V for $\{001\}\langle100\rangle$- and $\{011\}\langle100\rangle$-oriented arrays ($C = 0.51$ wt%) at the same temperature gradient, $G = 12.7$ K/cm. $\langle\lambda\rangle$ is near $\langle\lambda_{min}\rangle$ at high V and approaches $\langle\lambda_{max}\rangle$ as V decreases. $\langle\lambda_{min}\rangle$ of both crystals decreases with increasing V, whereas two crystals show completely different behavior in $\langle\lambda_{max}\rangle$. As

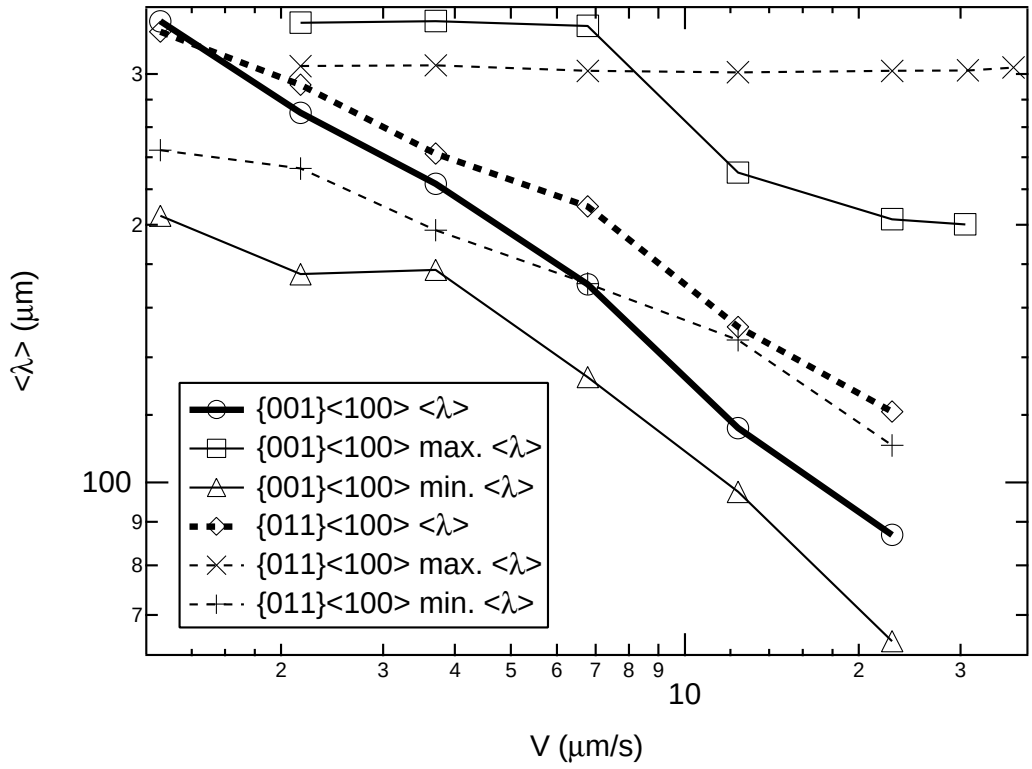

Figure 6.7: A plot of $\langle\lambda\rangle$, $\langle\lambda_{max}\rangle$, and $\langle\lambda_{min}\rangle$ vs.f V for $\{001\}\langle100\rangle$- and $\{011\}\langle100\rangle$-oriented arrays. $C = 0.51$ wt%, $G = 12.7$ K/cm.

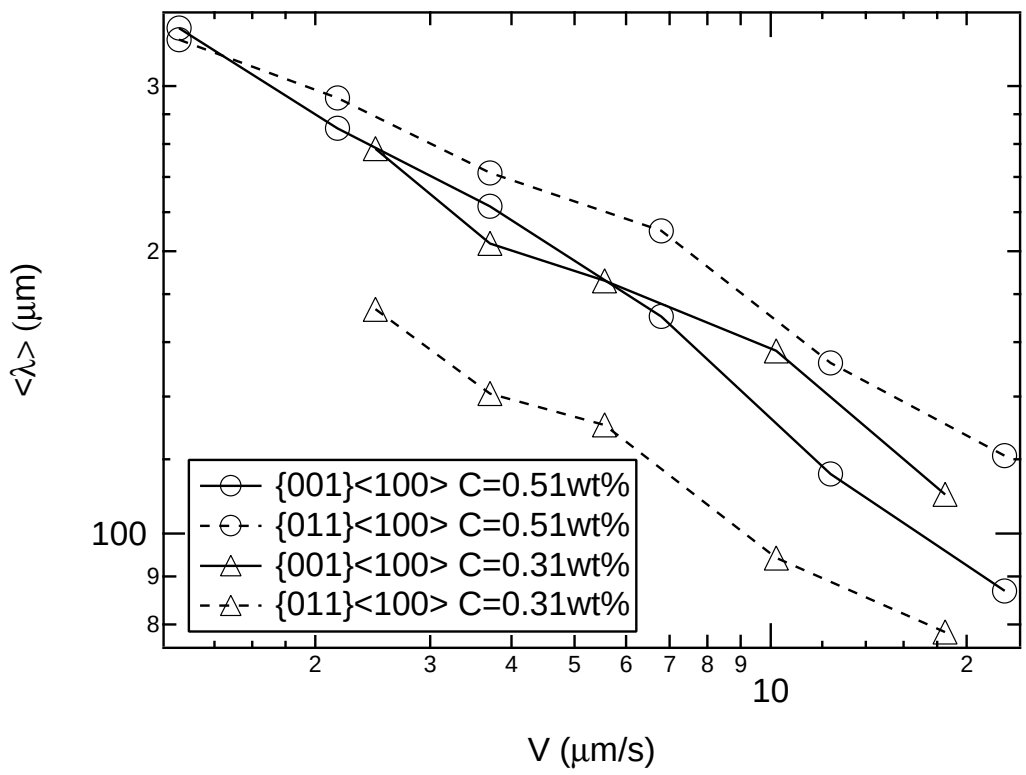

Figure 6.8: A plot of $\langle\lambda\rangle$ vs. V for $\{001\}\langle100\rangle$- and $\{011\}\langle100\rangle$-oriented arrays for two different concentrations. $G = 12.7$ K/cm.

V increases, the $\{001\}\langle100\rangle$-oriented dendritic array reduces its spacing through the growth of sidebranches, leading to the decrease in $\langle\lambda_{max}\rangle$. However, the maximum average spacing of the $\{011\}\langle100\rangle$-oriented dendritic array does not decrease with increasing V, which makes the range of stable spacing significantly large. Our observations indicate that in the $\{011\}\langle100\rangle$-oriented dendritic array the mechanism of reducing the spacings through the growth of sidebranches is not allowed because all the sidebranches are growing up or down against the top and bottom glass walls with a 45° angle. Also, we do not observe any tip splitting, which is the only other possible mechanism to reduce the spacings.

Fig. 6.8 shows a plot of $\langle\lambda\rangle$ vs. V for $\{001\}\langle100\rangle$- and $\{011\}\langle100\rangle$-oriented arrays for two different concentrations ($C = 0.31$ wt% and $C = 0.51$ wt%). In the whole explored range of V, a $\{011\}\langle100\rangle$-oriented crystal with low concentration forms cells while a $\{011\}\langle100\rangle$-oriented crystal with high concentration forms dendrites. $\{001\}\langle100\rangle$-oriented crystals form dendrites for both concentrations. To explain this, we need to consider two different effects on the cell-dendrite transition speed. First, the cell-dendrite transition speed increases as concentration decreases [60]. Second, low surface tension anisotropy makes the cell-dendrite transition speed higher [18]. In addition, since two crystals are different only in the transverse surface tension, our conjecture is that surface tension anisotropy affects the cell-dendrite transition speed via the transverse surface tension. When concentration is low, the transition speed of $\{011\}\langle100\rangle$-oriented crystal with low transverse surface tension is significantly increased, thus we observe only cells. The transition speed of $\{001\}\langle100\rangle$-oriented crystal with low concentration is not increased as much because of its high transverse surface tension. The low transverse surface tension makes it harder for the cells to develop sidebranches and to become dendrites even if they have the strong tip surface tension. In our experiments instabilities out of the sample plane are hindered by the presence of sidewalls.

Fig. 6.8 shows that $\{011\}\langle100\rangle$-oriented cells have smaller average spacing than $\{001\}\langle100\rangle$-oriented dendrites, whereas $\{011\}\langle100\rangle$-oriented dendrites have larger average spacing than $\{001\}\langle100\rangle$-oriented dendrites. Fig. 6.9 shows a plot of $\langle R\rangle$ vs. V for the samples of Fig. 6.8. $\langle\lambda\rangle$ and $\langle R\rangle$ have exactly opposite behavior. $\langle R\rangle$ of $\{011\}\langle100\rangle$-oriented cells is larger than $\langle R\rangle$ of $\{001\}\langle100\rangle$-oriented

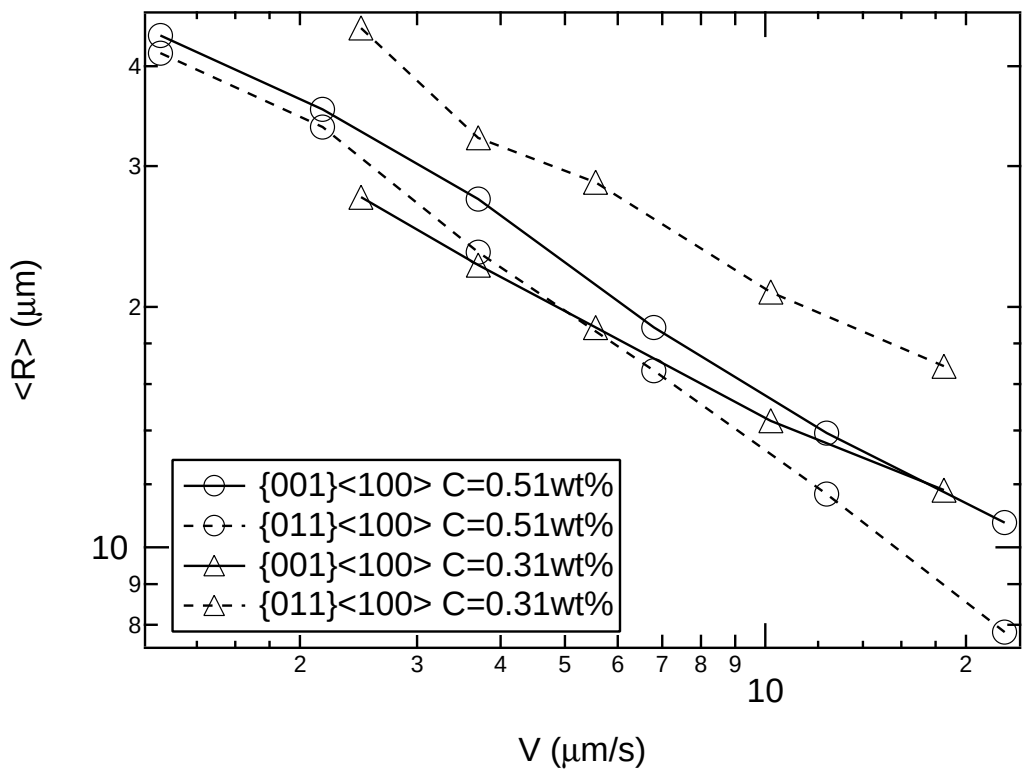

Figure 6.9: A plot of $\langle R \rangle$ vs. V for the samples of Fig. 6.8. $G = 12.7$ K/cm.

dendrites, while $\{011\}\langle 100\rangle$-oriented dendrites have smaller $\langle R \rangle$ than $\{001\}\langle 100\rangle$-oriented dendrites. When the spacing and the tip radius are multiplied together as shown in Fig. 6.10, interestingly the curves of two crystals with the same concentration collapse onto each other. More investigation is needed to explain this observation.

Fig. 6.11 shows a plot of $\langle \lambda \rangle$ vs. V for arrays of $\{001\}\langle 100\rangle$- and $\{\bar{1}01\}\langle 101\rangle$-oriented dendrites. They show almost identical behavior in the overlapped region. Two crystals have the same transverse surface tension, but the $\{\bar{1}01\}\langle 101\rangle$-oriented crystal has weak tip surface tension. This indicates that the transverse surface tension plays an important role in spacing selection and the tip surface tension has

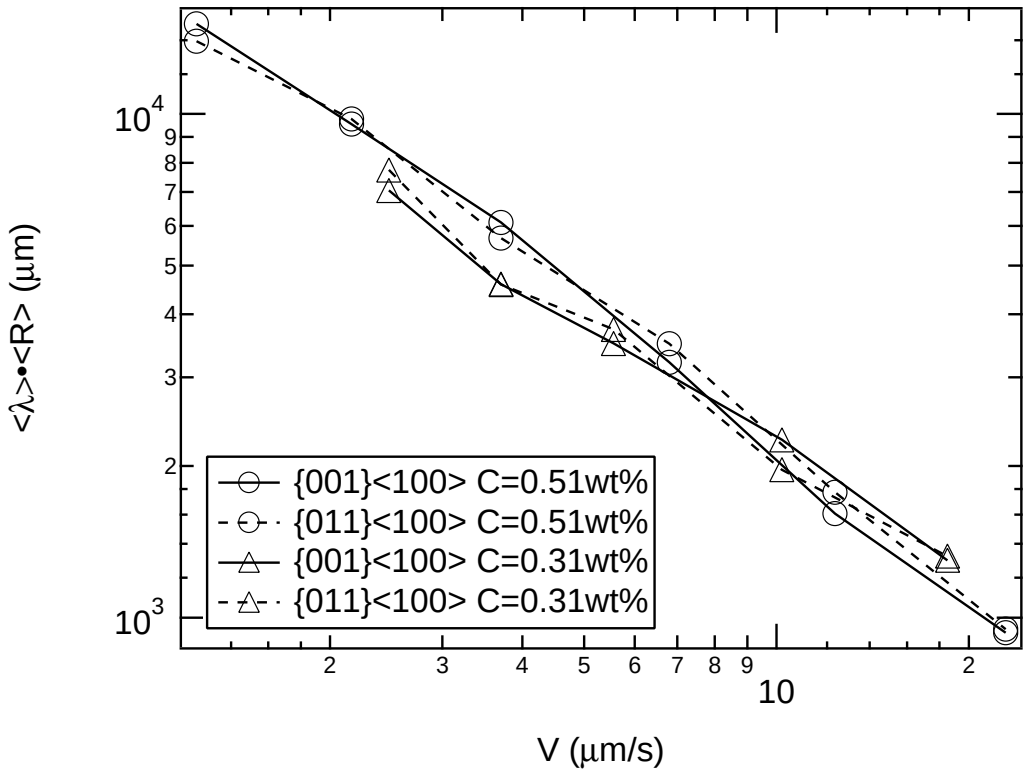

Figure 6.10: A plot of $\langle\lambda\rangle \cdot\langle R\rangle$ vs. V for the samples of Fig. 6.8. $G = 12.7$ K/cm.

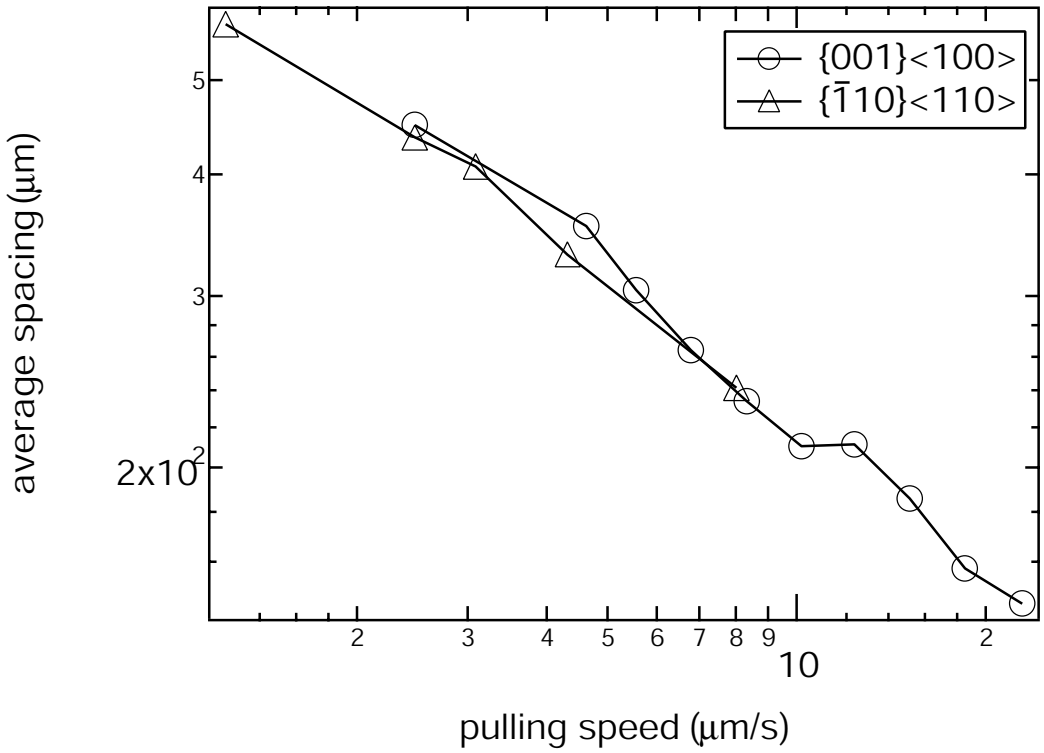

Figure 6.11: A plot of $\langle\lambda\rangle$ vs. V for arrays of $\{001\}\,\langle100\rangle$- and $\{\bar{1}01\}\,\langle101\rangle$-oriented dendrites. $C = 0.31$ wt%, $G = 4.4$ K/cm.

no effect.

$\{\bar{1}01\}\,\langle101\rangle$-oriented dendrites have very regular sidebranches on both sides of the tips, which are out-of-phase as shown in Fig. 6.12a (also see Fig. 6.2c). In addition, there is a sideway tip oscillation that couples the two out-of-phase sidebranchings (Fig. 6.12b). We suspect this is also because of the weak tip surface tension and the strong transverse surface tension. The sideway tip oscillation is very similar to the one that happens when $\{001\}\,\langle100\rangle$-oriented dendrites have unsustainable large spacings (see Chapter 4).

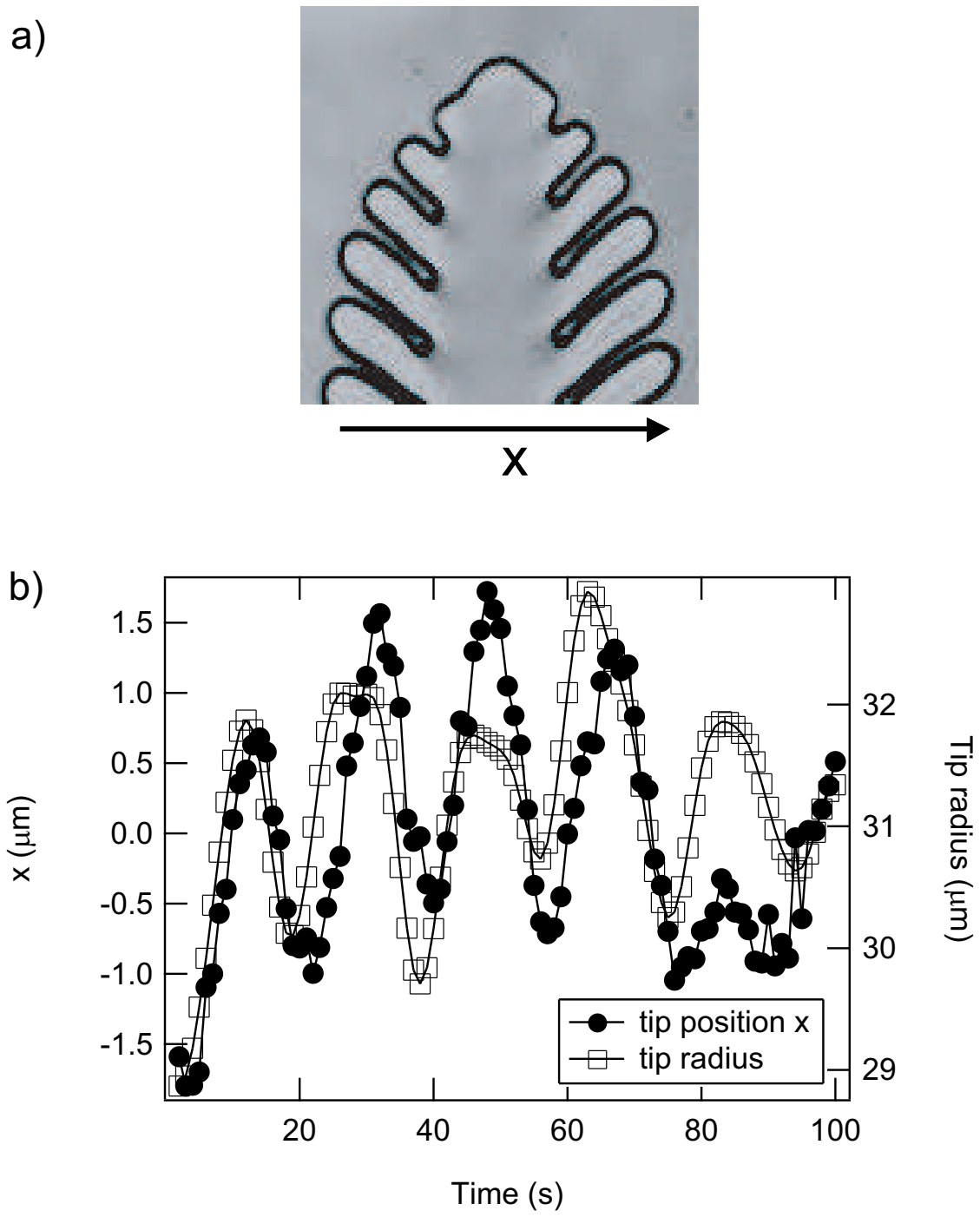

Figure 6.12: (a) A magnified image of a $\{\bar{1}01\}\langle 101\rangle$-oriented dendrite. (b) A plot of the tip position y and the tip radius vs. time for the dendrite in (a).

6.4 Conclusion

We investigated the role of surface tension anisotropy on the stability of cellular/dendritic arrays using three crystals of different growth orientations with respect to the surface tension anisotropy. The conventional four-fold symmetric surface tension is decomposed into two normal components, the tip surface tension, which is in the growth direction, and the transverse surface tension, which is in the normal direction to the growth direction. The crystal with low transverse surface tension and high tip surface tension has a larger dendritic spacing and a smaller tip radius than a crystal with high transverse and tip surface tension. On the other hand, the crystal with low tip surface tension and high transverse surface tension exhibits the same spacing as ordinary crystals but the tip is less stable and exhibits oscillations. From these observations, we deduce that the transverse surface tension affects the selection of the dendritic spacing while the tip radius is determined by both tip and transverse surface tension.

We need further investigations to fully understand the role of surface tension anisotropy on cellular/dendritic structures. For example, we have not compared $\langle\lambda\rangle$ for $\{001\}\langle100\rangle$- and $\{011\}\langle100\rangle$-oriented arrays when both arrays are cellular. Also, $\{\bar{1}01\}\langle101\rangle$-oriented cellular array needs to be included in the discussion and compared with other crystals. The range of stable spacings for $\{\bar{1}01\}\langle101\rangle$-oriented crystal should be compared with $\{001\}\langle100\rangle$-oriented crystal. The possible presence of 3-D effects on cellular/dendritic structures of three crystals can be investigated with thinner samples. In this study we have also encountered some

interesting questions such as why $\{011\}\langle 100\rangle$-oriented dendritic array has larger $\langle\lambda\rangle$ than $\{001\}\langle 100\rangle$-oriented dendritic array and, why $\langle\lambda\rangle$ times $\langle R\rangle$ is same for $\{001\}\langle 100\rangle$- and $\{011\}\langle 100\rangle$-oriented cellular/dendritic arrays. It will be also interesting to study the role of surface tension anisotropy on the stability of arrays by using perturbation methods described in Chapter 5.

Appendix A

Preliminary Studies on Eutectic Microstructure

(This work is done by collaboration with S. Akamatsu, S. Bottin-Rousseau, and G. Faivre, Groupe de Physique des Solides, Universités Denis-Diderot et Pierre-et-Marie-Curie, Paris, France

A.1 Overview

Prediction and control of the formation of lamellar eutectics is a challenging subject in applied metallurgy [3, 51] and in fundamental physics [99, 100]. Lamellar microstructures –a more or less regular alternation of lamellae of two different crystal phases– form during the solidification of nonfaceted binary eutectic alloys. This finely spaced microstructure greatly enhances the mechanical strength of the alloy. The morphology and the size distribution of the frozen-in two-phase structures are determined by dynamic phenomena on the growth front, namely, a competition between diffusion in the liquid and capillarity. This is a complex problem of **out-of-equilibrium, nonlinear pattern formation**, hence the microstructure cannot be predicted by any general minimization principle. Simulations are also difficult, since microstructure formation involves physical processes operating on a large range of spatial scales [101].

Nearly periodic lamellar microstructures can be obtained by directional so-

lidification of eutectic alloys, i.e., by pulling the crucible containing the alloy at a constant speed V in an imposed thermal gradient G. During steady state solidification, the crystal growth front presents a modulated shape on the scale of the interlamellar spacing λ, but is planar on larger scales (Fig. A.1). The problem, as it was formulated fifty years ago [102], was to know whether it is possible to predict the value of the spacing as a function of V, G, the concentration C_0 and the physical constants of the alloy. Decades of metallographic studies did not allow one to solve this "selection problem". These studies invariably found an average spacing value λ_{av} close to the spacing λ_m that leads to minimum undercooling (see Fig. A.2), and thus roughly varying as $V^{-1/2}$ –which speaks for the presence of a pattern selection mechanism. However, these studies also found a very large width of the spacing distribution about λ_{av} (from 20 to 50% in the most carefully controlled solidification conditions), which is clearly unfavorable to the selection hypothesis.

For a complete understanding of these phenomena, the spatio-temporal dynamics of the solidification front, including stationary and transient regimes, must be observed in real time. This can be achieved for two-dimensional (2-D) systems by using thin-sample directional solidification (TDS) [104, 105, 106] of a transparent model of nonfaceted metallic eutectics, namely CBr_4-C_2Cl_6. The crucible is made of two glass plates separated by calibrated spacers. When a sample thickness smaller than about 10 μm is chosen, the lamellae are forced to remain normal to the glass plates by wall effects. This imposes a strong 2-D character on the growth dynamics and allows observation in side view with an optical microscope. A small sample thickness also serves to block the thermo-solutal convection flows in the

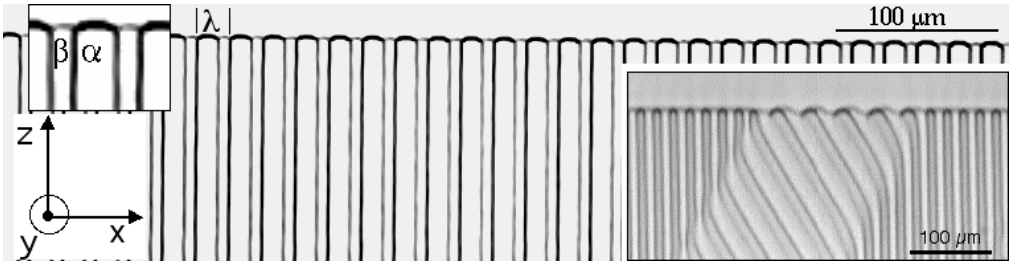

Figure A.1: Lamellar eutectic pattern observed in TDS of CBr_4-C_2Cl_6 ($C_0 \approx$ 11.6 mol%; $V = 0.5$ μms^{-1}). The growth direction is upward (axis z). The solid-solid interfaces, which trace the trajectories of the three-phase coexistence lines (trijunctions), provide a natural spatiotemporal diagram of the growth front. Here, these interfaces are aligned along the growth axis: the pattern is stationary. Inset: coexistence of a stationary pattern and a drifting pattern (tilt domain).

liquid, which are known to greatly perturb solidification in bulk samples, though three-dimensional (3-D) structures can be obtained at intermediate thickness before the onset of convection as described below.

Thin-sample directional solidification (TDS): The CBr_4-C_2Cl_6 system solidifies into transparent, nonfaceted, cubic phases (α: hypoeutectic, f.c.c phase; β: hypereutectic, b.c.c phase). The alloys are prepared by mixing zone-refined and outgased CBr_4 and C_2Cl_6 ($T_E = 84.4$°C ; $\lambda_m^2 V \approx 185 \mu$m^{3}s^{-1}) [19]. Thin samples (8 mm x 70 mm x 12 μm) are filled under controlled Ar atmosphere ($\approx$ 10mbar), and sealed after a rapid cooling at room temperature. The amount of residual impurities in the samples is of about 10^{-4} (mole fraction) [20], and its influence on the phenomena shown in this study is weak, unless otherwise noted.

The samples are placed in a horizontal temperature gradient G ($40 - 110 \pm$

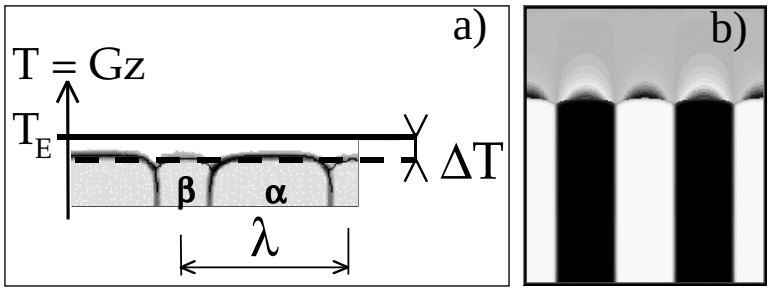

Figure A.2: (a) Large-magnification micrograph of a lamellar pattern. The average temperature of the front T_{av} is close to the eutectic temperature T_E, due to the coexistence of the two solids and the liquid. The departure from equilibrium is measured by the undercooling $\Delta T = T_E - T_{av} > 0$, and is determined by the mean curvature of the interface imposed by the equilibrium of the surface tensions on trijunctions and by the modulated concentration field in the liquid. ΔT is a function of λ and V, and presents a minimum, at given V, for a spacing value λ_m (minimum-undercooling spacing), which varies as $V^{-1/2}$ [102, 103]. (b) Numerical simulation of a stationary pattern; courtesy of M. Plapp [see M. Plapp and A. Karma, Phys. Rev. E **66**, 061608 (2002)]. The gray levels represent the diffusion field in the liquid.

10% Kcm^{-1}) realized between two well regulated copper blocks (within 0.01 K), and pulled toward the cold block at a constant velocity ($V = 0.125 - 30\mu\mathrm{ms}^{-1} \pm 2\%$). The growth front is continuously observed along the y direction (side view) with an optical microscope, and the images of the front are recorded with a CCD camera on video tapes, and analyzed numerically. The spacing distribution and the front profile are measured with a sensitivity of $0.05 - 0.1\mu$m (optical resolution is limited to about 1μm, but interpolation allows us to reach subpixel resolution) [107].

For the observation of homogeneous, extended patterns, large (containing 100–150 pairs of lamellae) eutectic grains (i.e., regions of a lamellar eutectic solid in which all the lamellae of each phase have the same crystal orientation) with a weak interfacial anisotropy were prepared following a procedure explained in Ref. [108]. The average spacing value is generally close to, but smaller than λ_m at the chosen V.

Stationary lamellae: Recent TDS studies, in conjunction with numerical simulations, have essentially solved the selection problem for one-dimensional (1D) fronts [105, 106, 107]. They have shown that, at given V, stationary lamellar fronts are stable for a finite-width range of spacings. Moreover, the lower and upper bounds of the stability interval (about $0.8\lambda_m$ and $2.3\lambda_m$, respectively, at the eutectic concentration for CBr_4-C_2Cl_6) approximately follow the similarity law $\lambda \propto V^{-1/2}$. This clearly provides the theoretical framework within which metallographic data can be interpreted. In brief, the distribution of spacings found in a sample depends on initial and boundary conditions (among which the eutectic grain structure plays a prominent role) of the solidification run. These dependencies are in addition to

the dependence on "standard" solidification parameters such as V and G, which provide a range of stable patterns. Since the stability interval varies as $V^{-1/2}$, the variation of λ_{av} over a sufficiently large V range also roughly follows a $V^{-1/2}$ law for standard solidification runs, whatever the detail of the spacing distribution may be.

Dynamic patterns: In addition to the preceding, prior TDS and numerical studies have revealed a wealth of new dynamical phenomena, in particular, the existence of a number of low-symmetry (drifting, and/or oscillatory) growth patterns, on top of the stationary patterns [105, 106]. These nonlinear patterns can emerge from stationary patterns through the spontaneous development of symmetry breaking instability modes without any change of the average spacing value, and independently of any crystallographic influence. For instance, the inset of Fig. A.1 shows a domain of a drifting pattern traveling inside a stationary pattern. The stability domains of these patterns in parameter space (morphology diagram) were determined both experimentally [106] and numerically [109] for CBr_4-C_2Cl_6. The quantitative agreement between experiments and numerical simulations performed without adjustable parameter is very good.

Open questions: These encouraging results have brought us closer to a fundamental understanding, but for predictive ab-initio modeling and accurate control of eutectic growth microstructures, many open questions still remain to be addressed:

1. *Microstructure control:* The standard solidification parameters only set the microstructure scale to within a factor of about 2. In addition, oscillatory or

chaotic patterns (or transients) often occur. What should one do if more accurate control is needed, especially in complex cast geometries? How could one adjust the microstructure locally, e.g. near edges in a cast? How can dynamical instabilities (which appear spontaneously under certain growth conditions) be triggered or suppressed in a more controlled fashion?

2. *Interfacial-anisotropy effects:* The influence of capillary anisotropy (i.e., the fact that surface tension of the solid-liquid and solid-solid interfaces depend on the orientation of these interfaces with respect to the crystal lattices of the solid phases) on eutectic patterns still has open questions. How strong is the influence of a weak anisotropy of the (nonfaceted) solid-liquid interfaces ? Is it possible to gain information about the physics of solid-solid interphase boundaries ?

A.2 Microstructure Control Through Adaptive Holograms

Background: Prior TDS investigations mostly utilized velocity jumps to trigger transitions from a homogeneous growth pattern to another. This is a strong, global perturbation method. For basic research, it has allowed investigation of non-linear phenomena (phase diffusion, domains, solitary waves), which appear during the transients, and sometimes persist for a long time, giving rise to chaotic patterns (Fig. A.3; also see ref. [110]).

More accurate control of the lamellae structure, and further insights into the chaotic dynamics described above can be achieved by applying local or patterned

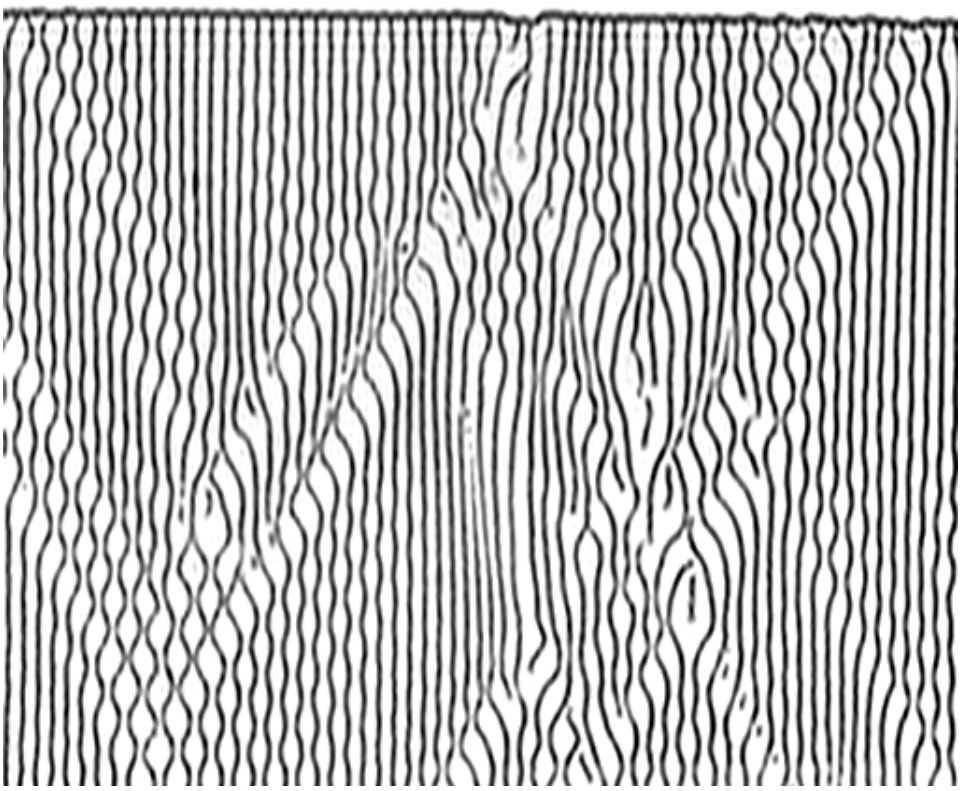

Figure A.3: Nonstationary, intermittent-like pattern in a CBr_4-C_2Cl_6 sample of concentration close to the eutectic one, observed after a velocity jump far above the threshold of the so-called period-doubling oscillatory instability ($C_0 \approx 11.6$ mol%; $G = 80$ Kcm^{-1}; $V = 0.5$ μms^{-1}). Horizontal dimension: 830 μm.

perturbations controlled in space and time. Prior experimental work by some of us has demonstrated basic control schemes for dendritic arrays in dilute binary alloys [92]. Theoretical work has demonstrated the possibility to use perturbations to e.g. stabilize an unstable planar growth front [96].

Method: Local perturbations of a growth front by a single laser beam [21] or by an array of fixed, regularly spaced spots of UV light [48] have been used previously for the study of sidebranching in dendritic growth and the dynamics of cellular fronts in dilute alloys. Then, the heating effect was due to the absorption of energy by a dye molecule, which is used as the second alloy component. The released heat diffuses in the liquid. The size of the heated region depends on the diameter of the spot and on (heat and solute) diffusion coefficients. Our thin samples were similar to those used in standard TDS experiments. Though the absorption of CBr_4 and C_2Cl_6 in the wavelength of the laser is extremely weak (less than a percent), it is sufficient to perturb the front. We utilize multiple independently movable local heating spots generated by an adaptive hologram that is incorporated into a microscope. A laser reflected off that hologram generates complex 3-D laser light patterns that locally heat or otherwise alter the sample. Such a holographic laser tweezer array has been available commercially since the summer of 2002 (Arryx Bioryx200) with up to 200 independently movable laser spots. The laser power can be varied from 0.2W to 2W, and the wavelength of the laser is 532nm.

Results: We studied the response of a well-stabilized stationary pattern (e.g., Fig. A.4a) to perturbations of varying amplitudes (Figs. A.5 and A.6). In Fig. A.4b, a single laser spot was targeted close to a trijunction during a short time period (a

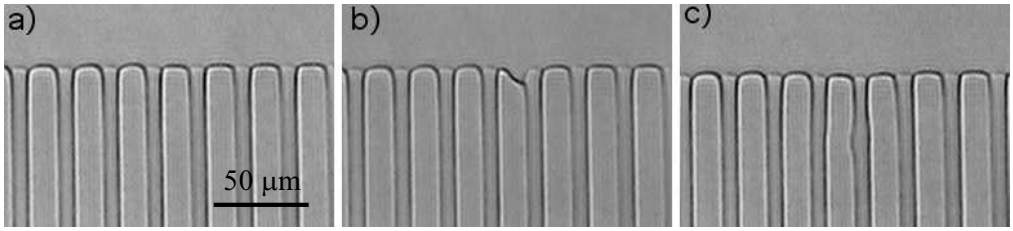

Figure A.4: Perturbation of a lamellar eutectic front by a single, small-power laser spot. (a) Initial, unperturbed stationary pattern; (b) Perturbation; (c) Recovery of the perturbation after 200 s ($V = 0.5\ \mu\text{ms}^{-1}$).

few seconds), causing the melting of a small portion of an α and a β lamellae. The short-scale perturbation thus induced relaxed rapidly, and was totally damped out within a few 10 s (Fig. A.4c).This observation (the very small size of the heated spot) clearly shows that laser light absorption occurs in the thin alloy layer, and not in the 300-μm thick glass walls enclosing the alloy.

In Fig. A.5a, a solidification front is exposed to a single spot moving continuously (at a velocity much larger than V) toward the front along the solidification axis. A large portion of the solid melts. The melting and the initial deformation of the front are essentially due to a strong deformation of the isotherms. Note that the α lamellae melt further back than the β lamellae (Fig. A.5) due to the fact that the constitutional undercooling in the diffusion layer favors the majority phase (β in the hypereutectic case), the liquidus temperature of which is much higher than that of the minority phase. After the perturbation is switched off, the excess heat diffuses rapidly over the whole sample. During this stage, a lamella is eliminated. Thereafter, the front slowly restabilizes by a "phase diffusion" process, meaning

that the time evolution of the spacing distribution $\lambda(x,t)$ obeys a diffusion law [99]. Here, a perturbation of characteristic length $\delta \approx 200\mu$m relaxes within about 100 s. This corresponds to a phase diffusion coefficient $D_\lambda \approx 2.5\mu\text{m}^2\text{s}^{-1}$, which is in good agreement with previous estimates of D_λ [107]. Note that, for a perturbation of characteristic length of $\delta = 30\mu$m as in Fig. A.4, and for D_λ (which depends on V and λ) of the order of 1 $\mu\text{m}^2\text{s}^{-1}$, the characteristic relaxation time $D_\lambda(2\pi/\delta)^2$ should be a few seconds. This rough estimate is also consistent with our observations.

In the case of Fig. A.5b, we melted a very large area of the solid with a moving laser spot for a long time. The relaxation process was very slow, and the long-lasting deformation of the front cannot be explained simply by thermal effects, but implies the presence of residual impurities - possibly generated by material decomposition due to excessive heating. No such effect of impurities was detected in the other examples described above (except for Fig. A.6a). The overall process in Fig. A.5b presents striking similarities with transient regimes preceding the formation of eutectic colonies [111]. Nevertheless, the front is stable against the formation of colonies, and a quasi stationary pattern with a gradually varying spacing forms.

One example of dynamical control is presented in Fig. A.6, which shows how a laser spot of appropriate size and location, and turned on at due time can start and stop a traveling wave. The initial stationary pattern was created at values of λ and V close to the threshold of the tilt instability. It can be seen that a perturbation can trigger or stop a localized instability such as a tilt domain (also see Fig. A.1) [105]. This indicates that various types of spatio-temporal laser perturbations can be applied to study the different modes of instabilities as well as to dynamically

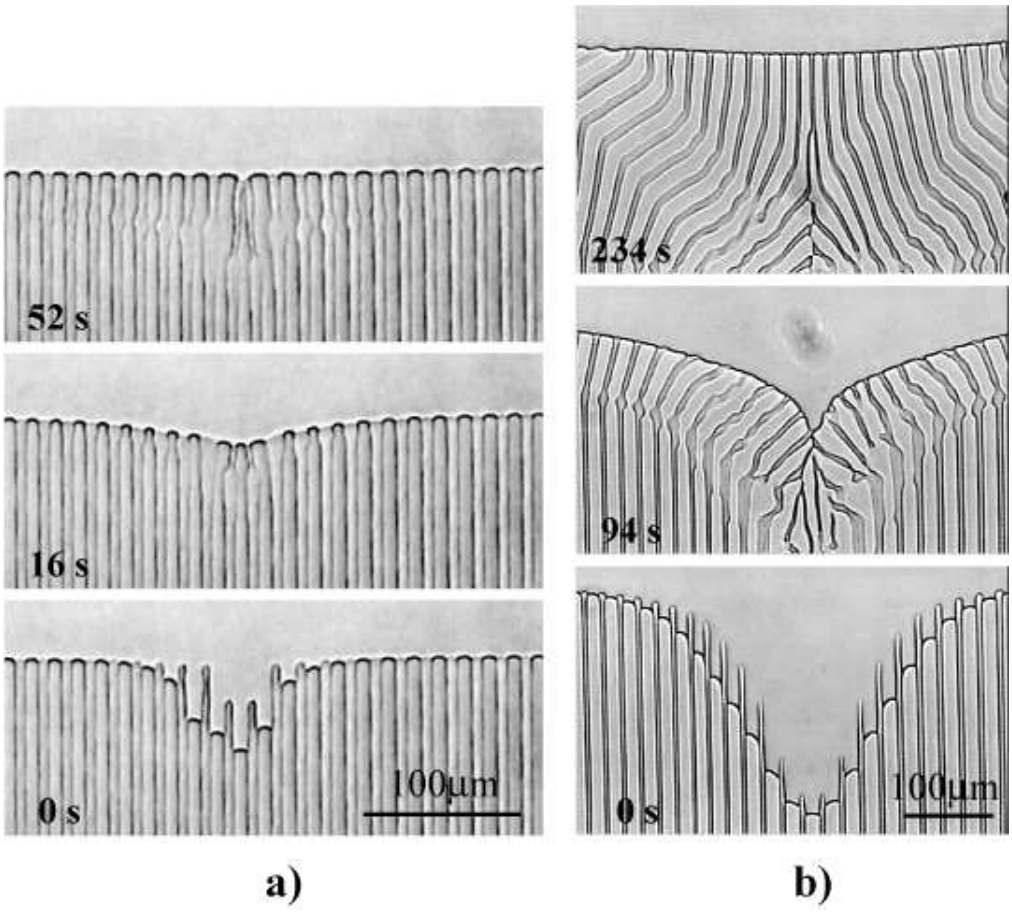

Figure A.5: Perturbation of a lamellar eutectic front by a single, small-power laser spot moving along the solidification axis toward the front (a) for 5 seconds ($V = 1.3\ \mu\text{ms}^{-1}$); (b) for 40 seconds ($V = 1.0\ \mu\text{ms}^{-1}$); note the spontaneous appearance of tilt domains.

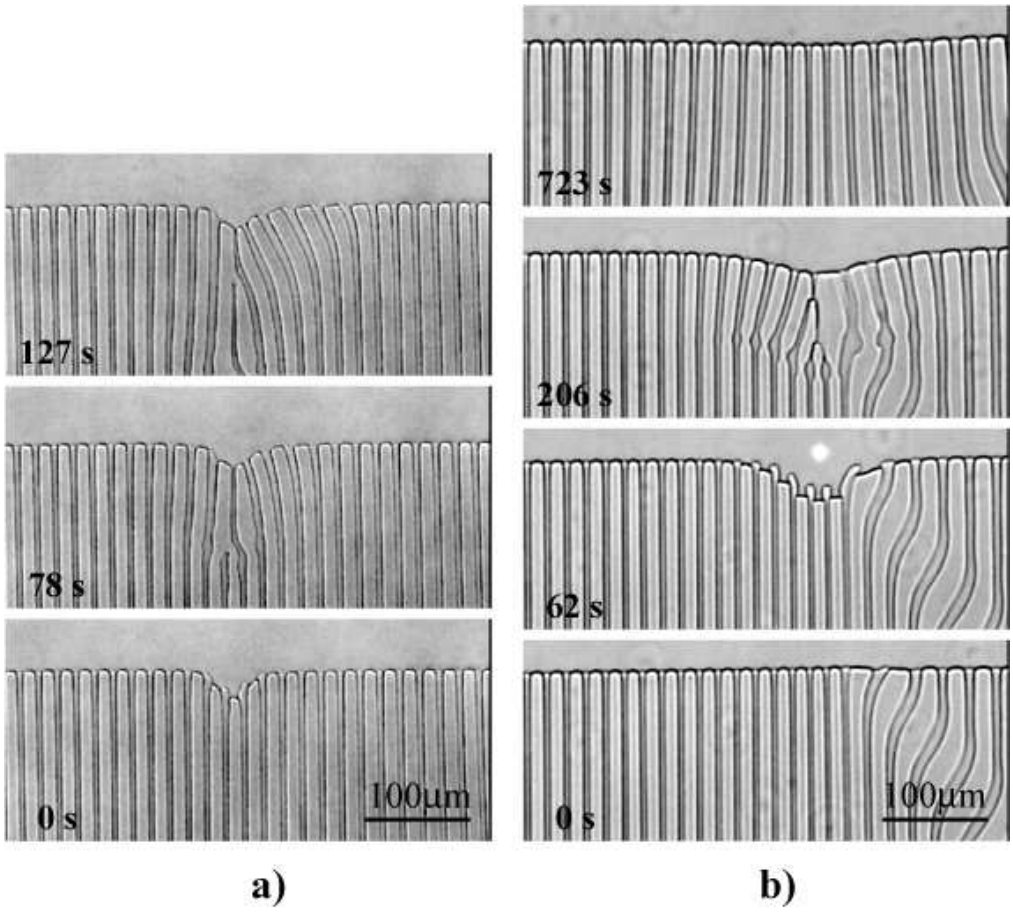

Figure A.6: Control of lamellar structure through localized laser perturbations. (a) Triggering local tilt instability ($V = 1.3\ \mu\text{ms}^{-1}$). (b) Stopping local tilt instability ($V = 0.7\ \mu\text{ms}^{-1}$).

control the microstructure.

These control techniques could be applied to real metallic alloys using holograms suitable for higher frequency light that can be partly transmitted through some materials, or (if less complex shaped perturbations are needed) interference patterns using ultrasound, X-rays, or microwave radiation of a frequency that gets partly absorbed by the material.

A.3 Analyzing Interface Anisotropy Through Confocal Microscopy

Background: Capillary anisotropy (which does not play a role in the phenomena described above) can strongly influence eutectic patterns. Previous studies pointed out that locking and faceting of the solid-solid interface occur when its anisotropy is large. These phenomena have a marked influence on the macroscopic dynamics, but their basic mechanisms occur on too small a scale to be observed with a conventional optical microscope, where interfaces appear broader, since they are not perfectly flat in the third dimension over which standard microscopy averages.

Method: We used reflection scanning confocal microscopy (with a Leica TCS SP2) which has the capability of eliminating out-of-focus light and collecting only the reflected light from the focal plane, therefore, reproducing sharp interfaces with resolution down to hundreds of nm.

Results: The micrograph of Fig. A.7 shows an oscillating pattern observed in TDS of a nearly eutectic CBr_4-C_2Cl_6 alloy. This kind of pattern, called "giant oscillation", is obtained at relatively low solidification rate for large values of the spacing ($\lambda/\lambda_m > 3$) [106]. The large amplitude (nearly equal to λ) of the oscillation imposes, in addition to relatively large deformations of the solid-liquid interfaces, that the solid-solid interfaces explore all orientations from -90° to 90° with respect to z. In the right hand side of the micrograph of Fig. A.7a, the shape of α-β interfaces exhibits small kinks and facets, which are absent in the remainder of the image, i.e., in a different eutectic grain. We recall that the α- and β-liquid interfaces are nonfaceted. Therefore, the formation of facets can only be attributed to a strong

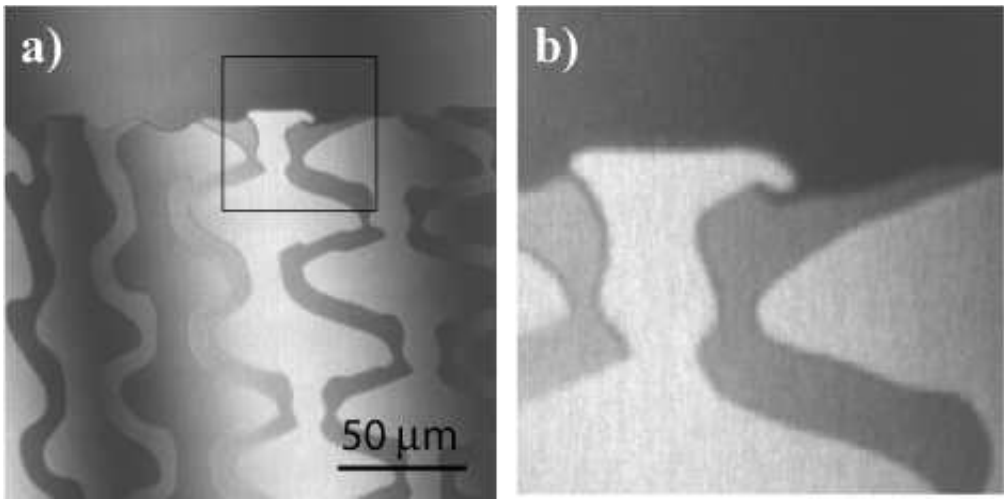

Figure A.7: (a) Giant-oscillation pattern in a thin sample of a nearly eutectic CBr_4-C_2Cl_6alloy observed in reflected-light confocal microscopy ($V = 1.1\ \mu\mathrm{ms}^{-1}$). (b) A magnified detail of the front (square portion in (a)).

anisotropy of the α-β surface tension. This anisotropy depends critically on the relative orientation of the two crystal lattices, and facets form only for singular α-β orientation relationships.

It can also be seen in a magnified detail of the front (Fig. A.7b) that, at some moments, a very small finger of the α phase overhangs transiently the neighboring lamella, which indicates that the α-β interface cannot turn continuously during the oscillation. We think that the presence of kinks (or edges) in the shape of the α-β interface is due to the existence of a finite angular sector of forbidden orientations for the interface. This detail of the shape of the front could not have been resolved with classical microscopy.

Large-scale perturbations causing an ample modulation of the front shape as shown in Fig. A.5 can also be used, in principle, to tilt phase boundaries and

reveal the possible existence of preferred orientations of the solid-solid interface. This also may be an indirect means, based on mesoscale observations, to determine the orientation of the two solid phases (and singular orientations of the solid-solid interface), if combined with independent crystallographic measurements.

Finally, if one adds a laser dye in the eutectic alloy, one can use high-resolution fluorescence imaging microscopy such as fluorescence confocal or two-photon microscopy to image the impurity(dye) concentration field directly. A study of impurity segregation at phase boundaries with this technique is under consideration.

A.4 Conclusion

We have shown two applications of advanced optical techniques (holographic laser spots and confocal microscopy) to laboratory experimental research on fundamental aspects of the dynamics of lamellar eutectic fronts. These results show encouraging prospects in the following directions:

1- The possibility of triggering at will localized instabilities should allow us to gain a deeper insight into spatio-temporal chaotic or intermittent regimes, and help in the design of new microstructure control techniques.

2- The use of high-resolution, reflected-light confocal microscopy gives a unique means of investigation into the physics of anisotropic solid-liquid and solid-solid interfaces.

In addition, the feasibility of imaging slow growing 3-D eutectic structure by confocal microscopy is under consideration.

These are only preliminary results for most of these new instruments. They point to the potential to directly probe microstructure stability, to investigate 3-D structures, and to develop new techniques that may be used to accurately control lamellar patterns. These studies also aim to close the gap between fundamental investigations of nonequilibrium dynamics of pattern formation, which has investigated a rich phase space of patterns and dynamical phenomena, and their practical application in real casts.

Appendix B

Sample Preparation

B.1 Capillary Cleaning

The thin (100 μm $\times$ 2 mm $\times$ 30 cm or 200 μm $\times$ 4 mm $\times$ 30 cm) glass capillaries (Vitro Dynamics) need to be cleaned before filling in with SCN/C152 (Fig. B.1). We connect one end of the capillary to a funnel through a Teflon holder. The other end of the capillary is connected to a flask through a Teflon holder and a rubber stopper. We connect the flask to a venturi pump and keep it constantly at low pressure so that the fluid we pour in the funnel is pulled through the inside of the capillary due to the pressure difference. First, we pour warm soapy water (1% Alconox solution) twice and let it flow through. Then, we let distilled water flow through. At last, we let a little amount of aceton flow in to remove water. We then put the capillary in a vacuum oven (130 °C, 400 mmHg) overnight. We seal both ends of the capillary with a torch.

B.2 Distillation of SCN

SCN (99%, 500g, Sigma-Aldrich, St. Louis, MO) is distilled three times before mixing with C152. In the first distillation the middle third is collected and used as a source for the second distillation. In the second distillation again the middle third is collected and used as a source for the third distillation. In the third distillation

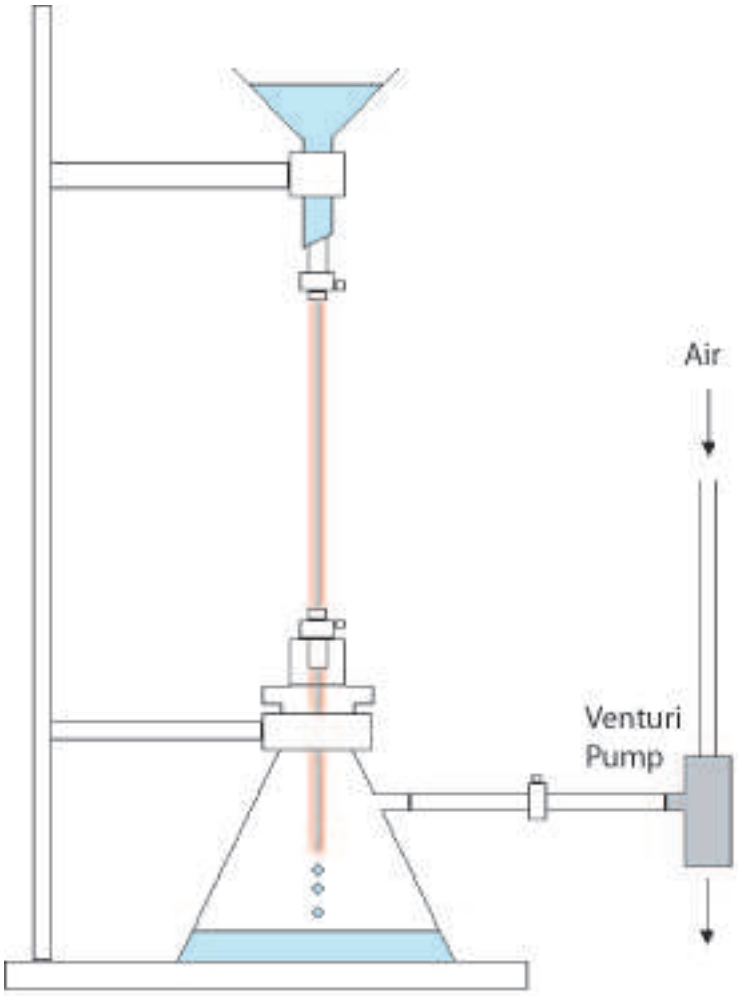

Figure B.1: Schematic of the capillary cleaning.

the middle third is collected into a 25ml graded glass buret for sample filling.

The distillation setup is shown in Fig. B.2. We put SCN in a big funnel and melt it with a heatgun under a fume hood so that it flows into a flask. We connect the flask to the distillation setup (the flask 1 in Fig. B.2). An empty flask with a stopper is connected (the flask 2 in Fig. B.2). We establish a vacuum (100-200mTorr) throughout the system with valves A,C, and D open, and B and E closed. The temperature of the condenser is constantly held at 75 °C by water circulation. The shaded parts of the setup are heated by electrical heating tapes. The shaded part on the side of the flask 1 is held at the temperature 95 °C, and the the flask 2 side is held at 80 °C. We put an electrical heater (120 °C) under the flask 1 to melt SCN. When one third of the original amount of SCN is collected in the flask 2, we stop heating the flask 1 and wait until SCN solidifies. Then, we close the stopper of the flask 1 and wait until all the SCN is cleared from the passage. We close the stopper of the flask 2 and close valves A and C and open valve B. Then, we open valve E and remove the stopper next to valve E to let the air in. We place another flask with the stopper open for collecting SCN. We put the stopper back in and close valve E. We close valve B and open valves A and C to establish the vacuum throughout the system. We follow the same procedure to collect the second third into the flask 2, which will be the source for the second distillation. We follow the same procedure for the second and third distillations.

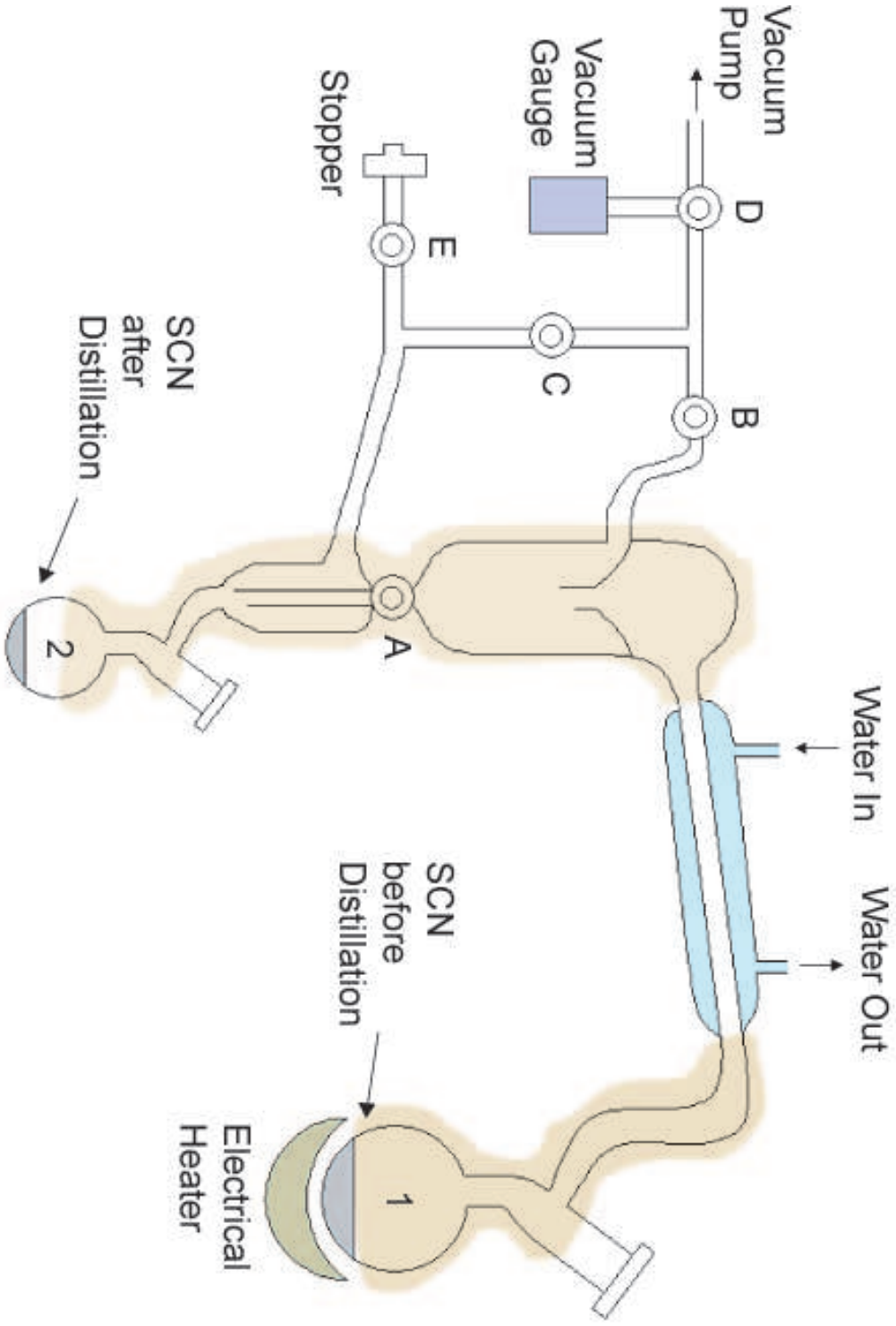

Figure B.2: Schematic of the distillation of SCN.

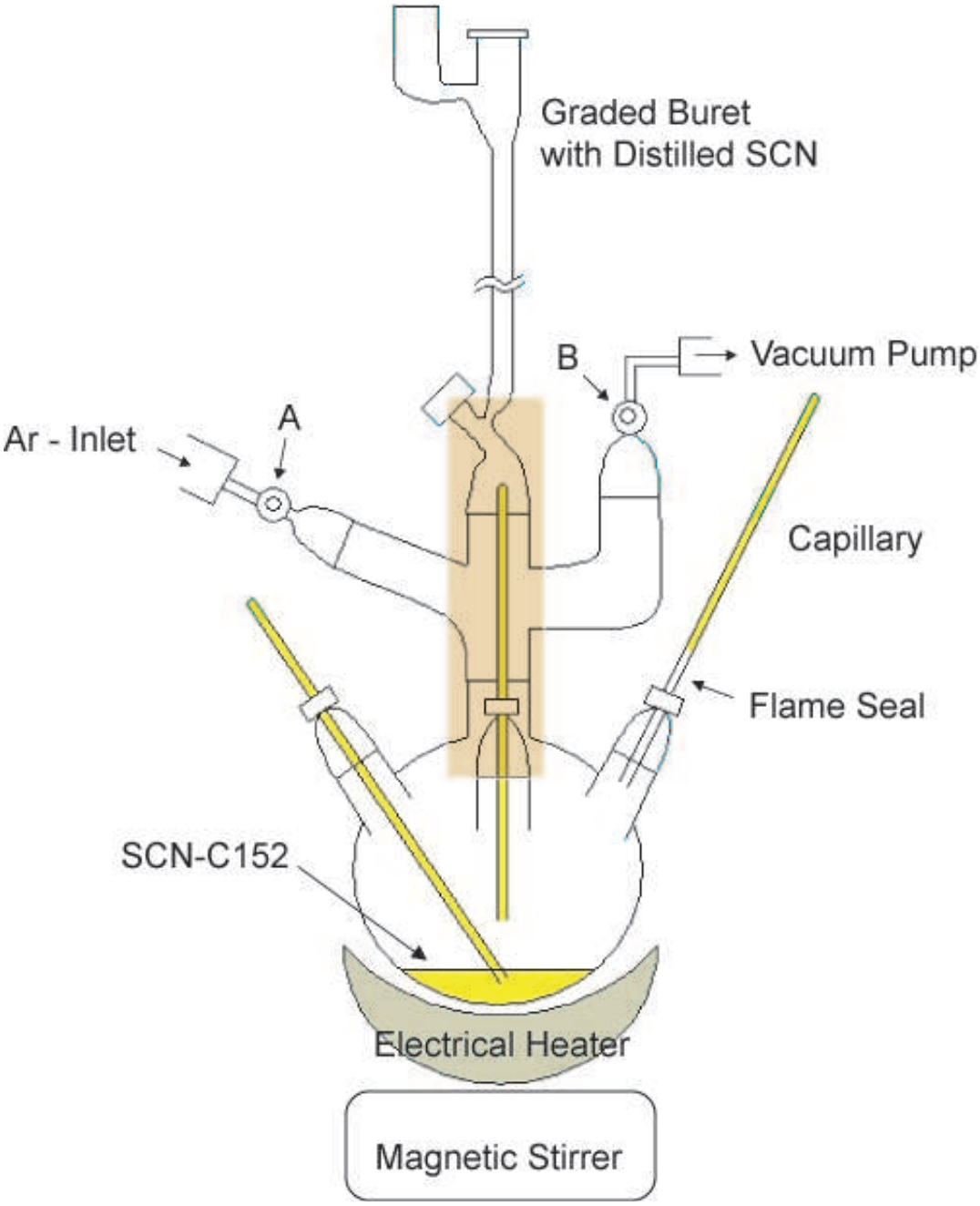

Figure B.3: Schematic of the sample capillary filling.

B.3 Filling the Sample Capillaries

A schematic of the sample capillary filling setup is shown in Fig. B.3. We connect the buret with distilled SCN to the system and wrap heating tapes around the shade part of the system. Before installing the capillaries we put plugs in the three necks of the mixing flask and establish a vacuum (100-200mTorr) by opening valve B. We let a small amount of Ar gas into the system to remove the possibility of mixing vacuum grease with SCN. The pressure of Ar is greatly lowered by triple valves (the first two Ar valves are kept open to give 10 psi before the last Ar valve). To let the Ar gas in, we open valve A and then the last Ar valve. We put screw caps with rubber covers on three inlet adapters. The rubber covers have are clamped between the screw caps and the inlet adapters for for a vacuum tight seal of the inlet. We dip one end of the cleaned and sealed capillary in vacuum grease and insert into the inlet adapter through a small slit in the rubber in the outward direction so that the clean end of the capillary can go into the flask. We put a measured amount of C152 (3-30mg, depending on the concentration we want) and a magnetic stirrer into the flask. Then, we break off the clean ends of the capillaries and insert the inlet adapters into the three necks of the flask. The capillary end is positioned above the expected level of SCN filling. We ice cool the flask to minimize the possible sublimation losses. We establish the vacuum again by opening valve B. We heat the buret with a heatgun to melt SCN. Then, we close valve B and open the buret valve. As soon as a measured amount (8ml) of SCN flows into the flask, we open valve B. SCN immediately solidifies due to ice cooled flask. We put an electrical

heater (80 °C) to melt SCN. As soon as SCN melts, we close valve B and make C152 mix with SCN using the magnetic stirrer for 3-5 minutes. Once in a while we stop the stirrer and open valve B to ensure the vacuum. When mixing is complete, we stop the stirrer and open valve B. We clean the exposed part of capillaries and heat the capillaries with the heatgun. Then, we lower the capillaries and dip the open ends into SCN-C152 mixture. Capillary action fills approximately one third of the capillaries. While heating the capillaries we open valve A and carefully the Ar valve to let Ar gas in. As soon as the Ar pressure fills the capillaries completely, we close the Ar valve. We stop heating the capillaries and ice cool the flask so that the mixture inside the capillaries quickly solidifies. We raise the capillaries and heat carefully the parts still inside the inlet adapter with the heatgun to remove the mixture from the parts. We raise the capillaries a little more so that a portion of the part from which the mixture is removed is outside of the inlet adapter (see the rightmost capillary in Fig. B.3). We wipe the area to be sealed and also heat the area by several quick swipes across the capillary with a torch to remove residues sticking to the glass. We tip off and seal the capillary with the torch. If the buret still has SCN for next sample filling, we remove SCN-C152 residues from the buret with the heatgun.

Appendix C

Image Analysis

We used the commercial software Interactive Data Language (IDL from RSI Inc.) to write our image analysis routines. In the following sections, our IDL programs (*.pro) used for extracting shapes and physical quantities are listed with a brief description, inputs, outputs, important parameters and typical values of the parameters.

C.1 Programs for Dendrite Tip Extraction

qcell_dendrite.pro This program is used to extract the shapes of dendrites from a sequence of original images (from Fig. C.1a to b). The intensity profile obtained by scanning along the x and y directions over the interface is fit to a parabola to give the position (with subpixel resolution), brightness, and thickness of the interface.

INPUTS:

a sequence of TIF image files

OUTPUTS:

x, y, intensity (brightness of interface), radius of curvature of parabola (thickness of interface)

PARAMETERS:

bpass1=1 (characteristic lengthscale of noise in pixels)

bpass2=4 (characteristic width of boundary in pixels)

thresh=40 (minimum intensity value of pixels which will be taken into account)

qtip_finder.pro This program is used to find the tips of dendrites (from Fig. C.1b to c and d). The tip is fit to a parabola to give the position and radius of curvature of the tip.

INPUTS:

gdf files created by qcell_dendrite.pro

OUTPUTS:

x, y, R (radius of curvature of tip), frame number, uncertainty in radius

PARAMETERS:

dx=7 (x-range of pixels used for fitting, depends on tip size in consideration)

std_tol=.1 (standard tolerance in fitting)

min_num_feat=14 (minimum number of points required to be fit, about two times dx)

max_curvature=.4 (maximum curvature to be considered as a tip)

min_curvature=.04 (minimum curvature to be considered as a tip)

tip_track.pro This program is used to track dendrite tips in time. Each tip is identified with a tip track number and the position, radius, and velocity of the tip is given at each frame.

INPUTS:

a gdf file created by qtip_finder.pro

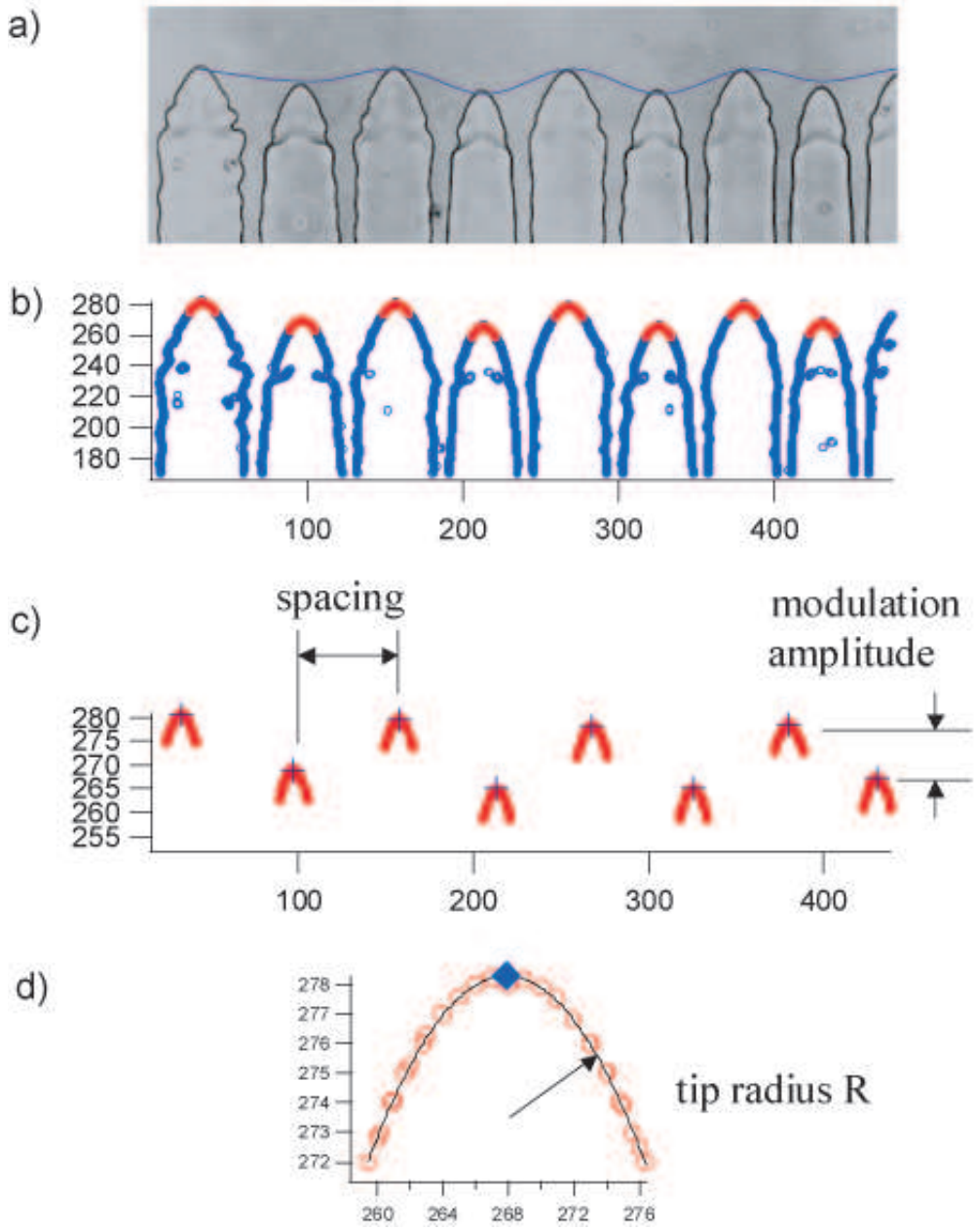

Figure C.1: (a) An original image. (b) Extracted dendrite shape. (c) Obtaining tip positions. (d) Obtaining tip radius.

OUTPUTS:

x, y, R (radius of curvature of tip), frame number, tip track number, V_x, V_y, V

PARAMETERS:

deltacut=10 (number of pixels on fringe that will be ignored) deltamax=3 (maximum displacement between frames)

goodenough=50 (minimum length of trajectory)

steps_memory=3 (number of time steps that dendrite tip is remembered if temporarily obscured)

dendrite_spacing.pro This program is used to obtain the spacings between neighboring dendrites (Fig. C.1c). At each frame the differences in tip positions and tip radii between every pair of neighboring dendrites are calculated.

INPUTS:

gdf file created by tip_track.pro

OUTPUTS:

frame number, Δx, Δy, ΔR for two neighboring tips

PARAMETERS:

None

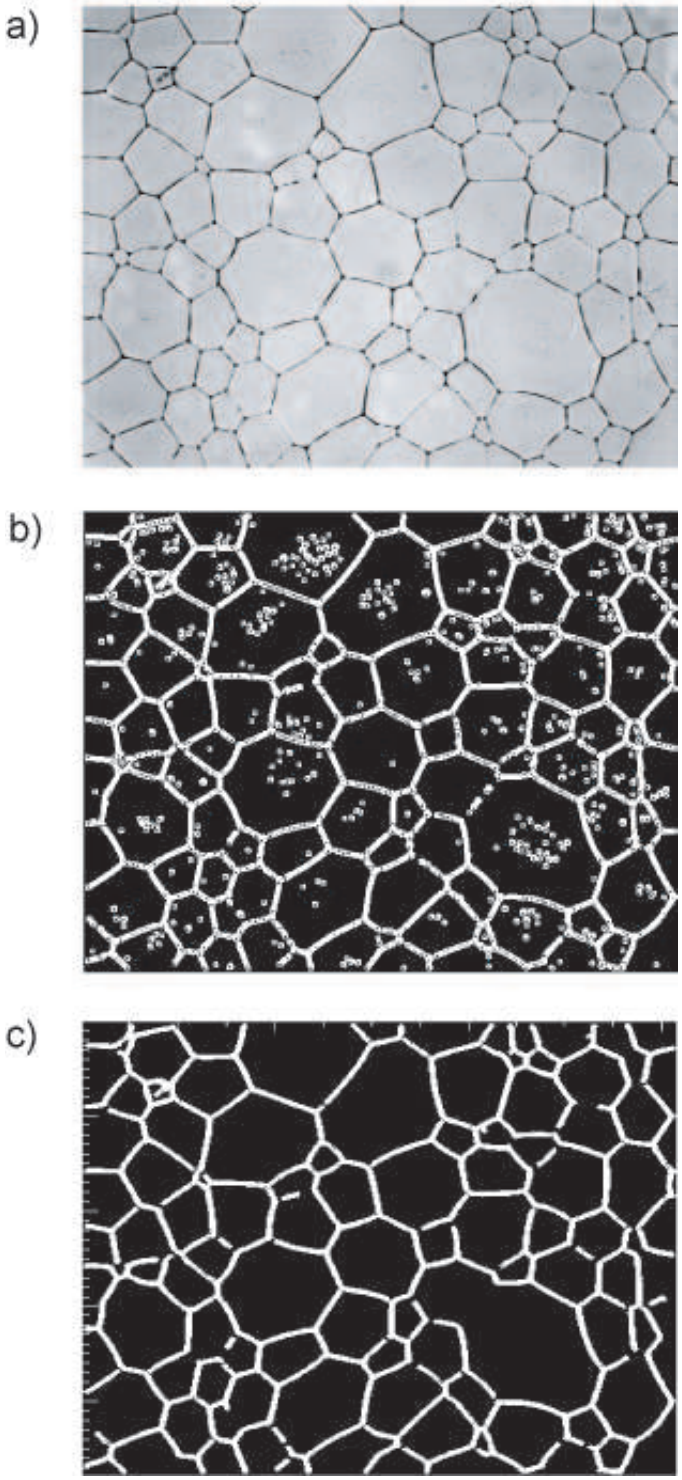

Figure C.2: (a) An original image. (b) Extracted grain boundaries with noises. (c) Extracted grain boundaries after noises are removed.

C.2 Programs for Grain Boundary Extraction

grain_boundary_scan.pro This program is used to extract grain boundaries from a sequence of original images (from Fig. C.2a to b). This is the same as qcell_dendrite.pro except that the output includes the direction of scanning, which will be needed in

grain_boundary_track.pro.

INPUTS:

a sequence of TIF image files

OUTPUTS:

x, y, radius of curvature of tip, frame number, uncertainty in radius, scan direction

PARAMETERS:

bpass1=1 (characteristic lengthscale of noise in pixels)

bpass2=4 (characteristic lengthscale of boundary in pixels)

thresh=40 (minimum intensity value of pixels which will be taken into account)

grain_boundary_track.pro This program is used to remove noises that are still present in the grain boundary data obtained by

grain_boundary_scan.pro (from Fig. C.2b to c). At each frame the points on grain boundaries are spatially tracked in the x and y directions to eliminate the points not on the boundaries and to give the slopes of the boundaries.

INPUTS:

gdf files created by grain_boundary_scan.pro

OUTPUTS:

x, y, boundary points track number, slope, frame number

PARAMETERS:

deltacut=2 (number of pixels on fringe that will be ignored) deltamax=5 (maximum displacement between frames)

goodenough=20 (minimum length of trajectory)

steps_memory=500 (number of time steps that a grain boundary point is remembered if temporarily obscured)

smoothvel=10 (number of points over which to smooth the velocity vector)

C.3 Programs for Obtaining Speed of Grain Boundaries

grain_boundary_scan_x.pro This program is used to extract grain boundaries from a sequence of original images. This is the same as grain_boundary_scan.pro except that the scanning is done only in the x direction for the purpose of boundary points tracking in the y direction in the next step grain_boundary_track_y.pro.

INPUTS:

a sequence of TIF image files

OUTPUTS:

x, y, radius of curvature of tip, frame number, uncertainty in radius, scan direction

PARAMETERS:

bpass1=1 (characteristic lengthscale of noise in pixels)

bpass2=4 (characteristic lengthscale of boundary in pixels)

thresh=40 (minimum intensity value of pixels which will be taken into account)

grain_boundary_track_y.pro This program is used to remove noises that are still present in the grain boundary data obtained by qcell_dendrite_xscan.pro. This is the same as grain_boundary_track.pro except that the points on grain boundaries are tracked only in the y direction for the purpose of temporal boundary tracking in the x direction in the next step grain_boundary_speed.pro.

INPUTS:

gdf files created by grain_boundary_scan_x.pro

OUTPUTS:

x, y, boundary track number, frame number

PARAMETERS:

deltacut=2 (number of pixels on fringe that will be ignored) deltamax=5 (maximum displacement between frames)

goodenough=20 (minimum length of trajectory)

steps_memory=500 (number of steps that particle is remembered if temporarily obscured)

grain_boundary_speed.pro This program is used to obtain grain boundary speeds in the x direction (Fig. C.3). All the points on the boundaries are tracked from frame to frame. Since we are interested in the speed in the x direction, in order to avoid tracking in the y-direction, the y-coordinates of boundary points are multiplied by

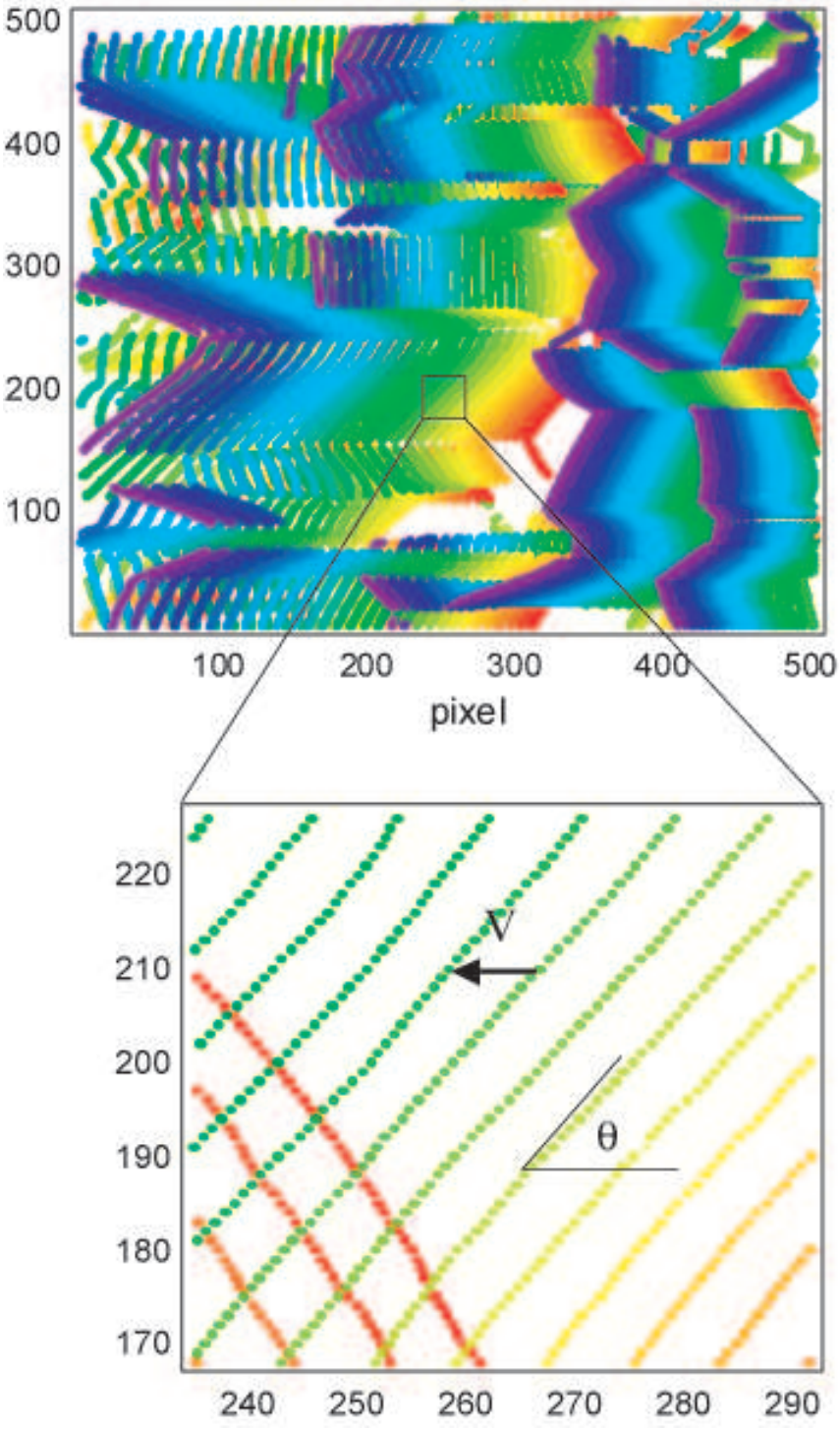

Figure C.3: Extracting grain boundary speed and slope. The colors represent time.

a large number to separate them apart in the y direction.

INPUTS:

a gdf file created by grain_boundary_track_y.pro

OUTPUTS:

x, y, V_x, frame number

PARAMETERS:

deltacut=10 (number of pixels on fringe that will be ignored) deltamax=2 (maximum displacement between frames)

goodenough=50 (minimum length of trajectory)

steps_memory=20 (number of steps that particle is remembered if temporarily obscured)

yexpand=10000 (factor multiplied to y-coordinates)

BIBLIOGRAPHY

[1] A. Ohno, *The Solidification of Metals*, Chijin Shokan Co. Ltd., Tokyo (1976).

[2] D.A. Porter and K.E. Easterling, *Phase Transformations in Metals and Alloys, 2nd edition*,Nelson Thornes Ltd., U.K. (2001).

[3] W. Kurz and D. J. Fisher, *Fundamentals of solidification, 4th revised edition*, Trans Tech Publications (1998).

[4] W. Wu, S.H. Brongersma, M. Van Hove, and K. Maex, *Appl. Phys. Lett.* **84**, 2838 (2004).

[5] J.W. Kysar, *Mater. Res. Soc. Symp. Proc.* **586**, 219 (2000).

[6] C. Yuan, J.T. Guo, and H.C. Yang, *Mater. Sci. Eng.* **18**, 73 (2002).

[7] *http://www.mme.tcd.ie/ tlgnphln/Brittle.html*

[8] *http://www.mme.tcd.ie/ tlgnphln/Creep.html*

[9] G. Zhang, D. Deng, B. Huang, W. Guang, and Z. Yin *Guijinshu (Precious Metals)* **20**, 42 (1999).

[10] S. Kumai, J. Hu, Y. Higo, and S Nunomura, *Acta Mater.* **44**, 2249 (1996).

[11] C.H. Caceres and J.R. Griffiths, *ICSMA 10, Proceedings of the 10th International Conference*, 451 (1994).

[12] N.R. Grugel, *Metall. Trans. A* **A26**, 496 (1995).

[13] N. Garnier, R.O. Grigoriev, and M.F. Schatz, *Phys. Rev. Lett.* **91**, 054501/1 (2003).

[14] K.A. Jackson and J.D. Hunt, *Acta Metall.* **13**, 1212 (1965).

[15] J.D. Hunt, K.A. Jackson, and H. Brown, *Rev. Sci. Instr.* **37**, 805 (1966).

[16] M. A. Eshelman, V. Seetharaman and R. Trivedi, *Acta Metall.* **36**, 1165 (1988).

[17] L. X. Liu and J. S. Kirkaldy, *J. Cryst. Growth* **140**, 115 (1994).

[18] P. Molho, A.J. Simon, and A. Libchaber, *Phys. Rev. A* **42**, 904 (1990).

[19] J. Mergy, G. Faivre, C. Guthmann and R. Mellet, *J. Cryst. Growth* **134**, 353 (1993).

[20] S. Akamatsu and G. Faivre, *J. Phys. I France* **6**, 5037 (1996).

[21] X.W. Qian and H.Z. Cummins, *Phys. Rev. Lett.* **64**, 3038 (1990).

[22] W.D. Huang, X.G. Geng, and Y.H. Zhou,] *J. Cryst. Growth* **134**, 105 (1993).

[23] M. Georgelin and A. Pocheau, *Phys. Rev. E* **57**, 3189 (1998).

[24] M.A. Palmer, V.E. Fradkov, M.E. Glicksman, and K. Rajan, *Scripta Metall. Mater.* **30**, 633 (1994).

[25] M.A. Palmer, K. Rajan, M.E. Glicksman, V.E. Fradkov, and J. Nordberg, *Metall. Mater. Trans. A* **26A**, 1061 (1995).

[26] M.A. Palmer, M.E. Glicksman, and K. Rajan, *Philos. Mag. A* **79**, 763 (1999).

[27] M.A. Palmer, M.E. Glicksman, and K. Rajan, *Scripta Mater.* **48**, 1173 (2003).

[28] D. Bouchard and J.S. Kirkaldy, *Metall. Trans. B* **27B**, 101 (1996).

[29] M. Gunduz and E. Cadirli, *Mat. Sci. Eng. A* **A327**, 167 (2002).

[30] L. Helfen, D.T. Wu, R. Birringer, and C.E. Krill III, *Acta Mater.* **51**, 2743 (2003).

[31] W.W. Mullins, *J. Applied Phys.* **27**, 900 (1956).

[32] J. von Neumann, in *Metal Interfaces*, ed. C. Herring, ASM, Cleveland, OH (1952), p.108.

[33] J.E. Burke and D. Turnbull, *Prog. Met. Phys.* **3**, 220 (1952).

[34] D. Weaire and S. McMurry, in *Solid State Physics Vol. 50*, Academic Press Inc. (1997), p.1.

[35] C. Sire, *Phys. Rev. Lett.* **72**, 420 (1994).

[36] C. Monnereau, N. Pittet, and D. Weaire, *Europhys. Lett.* **52**, 361 (2000).

[37] J.A. Glazier, *Phys. Rev. Lett.* **70**, 2170 (1993).

[38] F.N. Rhines and B.R. Patterson, *Metall. Trans. A* **13**, 985 (1982).

[39] F.C. Hull, *Mater. Sci. Technol.* **4**, 778 (1988).

[40] C. Monnereau and M. Vignes-Adler, *Phys. Rev. Lett.* **80**, 5228 (1998).

[41] S. Hilgenfeldt, A.M. Kraynik, S.A. Koehler, and H.A. Stone, *Phys. Rev. Lett.* **86**, 2685 (2001).

[42] S. Akamatsu, G. Faivre, and T. Ihle, *Phys. Rev. E* **51**, 4751 (1995).

[43] B. Utter and E. Bodenschatz, *Phys. Rev. E* **66**, 051604 (2002).

[44] M. Muschol, D. Liu, and H.Z. Cummins, *Phys. Rev. A* **46**, 1038 (1992).

[45] W.W. Mullins and R.F. Sekerka, *J. Appl. Phys.* **35**, 444 (1964).

[46] J.A. Warren and J.S. Langer, *Phys. Rev. E* **47**, 444 (1993).

[47] R. Trivedi and K. Somboonsuk, *Acta Metall.* **33**, 1061 (1985).

[48] W. Losert, B.Q. Shi, and H.Z. Cummins, *Proc. Nat. Acad. Sci. USA* **95**, 431 (1998).

[49] W. Losert, B.Q. Shi, and H.Z. Cummins, *Proc. Nat. Acad. Sci. USA* **95**, 439 (1998).

[50] P. Kopczynski, A. Karma, and W.-J. Rappel, *Phys. Rev. Lett.* **77**, 3387 (1996).

[51] W.J. Boettinger, S.R. Coriell, A.L. Greer, A. Karma, W. Kurz, M. Rappaz, and R. Trivedi, *Acta Mater.* **48**, 43 (2000).

[52] S.H. Davis, *Theory of Solidification* (Cambridge University Press, Cambridge, 2001).

[53] B.J. Spencer and H.E. Huppert, *Acta Mater.* **45**, 1535 (1997); **46**, 2645 (1998).

[54] B.J. Spencer and H.E. Huppert, *J. Cryst. Growth* **200**, 287 (1999).

[55] G.P. Ivantsov, *Dokl. Akad. Nauk. SSSR* **58**, 567 (1947).

[56] S.Z. Lu and J.D. Hunt, *J. Cryst. Growth* **123**, 17 (1992).

[57] J.A. Warren and J.S. Langer, *Phys. Rev. A* **42**, 3518 (1990).

[58] W. Losert, B.Q. Shi, H.Z. Cummins, and J.A. Warren, *Phys. Rev. Lett.* **77**, 889 (1996).

[59] W. Losert, O.N. Mesquita, J.M.A. Figueiredo, and H.Z. Cummins, *Phys. Rev. Lett.* **81**, 409 (1998).

[60] S.H. Han and R. Trivedi, *Acta Metall. Mater.* **42**, 25 (1994).

[61] S.K. Sarkar, *Phys. Lett. A* **117**, 137 (1986).

[62] O. Martin and N. Goldenfeld, *Phys. Rev. A* **35**, 1382 (1987).

[63] A. Dougherty, P.D. Kaplan, and J.P. Gollub, *Phys. Rev. Lett.* **58**, 1652 (1987).

[64] L.M. Williams, M. Muschol, X. Qian, W. Losert, and H.Z. Cummins, *Phys. Rev. E* **48**,489 (1993).

[65] W. van Saarloos, *J. Cryst. Growth* (To appear).

[66] W. van Saarloos, B. Caroli, and C. Caroli, *J. Phys. I France* **3**, 741 (1993).

[67] B. Echebarria and A. Karma, (Unpublished).

[68] W. Losert, D.A. Stillman, H.Z. Cummins, P. Kopczynski, W.-J. Rappel, and A. Karma, *Phys. Rev. E* **58**, 7492 (1998).

[69] J.T. Fredrich, B. Menedez, and T.-F. Wong, *Science* **268**, 276 (1995).

[70] M.G. Reed, C.V. Howard, and C.G. Shelton, *J. Microscopy* **185**, 313 (1997).

[71] S.A. Koehler, S. Hilgenfeldt, E.R. Weeks, and H.A. Stone, *Phys. Rev. E* **66**, 040601(R) (2002).

[72] T. Wilson and C.J.R. Sheppard, *Theory and Practice of Scanning Optical Microscopy*, Academic Press, London (1984).

[73] J.B. Pawley, *Handbook of Biological Confocal Microscopy*, Plenum, New York (1990).

[74] *Leica Confocal Microscope Manual*, Leica Microsystems Inc..

[75] W. Denk, J.H. Strickler, and W.W. Webb, *Science* **248**, 73 (1990).

[76] *http://www.udel.edu/bio/research/facilities/microscopy/equipment/multimgs .html*

[77] M. Tormen, L. Businaro, M. Altissimo, F. Romanato, S. Cabrini, F. Perennes, R. Proietti, H.-B. Sun, S. Kawata, and E. Di Fabrizio, *Microel. Eng.* **73-74**, 535 (2004).

[78] S. Maruo and S. Kawata, *J. Microelectromech. Syst.* **7**, 411 (1998).

[79] H.-B. Sun, T. Kawakami, Y. Xu, J.-Y. Ye, S. Matuso, H. Misawa, M. Miwa, and R. Kaneko, *Opt. Lett.* **25**, 1110 (2000).

[80] H.-B. Sun, S. Matuso, and H. Misawa, *Appl. Phys. Lett.* **74**, 786 (1999).

[81] B.H. Compston, S.P. Ananthavel, S. Barlow, D.L. Dyer, J.E. Ehrlich, L.L. Erskine, A.A. Heikal, S.M. Kuebuler, I.-Y. Sandy Lee, D.M. Maugon, J. Qin, H. Rokel, M. Rumi, X. Wu, S.R. Marder, and J.W. Perry, *Nature* **398**, 51 (1999).

[82] H.-B. Sun, V. Mizeikis, Y. Xu, S. Juodkazis, J.-Y. Ye, S. Matsuo, and H. Misawa, *Nature (London)* **412**, 667 (2001).

[83] S. Kawata, H.-B. Sun, T. Tanaka, and K. Takada, *Appl. Phys. Lett.* **74**, 786 (1999).

[84] P. Galajda and P. Ormos, *Appl. Phys. Lett.* **78**, 249 (2001).

[85] A. Lachish-Zalait, D. Zbaida, E. Klein, and M. Elbaum, *Adv. Funct. Mat.* **11**, 218 (2001).

[86] W.M. Lee, S.A. Pruzinsky, and P.V. Braun, *Adv. Mat.* **14**, 271 (2002).

[87] T.A. Taton and D.J. Norris, *Nature* **416**, 685 (2002).

[88] J.E. Curtis, B.A. Koss, and D.G. Grier, *Opt. Comm.* **207**, 169 (2002).

[89] *http://www.susqu.edu/brakke/*

[90] B. Bayender, N. Marasli, E. Cadirli, H. Sisman and M. Gunduz, *J. Cryst. Growth* **194**, 119 (1998).

[91] V. Seetharaman, L.M. Fabrietti, and R. Trivedi, *Metall. Trans. A* **20A**, 2567 (1989).

[92] K. Lee and W. Losert, *J. Cryst. Growth* **269**, 592 (2004).

[93] J.W. Cahn, *Acta Metall. Mater.* **39**, 2189 (1991).

[94] W.A. Tiller, *J. Appl. Phys.* **34**, 2757 (1963).

[95] H. Nguyen Thi, B. Drevet, J.M. Debierre, D. Camel, Y. Dabo, and B. Billia, *J. Cryst. Growth* **253**, 539 (2003).

[96] T.V. Savina, A.A. Nepomnyashchy, S. Brandon, D.R. Lewin, and A.A. Golovin, *J. Cryst. Growth* **240**, 292 (2002).

[97] M.B. Koss, J.C. LaCombe, M.E. Glicksman, V. Pines, and A. Chait, *Presentation at the 2002 Materials Science Conference* (Huntsville, Alabama, June25-26, 2002).

[98] R.H. Mathiesen, L. Arnberg, F. Mo, T. Weitkamp, and A. Snigirev, *Phys. Rev. Lett.* **83**, 5062 (1999).

[99] J. S. Langer, *Phys. Rev. Lett.* **44**, 1023 (1980).

[100] A. Karma, *Phys. Rev. Lett.* **59**, 71 (1987).

[101] For a review on pattern forming systems, see, e.g., M. C. Cross and P. C. Hohenberg, Rev. Mod. Phys. **65**, 851 (1993). Also see: B. Caroli, C. Caroli and B. Roulet, in *Solids Far from Equilibrium*, C. Godrèche ed., Cambridge University Press (1992).

[102] K. A. Jackson and J. D. Hunt, *Trans. Metall. Soc.* AIME **236**, 1129 (1966).

[103] K. Kassner and C. Misbah, *Phys. Rev. A* **44**, 6513 (1991).

[104] V. Seetharaman and R. Trivedi, *Metall. Trans. A* **19A** 2955 (1988).

[105] G. Faivre and J. Mergy, *Phys. Rev. A* **45** 7320 (1992); **46** 963 (1992).

[106] M. Ginibre, S. Akamatsu, and G. Faivre, *Phys. Rev. E* **56**, 780 (1997).

[107] S. Akamatsu, M. Plapp, G. Faivre and A. Karma, *Phys. Rev. E* **66** 030501(R) (2002).

[108] S. Akamatsu, S. Moulinet and G. Faivre, *Metall. Mater. Trans. A* **32A** 2039 (2001).

[109] A. Karma and A. Sarkissian, *Metall. Trans. A* **27A**, 635 (1996).

[110] M. Zimmermann, A. Karma and M. Carrard, *Phys. Rev. B* **42**, 833 (1990).

[111] S. Akamatsu and G. Faivre, *Phys. Rev. E* **61**, 3757 (2000).